

POLITECNICO DI TORINO

Corso di Laurea Magistrale

in Ingegneria

Aerospaziale

Tesi di Laurea Magistrale

**Supersonic retropropulsion for human Mars
exploration class missions: overview and CFD
code validation**



Relatori:

Prof. Domenic D'AMBROSIO

Prof. Roberto MARSILIO

Candidato :

Adriano Pansini

Anno Accademico 2019/2020

AKNOWELDGEMENTS

I would like to express my gratitude to my supervisors, Prof. D'Ambrosio Domenic and Prof. Marsilio Roberto, for giving me the opportunity to work with them and for the support , encouragements, suggestions, and patience provided throughout these months. Thanks for sharing your experience and knowledge with me.

I would like to thank my family for the love they give me every day, your love and support gave me the strength to overcome every obstacle.

Lastly, but not least, I would also like to thank all my friends for making me feel at home even when I was away.

Thanks to all the people who have been close to me during these university years, without you, all this would not have been possible.

TABLE OF CONTENTS

LIST OF FIGURES.....	5
LIST OF TABLES.....	7
LIST OF SYMBOLS	7
ABSTRACT.....	11
Chapter 1.....	12
1. Overview on Mars EDL technologies and their limits, introduction to Supersonic Retropropulsion	12
1.1 Introduction to EDL.....	12
1.2 Challenges to Mars EDL	14
1.3 Past Landed Mission	15
1.4 Limits of the EDL past technologies	19
1.4.1 Blunt 70° degrees sphere cone aeroshell.....	19
1.4.2 Supersonic 16 m Disk Gap Band parachute	21
1.5 Future robotic Mars mission	24
Chapter 2.....	26
Supersonic retropropulsion for human Mars exploration class missions	26
2.1 Aerocapture	26
2.2 Parametric studies for entry and descent phase for human Mars class exploration missions	29
2.3 EDL SA and human exploration of Mars DRA 5.0: studies and assessments.....	33
Chapter 3.....	45
Supersonic retropropulsion, aerodynamic main features	45
3.1 Blunt body in supersonic flow field.....	45
3.2 Underexpanded and highly underexpanded jet flow.....	51
3.3 Supersonic retropropulsion flowfield	53
Chapter 4.....	58
4.1 Introduction to CFD and test reference case	58
4.2 Introduction to Star CCM+.....	64
4.3 Simulation Setup.....	65
4.3.1. Geometry	65
4.3.2. Regions and boundary condition	68
4.3.3. Physics models:.....	71
4.3.4. Mesh.....	74
4.4. Results- Nozzle case.....	80
4.4.1. Qualitative Comparison.....	80
Pseudo Schlieren image.....	84
4.4.2 Flow main features dimension.....	86

4.4.3. Pressure coefficient comparison	87
4.5.No nozzle case-set up	91
4.5.1. Geometry	91
4.5.2. Difference with the previous simulation	91
4.5.3. Calculation of the nozzle exit condition.....	93
4.6. Results -No nozzle case.....	96
4.6.1. Comparison of the field parameters	96
4.6.2.Mach isocontours -pressure and temperature isocontours – qualitative comparison.....	107
Pseudo- Schlieren scene	110
4.6.3. No nozzle case -flow features dimension	112
4.6.4 Pressure coefficient comparison	113
4.7 Frequency analysis.....	115
4.7.1. Frequency analysis with grid refinement	117
Conclusion	118
Bibliography	121

LIST OF FIGURES

Figure 1 - Earth and Mars atmospheric comparison [3]	14
Figure 2 - Viking configuration [4]	15
Figure 3 - Viking descent profile [4]	16
Figure 4 - Past and current mission descent profile [3]	17
Figure 5-MSL EDL sequence of events [7]za	18
Figure 6 - Blunt body employed for the past missions [3]	19
Figure 7 - Ballistic and lifting L/D Mars EDL nominal trajectory for different β ($\beta = 63\text{kgm}^2$ and $\beta = 153\text{kgm}^2$) [3]	20
Figure 8 - trajectory for an entry vehicle with twice the entry mass and coefficient 1.26 time higher than of MSL, and the same vehicle with twice MSL's lift [8]	21
Figure 9 - Disk gap band parachutes with different canopy dimension [9]	22
Figure 10 – DGB qualification regions [7]	23
Figure 11 - Parachute deployment region, Mach Box [3]	23
Figure 12 - Schematic representation of the Aerocapture maneuver [11]	27
Figure 13 - Aerocapture width corridor for mid L/D=0.3 70° aeroshell [11]	28
Figure 14 - Mach 2 3 4 transition altitude as a function of L/D, entry mass, single or double use heatshield, heatshield diameter [11]	30
Figure 15 - EDL mass versus Total mass at entry with payload mass set to 60 tons, [11].....	31
Figure 16 - Parachute diameter chose to allow a supersonic deceleration from Mach 3 to Mach 0.8, from 2 km of altitude, with mid L/D rigid 70° cone shape aeroshell 15 m [3].	32
Figure 17 - Exploration class architectures [10]	35
Figure 18 - Aeroshell aerodynamic analysis performed with DPLR code [10]	36
Figure 19 - CBAEREO and DPLR solutions for flexible aeroshell.	36
Figure 20 - Comparison between Arch 1 and Arch 2 in terms of time , trajectory and terminal descent initiation altitude [10]	38
Figure 21 - Altitude versus velocity of the reference EDL SA architectures. [10]	39
Figure 22-Mass comparison for the eight architectures	40
Figure 23 - Boundary condition for transition event for both architectures [14]	40
Figure 24 - Event sequence for the rigid mid L/D aeroshell followed by SRP elaborated by Team X [14]	41
Figure 25- Event sequence for the HIAD aeroshell followed by SRP elaborated by Team x [14]	42
Figure 26- Propulsion system design [14]	43
Figure 27 - Figure for an entry vehicle [15]	45
Figure 28 - Representation of a detached bow shock	46
Figure 29 - θ - β -Mach curve	47
Figure 30 - Region of interest for the calculation [16]	49
Figure 31 - Jet underexpanded configuration [18]	51
Figure 32 – Underexpanded jet structure [23]	52
Figure 33 - SRP flowfield [24]	53
Figure 34 - Variation of axial coefficient and drag coefficient related to thrust coefficient with a central nozzle [25]	55
Figure 35 - Transition between long and blunt penetration mode [25]	56
Figure 36-Navier Stokes equations	57
Figure 37-Relevant flow dimension computed for run 165 ref. [30]	61
Figure 38-Schlieren, pseudo Schlieren and Mach isocontours scenes, from reference [29]	61
Figure 39-Forebody and Aftbody averaged surface pressure coefficient distribution [29]	62
Figure 40-Forebody and aftbody averaged surface pressure coefficient distribution from reference [31]	62
Figure 41-Section view of the model baseline	65
Figure 42-Nozzle section , derived from the sketch of the geometry adopted in the simulation	66

Figure 43-Centerline nozzle section adopted from appendix A	66
Figure 44-Aftbody and forebody sketch, with the blue line highlighting the contours of the bodies	67
Figure 45-global sketch	67
Figure 46-global view of the extruded model	68
Figure 47- aftbody and forebody boundaries	70
Figure 48-nozzle and reservoir boundaries	70
Figure 49- lateral boundaries of the region	71
Figure 50-outer unperturbed region mesh vs mesh elaborated inside the volumetric control	77
Figure 51-cone shape adopted for the volumetric control	78
Figure 52-Nozzle and reservoir grid	78
Figure 53- aftbody, forebody and rounded junction grid	79
Figure 54-zoom on the prism layers structure	79
Figure 55-residuals plot for the las 50000 iterations up to the current solution time	80
Figure 56-Mach isocontours	82
Figure 57-temperature isocontours	83
Figure 58-Pressure isocontours	83
Figure 59-streamlines visualization on Mach isocontours scene	84
Figure 60-Pseudo Schlieren image	85
Figure 61--Aftbody averaged surface pressure coefficient distribution	88
Figure 62-Forebody averaged surface pressure coefficient distribution	89
Figure 63-Nozzle exit instead of the convergent-divergent nozzle	91
Figure 64-point 2, nozzle case simulation	92
Figure 65-point 3 on the bottom left and point 4 upon the body corner, no nozzle case	93
Figure 66-Mach function and graphical representation of the solution of the nonlinear equation	95
Figure 67-MATLAB computation of the Newton Bisection Method	95
Figure 68-No nozzle simulation, point 2 Mach number over 20000 iterations	97
Figure 69-Nozzle simulation, point 2 Mach number over 20000 iterations	97
Figure 70-No nozzle simulation, point 2 pressure over 20000 iterations	98
Figure 71-Nozzle simulation, point 2 pressure over 20000 iterations	98
Figure 72-No nozzle case, point 2 temperature over 20000 iterations	99
Figure 73-Nozzle case, point 2 temperature over 20000 iterations	99
Figure 74-No nozzle case, point 4 Mach number over 40000 iterations	100
Figure 75-Nozzle case, point 4 Mach number over 40000 iterations	100
Figure 76-No nozzle simulation, point 4 pressure over 40000 iterations	101
Figure 77-Nozzle simulation, point 4 pressure over 40000 iterations	101
Figure 78-No Nozzle case, point 4 temperature over 40000 iterations	102
Figure 79-Nozzle case, point 4 temperature over 40000 iterations	102
Figure 80-No nozzle case, point 3 Mach number over 40000 iterations	103
Figure 81-Nozzle case, point 3 Mach number over 40000 iterations	104
Figure 82-No nozzle case , point 3 pressure over 40000 iterations	104
Figure 83-Nozzle case, point 3 pressure over 40000 iterations	105
Figure 84-No nozzle case, point 3 temperature over 40000 iterations	105
Figure 85-Nozzle case, point 3 temperature over 40000 iterations	106
Figure 86-Mach isocontours scene with SRP flowfield main features, no-nozzle case	107
Figure 87-Mach isocontours scene for the no-nozzle simulation	108
Figure 88-temperature isocontours scene for the no-nozzle simulation	109
Figure 89-Pressure isocontours scene for the no nozzle simulation	110
Figure 90-Pseudo Schlieren image, no-nozzle case	111

Figure 91-Aftbody averaged surface pressure coefficient distribution _____	113
Figure 92-Forebody averaged surface pressure coefficient distribution _____	114
Figure 93-point 4 dynamic frequency analysis, nozzle simulation _____	116
Figure 94-point 4 dynamic frequency analysis-no nozzle simulation _____	116
Figure 95-point 4 dynamic frequency analysis-no nozzle simulation, grid refinement _____	117

LIST OF TABLES

Table 1- Mars EDL technologies summary for past missions [3] _____	16
Table 2 - DGB and ringsail parachute comparison _____	24
Table 3 - Mass sizing for EDL , elaborated by the DRA 5.0 team [12] _____	34
Table 4-Freestream conditions run 165 _____	60
Table 5-Exhausting Jet conditions _____	60
Table 6- nozzle main features dimension _____	66
Table 7-aftbody and forebody main features dimension _____	67
Table 8-boundary types _____	69
Table 9-freestream conditions _____	70
Table 10-Default mesh condition, unperturbed outer region< _____	75
Table 11-Default mesh conditions, nozzle parts _____	75
Table 12-Default mesh conditions, aftbody, forebody and rounded junction_	76
Table 13-Default mesh condition, inferior boundary of the reservoir _____	76
Table 14- Default mesh condition, volumetric control _____	76
Table 15-total number of cells, interior faces and vertices for the adopted mesh	76
Table 16.-comparison between the two adopted mesh _____	77
Table 17-dimensions comparison _____	86
Table 18-Number of cells, vertices, and faces _____	91
Table 19-Point 2 Mach number averages for both iterations _____	97
Table 20-Point 2 pressure averages for both simulations _____	98
Table 21-point 2 temperature averages for both simulations _____	99
Table 22-Point 4 Mach number averages for both iterations _____	101
Table 23-Point 4 pressure averages for both simulations _____	102
Table 24-point 4 temperature averages for both simulations _____	102
Table 25-Point 3 Mach number averages for both iterations _____	104
Table 26-point 3 pressure averages for both simulations _____	105
Table 27- point 3 temperature averages for both simulations _____	106
Table 28- comparison of flow features dimension _____	112

LIST OF SYMBOLS

Acronyms

AoA	Angle of attack
AOCS	Attitude orbit and control system
ARC	Ames Research Center
AUSM	Advection Upstream Splitting Method
BPM	Blunt Penetration Mode
BUD	Bridle Umbilical Device
DGB	Disk Gap Band

EDL	Entry Descent and Landing
EDL SA	Entry Descent and Landing System Analysis
EDTP	Exploration Technology Development Program
FEM	Finite Element Method
GNC	Guidance Navigation control
HAT	Human Spaceflight Architecture Team
HIAD	Hypersonic Inflatable Aerodynamic Decelerator
IAD	Inflatable Aerodynamic Decelerator
ISS	International Space Station
LARC	Langley Research Center
LHIAD	Large Hypersonic Inflatable Aerodynamic Decelerator
LOX/LH2	Liquid Oxygen-Liquid Hydrogen
LOX/LCH4	Liquid Oxygen-Liquid Methane
LPM	Long Penetration Mode
LSQ	Least Squares
MAWG	Mars Architecture Working Group
MDRA 5.0	Mars Design Reference Architecture 5.0
MOLA	Mars Orbiter Laser Altimeter
MER	Mars Exploration Rover
MSL	Mars Science Laboratory
MPF	Mars Pathfinder
MR	Mixture Ratio
NS	Navier Stokes
PICA	Phenolic Impregnated Carbon Ablator
PDV	Power Descent Vehicle
POST2	Program to Simulate Optimized Trajectories
RCS	Reaction control System
RL10	Liquid Fuel Cryogenic rocket engine
SIAD	Supersonic Inflatable Aerodynamic Decelerator
SLA 561	Silica Lightweight Ablator
SOA	State of Art
SRP	Supersonic Retropropulsion

STAR CCM+	Simulation of Turbulent Flow in Arbitrary Regions	regions-computational continuum
TRL	Technology Readiness Level	
UPWT	Unitary Plan Wind Tunnel	

Latin and Greek Symbols

A	m^2	Area
Ca	/	Axial coefficient
Cd	/	Drag coefficient
Cp	/	Pressure coefficient
Cv	J/K	Specific heat at constant volume
d	m	Diameter
e	J/kg	Total energy per unit mass
E	J	Total energy
g_∞	depends	Generic value referred to the freestream unperturbed condition
g_e	depends	Generic value at the nozzle exit section
g_{ref}	depends	Generic value used as reference value
g_{throat}	depends	Generic value at the nozzle throat section
g_{total}	depends	Generic total value of the quantity
h	J/kg	Enthalpy per unit mass
Isp	s	Specific impulse
kHz	Hertz	Frequency
Kn	/	Knudsen number
L/D	/	Lift to drag ratio
m	kg	Mass
M	/	Mach number
\vec{n}	/	Normal direction
p	Pa/bars/psi/ $\frac{N}{m^2}$	Pressure
q	Pa	Dynamic pressure
Q	W/m ²	Heat flux
R	m	Radius
Re	/	Reynolds number
s	seconds	Time

t	tons	Mass
t	K	Temperature
T	kN	Thrust
T/W	/	Thrust to weight ratio
v, u, w	m/s	Velocities along x, y, z
x, y, z	m	Coordinates
X,Y,Z	m	Reference axes
β	$\frac{\text{kg}}{\text{m}^2}$	Ballistic coefficient
β	°	Shock inclination
γ	/	Gas constant
Δ	m	Standoff distance
Δ	/	Variation
ε	/	Ratio among nozzle exit are and nozzle throat area
θ	°	Corner inclination
μ	$\frac{\text{kg}}{\text{ms}}$	Kinematic viscosity
ν	$\frac{\text{m}^2}{\text{s}}$	Dynamic viscosity
ρ	$\frac{\text{kg}}{\text{m}^3}$	Density

ABSTRACT

The supersonic retropropulsion (SRP) represents the most likely mean to slow down the spacecraft during the descent phase of the next era of Martian missions, i.e. human Mars exploration class missions. A general overview of the Entry-Descent-Landing phase (EDL) is provided, referring to the past missions to derive their limits and understand the importance of SRP for overcoming them. The preliminary results of the NASA studies for the parametrization and conceptual design of a propulsion system implementing SRP during a descent Mars phase are also presented.

Among all the fields of interest concerning the application of SRP, the aerodynamic one has been studied since the 60s, representing an important topic of research and development. In order to better understand the complexity of the flowfield, due to the interaction of a bow shock and exhausting highly underexpanded jet, all the factors that contribute to the definition of this flowfield have been briefly described in their salient points. Afterward, it was demonstrated the ability through the use of a computational fluid dynamic (CFD) commercial software, STAR CCM+, to reproduce the flowfield and SRP main features through a CFD simulation, and thus validate this simulation through the comparisons with reference data. Once the CFD simulation has been validated, it has been possible to make further analysis in the computational field, indeed realizing a simplified situation where the jet expansion conditions have been replicated directly to the nozzle exit section, thus removing the jet expansion inside the convergent-divergent nozzle. The use of such simplification allows a remarkable saving in the number of computational domain points, reducing the computational cost; moreover the verification of such simulation with code-to-code comparison, paves the roads for the applications of this principle in more complex simulations. Finally, an analysis of the fundamental frequencies has been carried out to study the unsteadiness of the flowfield and how the grid resolution affects the capture of unsteady phenomena.

Chapter 1

1. Overview on Mars EDL technologies and their limits, introduction to Supersonic Retropropulsion

1.1 Introduction to EDL

EDL is the acronym standing for Entry, Descent and Landing defined as “the set of operations needed to safely achieve a landing on a body with atmosphere”. [1] In the mission framework of a Mars mission, this phase occurs immediately after an interplanetary transfer orbit and consequential to an Aerobraking maneuver, or, for future mission, to an optimized maneuver called Aerocapture. Either the Aerobraking and the Aerocapture enable the initial condition for the insertion of the spacecraft into an entry trajectory.

As the word EDL says, is possible to split this mission phase into several process:

- The entry phase consists of the bridge between the exo-atmospheric operations and the atmospheric flight. Indeed, is possible to shift the entry phase in different steps. Initially, through a ΔV variation, the spacecraft variates its orbital parameters, reaching the speed and attitude condition ideal to achieve an entry trajectory. Subsequently, the properly entry phase starts, with a variation of speed and a deorbit manoeuvre which enable the transition from the elliptic orbit to an entry trajectory. The atmospheric flight begins after the entry phase; in the atmospheric flight the vehicle is embedded into a hypersonic flowfield with consequent hypersonic aerothermal and aerodynamic conditions. During the hypersonic flight, the vehicle should be capable to realize the “pull-out” manoeuvre, to enable the spacecraft to recover an acceptable flight level, overcome the diving condition, and minimize the altitude loss, and the heading alignment maneuver, to minimize the azimuth error, and thus the error with respect to the targeted landing site. In brief, the entry phase aims to create the condition for the deceleration of the vehicle throughout the hypersonic flowfield and create the initial conditions for the following deceleration phase, with respect to the altitude and attitude constraints imposed by flight dynamics and controlled through the GNC and AOCS systems. Indeed, is also important to emphasize that the bulk of the residual energy from hyperbolic or orbital entry is dissipated in the hypersonic domain. In conclusion, different technologies are involved to accomplish the entry phase, and related improvements and further works will be implemented, in order to achieve compelling tasks as increasing the entry speed and the entry payload.
- The second phase is called the descent phase and is the link between the hypersonic portion of the entry sequence and the last phase of landing. Within this phase the vehicle is subjected to an important variation of the flow-fields condition, passing from a supersonic flight to a high subsonic flow field. Descent initiation may occur on a staging event, generally represented as the separation from the drag device used in hypersonic flight, and starting the operation with the supersonic decelerator means. In the majority of the past Mars mission, the descent phase was initiated with the deployment of the supersonic parachute. The purpose of this stage is to heavily decelerate the vehicle within a short temporal framework, handle the fast operations and interactions of the different technologies involved for this purpose, and providing the correct condition in terms of available propellant, correct altitude, and attitude for the terminal phase of landing. The purpose of the dissertation is to understand how the supersonic retropropulsion could represent a solution to overcome the physic limitations related to the large size and mass of the

vehicle , that occur during the descent and prevent use of past technologies for future missions. Hence in the next section, the descent phase will be deeply treated.

-The last phase is called the landing phase and purely consists of the touchdown phase. The initiation is coupled with the activation of the sensing ground system, while the previous phase is being completed. During the landing terminal phase the total deceleration of the vehicle is achieved through a descent subsonic propulsion system; the termination of the landing is completed when the vehicle hits the ground and the kinetic energy of the impact is dissipated avoiding damage to the payload. In the straight definition of the landing phase, the operation bringing the satellite in an operative state, as a deployment or egress, could be involved.

Despite its simple conceptual description, several systems are required in this phase, and either the ground condition and the vehicle conditions, after two harsh aero-thermodynamic phases, could generate tough constraints for the landing phase. However, for past and future missions, the technologies employed in Viking, represent a viable means for this phase.

In conclusion, two main mission constraints could briefly summarize this critical phase:

Remove the initial energy of the vehicle to allow a safe landing, avoiding crush, and place the final landing point within a 10 km or less elliptic area, to satisfy the targeted mission objectives.

1.2 Challenges to Mars EDL

Nowadays, several aspects still constitute a technologic and scientific challenge to implement a Mars EDL, and those challenges are related to the Mars environment.

- The atmosphere thickness is about $1/100^{\text{th}}$ of Earth's atmosphere. Despite its low aerodynamic drag, the Mars atmosphere could create really high heating transfer condition and thus problem during the descent, linked to the hypersonic deceleration. [2] The deceleration occurs at much lower altitudes, reducing time for the remaining phase of EDL: by the time the velocity is low enough to deploy supersonic or subsonic decelerators the vehicle may be near the ground, with insufficient time to land. The atmospheric dust content and the variability of its conditions, as the presence of storms, adds complexity to the problem.

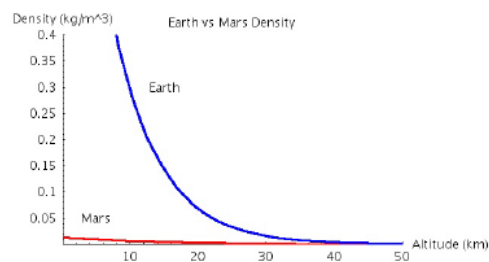


Figure 1 - Earth and Mars atmospheric comparison [3]

- To date, the instabilities, harshness, and sourness of the Mars surface represent a huge concern for the terminal phase of EDL. Whether the distribution of large sized rocks, craters terrains, and drop into the sole altitude drives the limitation and constraints for landing technologies, the bi-model surface elevation strongly imposed aerodynamic limits to the achievement of a target zone in the half of the Mars territory.
- Lastly, the short time span of Mars EDL (5-8 minutes) and the complexity of switching between units in flight causes a non-redundancy of the EDL systems. Therefore, these system should be highly reliable; on the contrary, the huge cost of replicating Mars relevant condition with test and qualification should be took into account. [3]

The heritage acquired from past flight projects mixed with reliable numerical simulation provides a viable base for developing new technologies matching the previous constraints. Hence, the majority of the new architectures considered for future Mars mission, both manned and unmanned, will be based on improvement and refinement of already existing technologies.

1.3 Past Landed Mission

From Mars Pathfinder, to MER and MSL, the capability to land payloads on the Mars surface is based on the adoption and improvement of the EDL architecture developed for the Mars Viking Program.

Viking used different means for the entry phase, the descent, and the terminal landing. The whole EDL architecture was composed by a blunt 70° degrees sphere-cone heatshield , Silica Lightweight Ablator (SLA 561) thermal protection subsystem material, a 50 foot (16m) Disk- Gap Band parachutes, monopropellant liquid engine, doppler and radar altimeter, and the landing gears.

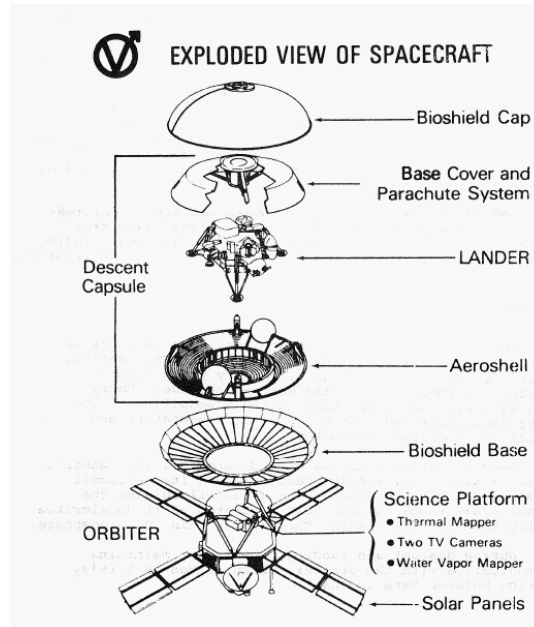


Figure 2 - Viking configuration [4]

The EDL phase followed an in-orbit time, to recognize the optimum landing site. Afterward, the initial conditions for Mars entry are established at an altitude of 125 km, above the surface, with a mean radius of 3522.2 km from the planet core. The entry relative speed for the Viking mission was calculated around 4.7 km/s. The operation started with the separation of the lander and its aeroshell from the orbiter. Within the hypersonic flow field regime, the aeroshell shielded the lander against the intense heat generated through the deceleration in the CO₂ thin atmosphere, providing the optimal state for the descent supersonic phase. Indeed, the disk gap band parachute was deployed to further decelerate the lander at 6000 m above the surface, counteracting a supersonic flow characterized by a Mach number of 2. Immediately after the deployment, the aeroshell was jettisoned, avoiding collision with the parachute. Lastly , the parachute was jettisoned at 1.6 km above the surface, enabling the starting of the terminal propulsive descent, that fired its three monopropellant engines bringing the lander to a 2.4 m/s +- 1m/s horizontally and a < 1m/s vertical speed. Radar altimetry and doppler radar were used to detect horizontal velocity, and landing legs with small clearances for rock were adopted for the touch-down phase . [5] [6] The EDL sequences is shown in figure 3.

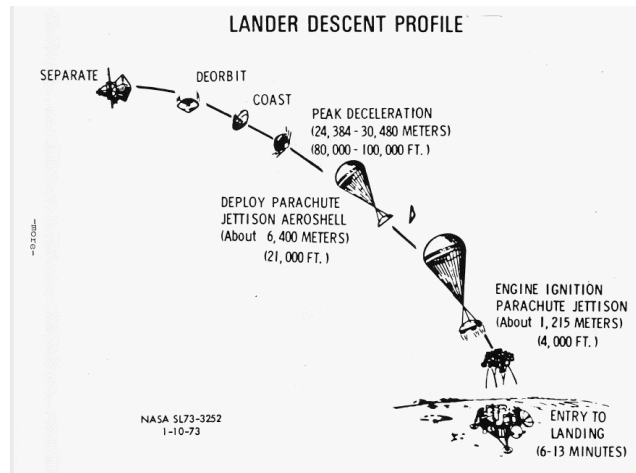


Figure 3 - Viking descent profile [4]

The whole mission was not constrained by low budgets: the availability of testing and qualification for the EDL subsystems facilitated their reliable functioning in the operative conditions, bringing their TRL level to such high value to allow the use of the Viking derived EDL technologies as a back-bone for all the Mars EDL system in the following 40 years.

Mars Pathfinder and Mars Exploration Rover were defined by other constraints and mission goals, but their EDL systems represented an upgrade and a modification of the Viking technologies.

The following table summarizes EDL features of the mentioned mission, and it's easy to notice the common guidelines in terms of aerodynamic values (i.e. Parachute dynamic pressure, Parachute deploy Mach number, Drag coefficient, Ballistic coefficient, entry velocity,), technologies (TPS , Heatshield, entry attitude control, Terminal descent decelerator, Speed sensing, touchdown system) ,and performance (useful landed masses, touchdown mass) .

Table 1- Mars EDL technologies summary for past missions [3]

Landing Year:	1976	1976	1997	2004	2004
Mission:	Viking 1	Viking 2	MPF	MER-A (Spirit)	MER-B (Opportunity)
Entry From	Orbit	Orbit	Direct	Direct	Direct
Entry Velocity (km/s)	4.7	4.7	7.26	5.4	5.5
Orbital Direction	Posigrade	Posigrade	Retrograde	Posigrade	Posigrade
Entry Flight Path Angle (deg)	-17	-17	-14.06	-11.49	-11.47
Ballistic Coefficient (kg/m ²)	64	64	63	94	94
Entry Mass (kg)	992	992	584	827	832
Entry Attitude Control	3-axis RCS	3-axis RCS	2 RPM passive	2 RPM passive	2 RPM passive
Trim Angle of Attack at entry	-11 deg	-11 deg	0 deg	0 deg	0 deg
Entry Lift Control	C.M. offset	C.M. offset	no offset	no offset	no offset
Entry Guidance	Unguided	Unguided	Unguided	Unguided	Unguided
Lift to Drag Ratio	0.18	0.18	0	0	0
Aeroshell (Heatshield) Diameter (m)	3.5	3.5	2.65	2.65	2.65
Heat Shield Geometry	70 deg cone	70 deg cone	70 deg cone	70 deg cone	70 deg cone
Heat Shield TPS	SLA-561	SLA-561	SLA-561	SLA-561	SLA-561
Heat Shield TPS Thickness (in)	0.54	0.54	0.75	0.62	0.62
Total integrated heating (J/m ²)	1100	1100	3805	3687	3687
Peak Heating Rate (W/cm ²)	26	26	100	44	44
DGB Parachute Diameter (m)	16	16	12.5	14	14
Drag Coefficient (approx.)	0.67	0.67	0.4	0.4	0.48
Parachute Deploy Mach No.	1.1	1.1	1.57	1.77	1.77
Chute Deploy Dyn.Pressure (Pa)	350	350	585	725	750
Parachute Deploy Altitude (km)	5.79	5.79	9.4	7.4	7.4
Descent Attitude Control	RCS Roll Rate	RCS Rate	none	none	none
Altitude Sensing	RADAR	RADAR	RADAR	RADAR	RADAR
Altitude Sensing Range (km)	137	137	1.6	2.4	2.4
Horizontal Velocity Sensing	Doppler RADAR	Doppler RADAR	none	Imaging/IMU	Imaging/IMU
Terminal Descent Decelerator	Mono-prop N2H4	Mono-prop N2H4	Solid Rockets	Solid Rockets	Solid Rockets
Terminal Descent Velocity Control	Throttled	Throttled	Sep. Cutoff	Sep. Cutoff	Sep. Cutoff
Horizontal Velocity Control	Throttled pitch	Throttled pitch	Passive	Lateral SRMs	Lateral SRMs
Touchdown Vertical Velocity (m/s)	2.4	2.4	12.5	8	5.5
Touchdown Horizontal Velocity (m/s)	< 1	< 1	< 20 (design)	11.5	9
Touchdown Attenuator	3 crushable legs	3 crushable legs	4-pi Airbag	4-pi Airbag	4-pi Airbag
Touchdown Rock Height Capab. (cm)	20	20	50	50	50
Touchdown Slope Capab. (deg)	15	15	>30	>30	>30
Touchdown Sense	Leg crush motion	Leg crush motion	Rollstop	Time out	Time out
Touchdown Sensor			Accelerometer	clock	clock
Touchdown Mass (kg)	590	590	360	539	539
Useful Landed Mass (kg)	244	244	92	173	173
3-sig. Landed Ellipse Major axis (km)	280	280	200	80	80
3-sig. Landed Ellipse Minor axis (km)	100	100	100	12	12
Landing Site Elevation (km MOLA)	-3.5	-3.5	-2.5	-1.9	-1.4

A remarkable consequence inferred from the above considerations is that also the entry aerodynamic profile, in terms of Mach number, entry velocity, and relative altitude, is similar between these missions, as shown by the next figure.

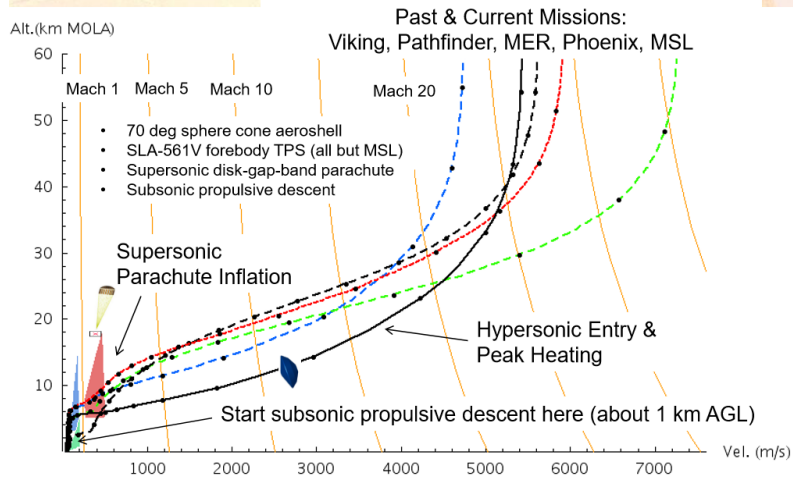


Figure 4 - Past and current mission descent profile [3]

According to Viking, MER, and MPF mission the inflection point in the trajectories, placed in the lower left corner of the figure, indicates the deployment of the parachute. For all those missions the point of deployment converges to a similar value in terms of Mach and altitude, underlining the similarities and contact point related to the adoption of the same base EDL technologies. Moreover, the trajectory path in the atmospheric is almost the same, slightly varying in altitude and speed due to the different payloads of each mission.

The black solid curve represents the Mars Science Laboratory trajectory path; launched in 2011, the Mars Science Laboratory defines the state of art for Mars EDL system, becoming the milestone for the next generation of robotic EDL systems, capable to land a 900 kg rover in a landing ellipse much smaller than any previous Mars lander and thus overcoming some limits of the technologies qualified for past missions.

The main features of the MSL EDL systems will be briefly reported, underlying the difference with the previous technologies, especially those regarding the descent, and terminal descent phase and the evolution of the landing system which enable the accomplishment of tons of landing. The spacecraft was composed of a cruise stage, an entry aeroshell, formed by the heatshell and the backshell, and a descent stage and a rover nested into the aeroshell.

In the entry and descent phase, the MSL resumed the configuration with a 70° degrees blunt sphere cone aeroshell and supersonic parachute. The aeroshell underwent a higher peaky heat rate, suffering a smooth body transition to turbulence regime, due to the higher ballistic coefficient, larger diameter, and higher atmosphere relative entry speed. As long as the shear stress overcame the classic values for the previous missions, the use of Phenolic Impregnated Carbon Ablator (PICA) as the forebody TPS replaced the SLA 561 V, only used on the backshell, subjected to lessen heat rates, thus varying for the first time the TPS legacy tied to the forebody features. The bulk of the kinetic energy was dissipated through the deceleration from the hypersonic regime to the supersonic flowfield. Hence, this flowfield made possible the use of a supersonic disk band gap parachute. The heavier payload and high landed altitude required a more performant parachute than those employed in the past missions. Indeed, it was used a single 21.5m diameter supersonic parachute, scaled from the 16m Viking DGB, the widest that has ever flown on Mars.

During the descent phase, the vehicle slowed down from 450 m/s to 100 m/s, within 50-90 s and burnt over 95 % of the kinetic energy remained. After the action of the supersonic decelerators , the spacecraft was subjected to subsonic conditions, and several critical reconfigurations events: the jettisoned of the heatshield, acquisition of Martian surface data, the discard of the backshell, and the preparation for the powered descent. Indeed the powered descent was implemented with a similar scheme with respect to the past mission, and the set of tools and equipment employed in this phase was named the power descent vehicle PDV. Following the powered descent , the touchdown phase took place. The touchdown employed by MSL, called the “Skycrane” manoeuvre, was the most innovative portion of the EDL architecture.

When the PDV reached a rate of 0.75 m/s, at an altitude around 20 m, the separation pyros were fired to release the rover. Since then , the PDV was separated in two vehicles, the Descent Stage and the Rover. While the DS is maintained at 0.75 m/s vertical descent speed, the lander was lowered through the Bridle and Umbilical device system , exploiting an electromagnetic brake implemented with three bridles placed into a spool, that gradually deployed until achieving their full extension of 7.5m. The rover touchdown was detected via persistence of bridle offloading as inferred from DS throttled command .The last part of the sequence was the “ snatch “ maneuver, which prepared the rover for touchdown using the development of the rover mobility system. Once the rover touched down the ground, the descent stage cut the umbilical and severed the bridle system, and used the engines to convert the descent into an ascent movement, in order to fall at the distance of 150 m away to the rover. [7]

The whole sequence is summarized in the next figure.



Figure 5-MSL EDL sequence of events [7]

1.4 Limits of the EDL past technologies

“Mars Science Laboratory defines the SOA for Mars EDL systems. Current estimates on the extensibility of the MSL architecture indicate that it is limited to roughly 1.5 t delivered mass. In contrast, estimates for human scale Mars missions, will require 20-60 tons of landed payload mass. Thus, NASA cannot continue to rely on the EDL technology investments of the ‘60’s and ‘70’s as a baseline to enable future missions”. [1]

The dissertation will be focused on supersonic retropropulsion as a viable means for achieving the descent phase of EDL operations and for enhancing the terminal landing phase condition. Therefore, the major concerns are related to the thickness of the atmosphere and the consequent time for hypersonic and supersonic deceleration. The sourness and hazardous characterizing the surface’s environment won’t be consider, as the problematics related to the touchdown phase and technologies.

This section is focused on the analysis of technical limits related to Viking-derived technologies employed in the entry and descent phase, introducing the need for other solutions and technological advancements to accomplish the future Mars mission class requisites.

As previously depicted, the goal of landing on the Martian surface has been achieved thanks to the development of the heritage acquired with the Viking program :the blunt 70 ° sphere cone aeroshell, equipped with SLA 561 V thermal body protection, and supersonic disk- gap band parachutes were the milestones granting the correct landing of several payloads. The deceleration from hypersonic to supersonic, using the aerodynamic features of the aeroshell, and subsequent deceleration from supersonic to subsonic, through the parachute, has been adopted and followed for all the past missions. Although the knowledge, cost effectiveness and reliability acquired throughout the past mission, these technologies set important limitations preventing their application for mission heavier than 1-2 tons.

1.4.1 Blunt 70° degrees sphere cone aeroshell.

From the Viking mission, different variants of the cone aeroshell have been employed in all the landed Mars mission.

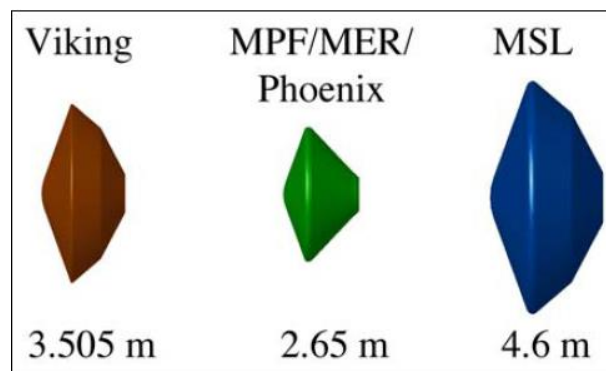


Figure 6 - Blunt body employed for the past missions [3]

The 70 degrees stands for the angle among the blunt body and aeroshell. The large usage of this technology is explained through its aerodynamic performance. This shape is characterized by a hypersonic C_d of 1.68, allowing an enormous loss of kinetic energy in the hypersonic flight. This shape is dynamically stable even if an angle of attack is induced and could lead to a lift to drag ratio up to 0.24. Hence , the three above configurations have successfully flown in the Mars atmosphere, creating a broad and reliable set of performance data , and raising confidence in this shape body.

The ballistic coefficient drives the behavior of an entry body in hypersonic and supersonic flow-field.

The ballistic coefficient is defined as:

$$\beta = \frac{m}{A C_D} \left(\frac{\text{kg}}{\text{m}^2} \right)$$

Where m stands for the entry mass, A is the cross-section area of the body, and C_d represents the drag coefficient.

A low ballistic coefficient has two main effects on the entry and descent phases: increasing the altitude where deceleration occurs, and decreasing the thermal peak. The crucial increase in the altitude is essential for the further deceleration phase: gaining time in a framework where all the events succeed each other rapidly is a key-point. The reduction of β above certain value could allow a deceleration without any parachutes. On the contrary, increasing β , decrease the chance of matching the Mach and dynamic pressure conditions for the parachutes opening.

For future Mars missions, where the tons limit will be overcome, the coefficient should of course grow due to its linear relationship with the entry mass. The rise of β could be counteracted by increasing the cross-section area, but the practical limits of this area should be taken into account. However, the ballistic coefficient, for the Viking heritage shapes, would go up as the diameter of the aeroshell: beyond the increase of the cross section area A , since the density of the entry vehicle's internal payload is considered constant, and the mass is approximately proportional to the vehicle's diameter cubed, β will to first order grow in proportion to the diameter. To date the maximum value of β is set to $115 \left(\frac{\text{kg}}{\text{m}^2} \right)$ with an aeroshell diameter of 4.6 m, derived from the MSL architecture. Larger aeroshell will require larger launchers, as the new Falcon Heavy, since the actual fairing launcher couldn't fit this geometric requirement. In addition considering the MSL density as an upper limit, and considering an aeroshell maximum diameter of 5 m, the maximum available β for robotic Mars mission class is around $153 \left(\frac{\text{kg}}{\text{m}^2} \right)$. [3]

This value is employed to highlight the behavior of the vehicle trajectory as a function of β .

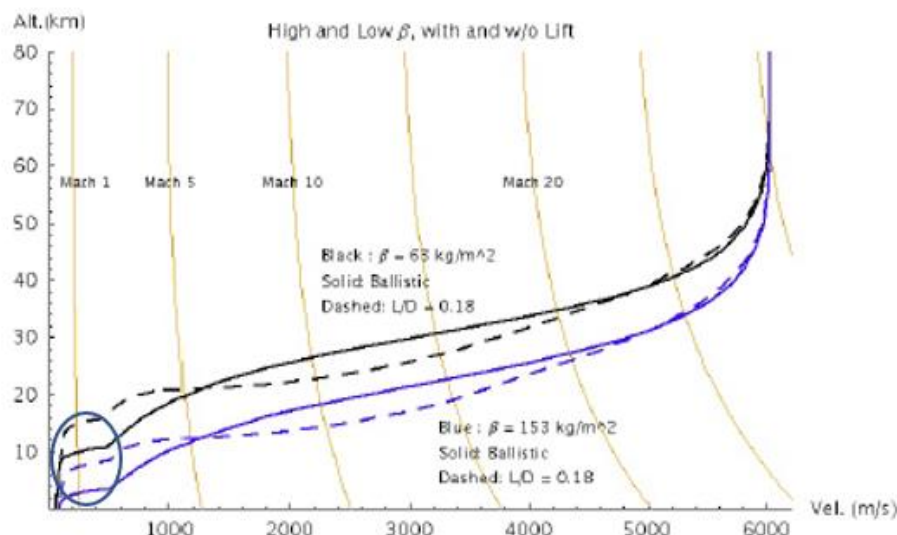


Figure 7 - Ballistic and lifting L/D Mars EDL nominal trajectory for different β ($\beta = 63 \frac{\text{kg}}{\text{m}^2}$ and $\beta = 153 \frac{\text{kg}}{\text{m}^2}$) [3]

Assuming the same entry velocity of 6 km/s, same L/D, same supersonic decelerators means (parachute deployment at Mach 2.1, and aeroshell with a diameter of 19.7 m, and a C_d of 0.65), and same flight path

angles, the inflation point of the curves, circled on the chart, suggests an important decrease in the height at which parachute opens, for the same opening Mach number, of about 7 km . The reduction causes a decrease in the available time for supersonic deceleration, and consequently prevents the landing at certain altitudes, highlighting the inability of landing for certain β values at certain MOLA altitudes. Last but not least, the trajectory obtained for the augmented β represents an important limitation and constraint for the vehicle in order to fall within the range of the so-called “ Mach Box” , which is related to the operations of the supersonic parachutes, and will be explained in the next section.

On the other hand, augmenting the lift , and hence the lift to drag ratio, could increase the parachute deployment altitude at the same Mach number, gaining time for further deceleration. This consequence could be better understood zooming on the left lower part of the chart, represented in a similar graph in figure 10.

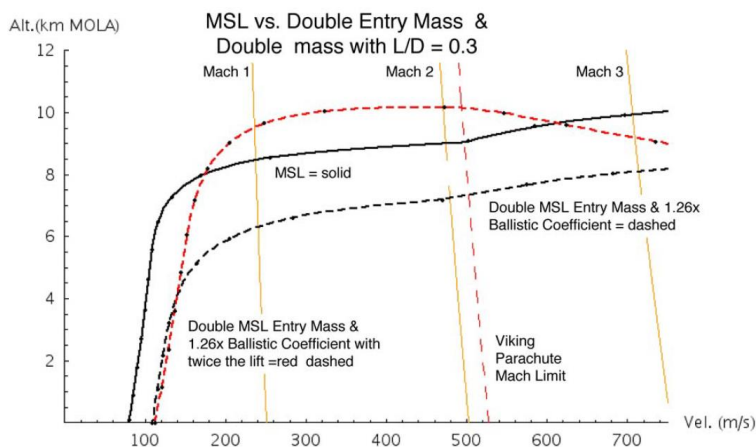


Figure 8 - trajectory for an entry vehicle with twice the entry mass and a ballistic coefficient 1.26 time higher than of MSL, and the same vehicle with twice MSL's lift [8]

The adverse impact of increasing beta, induced by the mass augmentation (black vs dashed black lines) could be counteracted by expanding the L/D ratio from 0.18 to 0.30 , acting on the capability to increase the lift. Despite this theoretical solution , several assessments indicate the unfeasibility of modifying the L/D ratio with the Viking's blunt body aeroshell shape. Hence, the addition of lift remains a possible solution to improve the performance of this type of aeroshell, but the design of additional lift should be well balanced with the increase of the cross-section area, and then of the diameter, which would cause the augmentation of β ,thus counterbalancing the positive effect related to the lift. Moreover , to optimize the lift for reducing kinetic energy, the lift is applied in the downward direction while the vehicle's speed is above 3.4 km/s, orbital Mars speed, and upward direction for lower speed . [8]

In conclusion , despite the heritage gained throughout the past landed Mars mission, the increase of the ballistic coefficient related to the mass of the future Mars exploration mission, will undermine the use of this entry-body coupled with supersonic parachute deceleration.

1.4.2 Supersonic 16 m Disk Gap Band parachute

Following the hypersonic deceleration, all Mars landing systems, used a supersonic parachute for slowing down to subsonic conditions. The parachutes served for several purpose as :

- Decreasing the ballistic coefficient and increase the drag area;
- Slow down the system within critical altitude;
- Provide vehicle stability through the transonic regime;
- Facilitate the downward separation of the heatshield.

The parachute allows the accomplishment of these critical steps to handle the reconfiguration of the system for the last terminal descent phase. As for the aeroshell, all the past landed missions rely on the heritage of the Viking program, using the DGB Viking parachute as a baseline for the development of their supersonic chute.

The “Disk Gap Band” directly refers to the parachute’s structure: designed for well balance drag and stability is based on a disk that forms the canopy, a small gap and a cylindrical band. Disk gap band chutes are a variant of circular canopies that have better stability characteristics: the gap allows a through-flow which stays better attached to the canopy avoiding asymmetric flow separation which can cause oscillations. Each gore is approximately triangular with a rectangular segment to form the band. [9]

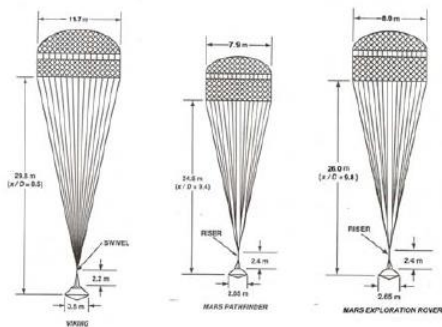


Figure 9 - Disk gap band parachutes with different canopy dimension [9]

The use of the supersonic parachute as a viable means for the deceleration through the supersonic regime, was possible via the qualification tests established in 1972, during the maturing of Viking. By means of these expensive tests the performances of DGB were evaluated and demonstrated compliance with the mission requirements. Indeed, these tests were conducted in Earth’s atmosphere recreating Mars relevant condition, under high speed coupled with high altitude environment. The results demonstrated the capability to robustly deploy, inflate and decelerate the payload in the expected flight conditions. Therefore, those capabilities are currently constrained to the Viking tested flight regions, described in terms of Mach number and dynamic pressure, as far as similar qualification tests have never been repeated.

The subsequent parachutes rely on the qualification by similarity of Viking design, coupled with subsonic and static tests to prove deployment and strength characteristics. The different delivered payload caused the variation of the parachute’s size, that should increase if the descent mass increase and should also maintain scaling to the aeroshell diameter. However, while MER and Pathfinder reduced the delivered mass, the MSL system was in charge to slow down a heavier entry payload, and resulted in increased the parachute dimension but still within the limitation imposed by the Viking test qualification.

The DGB parachute ,with diameter tested from 16 to 22 m , was qualified to deploy and inflate between Mach 1.4 and 2.1 , within a dynamic pressure of 250-700 Pa, a considerable margin relative to the Viking flight values of M 1.1 and dynamic pressure of 350 Pa. MER and Pathfinder performed their functions at deployment Mach number up to 1.8 and dynamic pressure up to 780 Pa. [3] The MSL parachute deployment condition was based on the qualification of a 21.3 m chute, with a configuration of Mach upper limit set up to 2.2 and dynamic pressure below 700 Pa. The following chart was elaborated for the MSL mission, and compares the MSL deployment conditions with prior tests and missions.

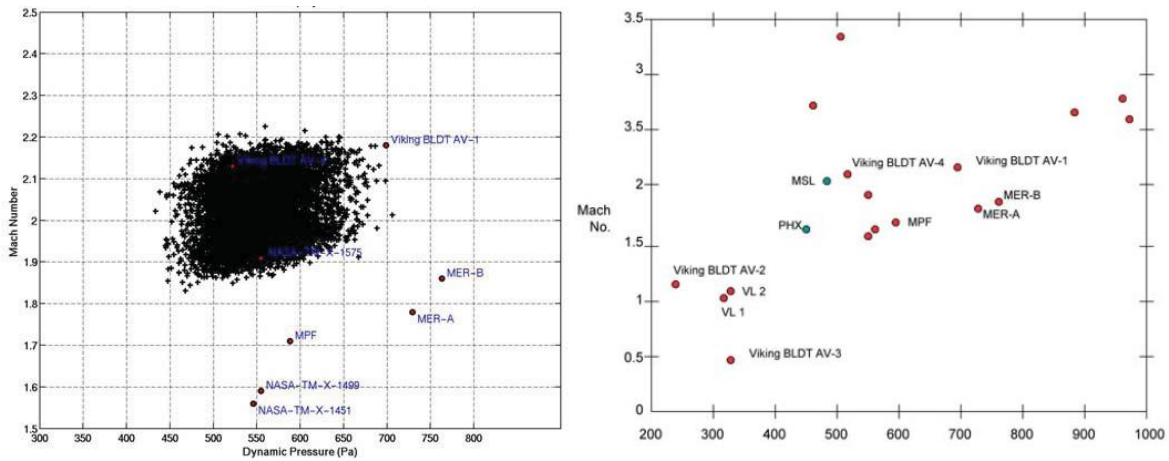


Figure 10 – DGB qualification regions [7]

Is possible to underline a region that constraints the trajectory of a Viking-derived EDL : in order to deploy a supersonic parachutes the spacecraft should respect the region’s limitation. This region is bounded by an upper Mach number of 2.1, and lower value of 1,1 and maximum dynamic pressure of 1200Pa, and lower value of 120 Pa. There’s also a slightly limitation in the deployment altitude, set at 5 km MOLA: this constraint is related to the further available time for deceleration , considering the final condition imposed by the supersonic deceleration phase and the targeted landing site elevation [3]. In the next figure the Mach Box is coloured by red.

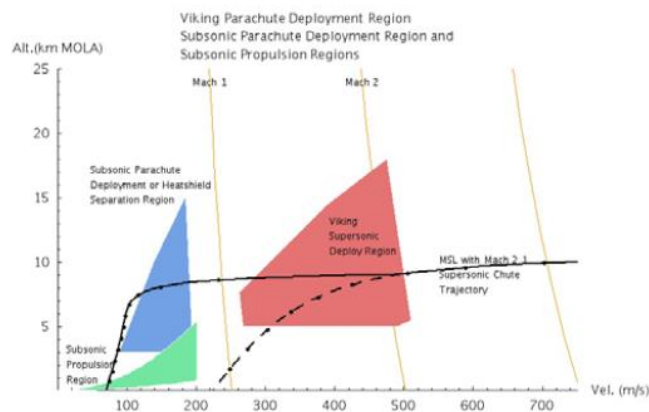


Figure 11 - Parachute deployment region, Mach Box [3]

The trajectories obtained as function of β , reveal how the augmentation of the ballistic coefficient represents an important limitation and constraint for the vehicle in order to fall within the range of the so called “ Mach box” .High β entry systems will either reach the parachute deployment Mach limit at lower altitudes, with a loss of timeline for the subsequent deceleration, or will fall short of the parachute deployment region and therefore won’t be able to use the parachute as a supersonic decelerator. In addition, these augmented mass systems will break out the Viking qualification regime with respect to parachute size, enlarged to correctly scale larger aeroshell diameters. When β gets above approximately 150 kg/m^2 , the trajectories fall below the supersonic parachute deployment region and a Viking parachute cannot be used for aerodynamic deceleration. [3] Without modification related to the phases preceding the parachute deployment, high β entry vehicles won’t be able to land on Mars with this architecture.

1.5 Future robotic Mars mission

The next class of robotic missions will be characterized by payload masses larger than 1-2 tons. To adopt the Viking derived EDL technologies, some solutions must be implemented to overcome the limits listed above. The strategies might be acting either on the reduction of the ballistic coefficient and on the enlargement of the Mach box.

The reduction of β below certain values will enable the achievement of the entry and descent phase through the exploiting of the aerodynamic characteristics of the aeroshell, thus removing the need for a supersonic decelerator.

However, the reduction of β through the use of the blunt 70° sphere cone aeroshell will lead to a considerable increase in the aeroshell diameter, contrasting the launcher packaging constraints and ignoring the proportionality existing between β and the diameter.

To date, inflatable or deployable entry aeroshell are valid options for reducing the ballistic coefficient, even though they will be mainly employed in the transition from the hypersonic regime to supersonic one, and so a different deceleration means will be employed for the following phases.

The enlargement of the Mach Box region, will ease limitations in terms of Mach numbers and pressure, allowing the parachute to deploy earlier in the time window of the EDL descent phase. The extension of the region shall be possible using materials able to withstand both larger dynamics and thermal load. Moreover, larger diameter parachutes will improve the chute performance expanding the supersonic envelope decreasing the lower bound, and increasing the right lateral limit. To achieve the desired enlargement, tests in relevant conditions will be mandatory to demonstrate the correct behavior of the systems and highlight any instability. [3]

An analysis of a robotic mission able to deliver 1500 kg of payload to the Mars surface, comparing various parachute designs based on an MSL entry vehicle, has been carried out in ref [10], in order to lay the baseline for further studies and analyses for robotic missions characterized by 1-2 tons of payload. To maximize the parachute performances and reduce the chute dimensions, the entry MSL capsule's lift to drag ratio was enhanced to 0.3, the capsule's diameter was defined 4.5 m, and the deployment Mach number was fixed to 2.5. The MSL aeroshell was also considered able to package 1500 kg of payload.

Table 2 - DGB and ringsail parachute comparison

Parachute		DGB		Ringsail	
Single Parachute					
Diameter (m)		32.5		31.5	
Deploy Mach		2.5		2.5	
Two-stage Parachute					
1 st Diameter (m)	2 nd Diameter (m)	21.5	41.5	21.5	41.0
1 st Deploy Mach	2 nd Deploy Mach	2.5	1.5	2.5	1.5
Reefed Parachute					
Reefed Diameter (m)	Disreefed Diameter (m)	21.5	>34.0	21.5	34.0
Reefed Deploy Mach	Disreefed Deploy Mach	2.5	2.0	2.5	2.0

The result of the study was that all the parachute solutions listed in table 2 were able to land 1500 kg on the Mars surface, using a scaled MSL type vehicle. Considering the single stage, the two stage, unreefed

and reefed configuration explored with DGB and Ringsail parachute, the technology that showed the most promising performance and capability was a single 34 m reefed supersonic Ringsail.

A reefed parachute is a parachute, or cluster of parachutes, that opens in stages to improve the probability of a successful deployment, especially with large diameter design.

Then, the Ringsail parachute overcame the DGB performance in terms of stability, also reducing mass and complexity while increasing flexibility to tailor the drag deceleration as needed.

Both this technology, and the DGB 32.5 diameter parachute are 50% larger than every Viking derived parachute tested, providing 2.3 times the drag that MSL performed. Even though the challenges related to the development of this new technology, in terms of costs, qualifications, and tests complexity, a TRL of 3 is actually been reached and represents a starting point for the future application of those systems for enabling large robotic class missions. [10]

Chapter 2

Supersonic retropropulsion for human Mars exploration class missions

2.1 Aerocapture

While the dissertation about future larger robotic class mission involves considerations and studies about 1-2 tons payload, a human Mars exploration seems to regard ten times the previous number, introducing a difference of 1 magnitude order in the desired payload to land.

To highlight the difference between these classes of mission and the previous ones, different studies dated 2000-2010 address the topic. In these studies, the analysis of the possible solutions able to face the challenges related to land tons of payload with a precision of tens of meters was taken into account. The assessments and evaluation elaborated in these years furnished a solid baseline for the development of the NASA works.

The first difference underlined with the robotic mission was in the part involving the entry phase. The atmosphere entry could be implemented with direct entry or orbit insertion. If the direct entry is convenient for ease of operations, and saving of mass, the orbit insertion decreases the deceleration peak and allows an analysis of the atmosphere condition, related to the favourable or bad weather to land. Meanwhile in the robotic class missions the acceleration loads are considered essential for their impact on the structure, in a manned mission, is important to preserve the human condition inside the spacecraft: for this reason, the reduction of the deceleration peak is a key-point that drives the choice between two different entry approaches. [11]

The orbit insertion could be realized with either aerocapture or propulsion. Trade between these two techniques was realized by NASA. [12] The analysis was conducted considering risks, cost, and mass saving estimations; even the qualitative nature of the assessments, the analysis highlighted the mass savings obtained with the aerocapture instead of the propulsion manoeuvre. The augmentation in the TPS mass was balanced by long terms advantages, and the difficulties related to the implementation of such manoeuvre, never tested, were defined relatively small with respect to the larger more challenging EDL system development costs and risks. Once the orbit insertion method was defined, other advantages and drawbacks brought by the aerocapture were depicted:

- Reducing the total architecture mass ;
- Less sensitivity to changes in payload mass
- Minimal TPS impact
- Dual use of TPS (increase overall risks).

In conclusion, the aerocapture was defined as easy manageable with moderate issues, and a viable option for the entry phase within the framework of a human Mars exploration class mission.

The manoeuvre is composed of three main phases. In the first phase the spacecraft, after the cruise stage on the hyperbolic orbit from Earth, passes through the Mars atmosphere. The atmospheric drag slows down the S/C reducing its kinetic energy and implementing an ellipse's root, with a trajectory that reminds an Hohmann transfer. Through the passage into the atmosphere, the hyperbolic relative velocity evolves into that which competes with an elliptical orbit. In the second phase, when the spacecraft approaches to

the apoapsis of this ellipse, an acceleration ΔV is furnished and allows to raise the periapsis, realizing the orbit circularization. In the end, once the vehicle arrives at the periapsis, some energy is spent to correct eventual orbit errors related to the propagation in a non-ideal environment, characterized by all the space perturbations to the two body predicted trajectory.

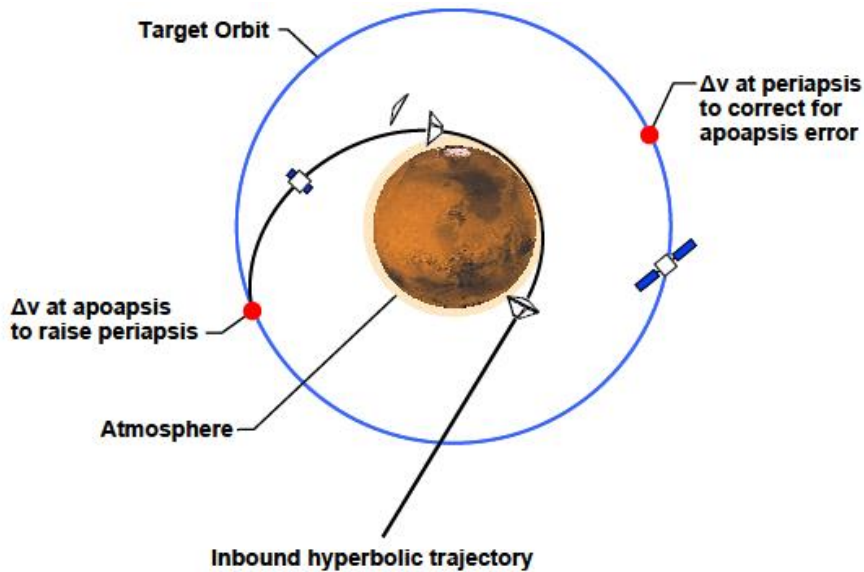


Figure 12 - Schematic representation of the Aerocapture maneuver [11]

The system architecture adopted in the aerocapture scenario is not standardized; three different architectures were compared and evaluated by the NASA Entry Descent and Landing Study Analysis Team in 2008. Moreover, these studies have been elaborated also exploiting the results obtained by Wells, Braun, Lafleur, Verges, et al. in reference [11] for the architecture with a mid L/D 70° aeroshell, derived from the Viking program; in their work, a parametric and optimization study on the mid L/D 70° blunt cone shape aeroshell was computed. The number of parameters manageable was huge, and some of them were considered as assigned and fixed. Considering the 70° aeroshell, with an L/D value set to 0.3 the main constraints that drove the definition of the trajectory involved were the flight path angle, in its shallow and steepest value, and the maximum deceleration peak, set to 5 g, related to the human presence on the spacecraft. Those two main factors resulted in the definition of an envelope curve that established the width of the flight corridor, and related the flight path angle with the entry speed.

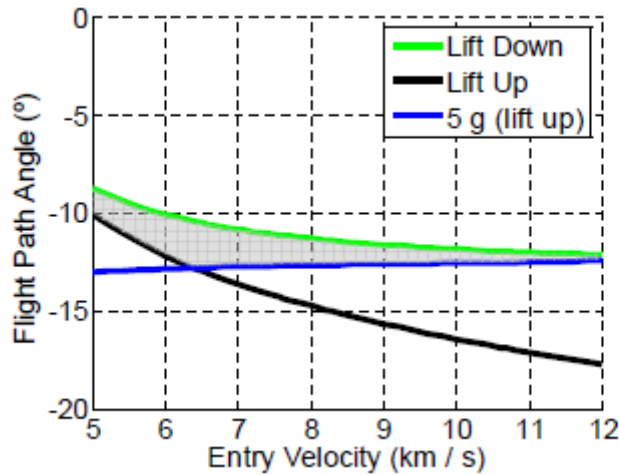


Figure 13 - Aerocapture width corridor for mid $L/D=0.3$ 70° aeroshell [11]

The result of the study was showing the validity of the rigid mid L/D aeroshell, which was able to remain within requirement on flight path angle, entry velocity between 8.8 and 6 km/s, and maximum g acceleration for the aerocapture phase.

The other options analysed by the EDL SA Team were a 23 m diameter inflatable aeroshell, (HIAD), and a larger HIAD, with a 55 m diameter. The results of the studies are contained in reference [13]. Briefly, the altitude profile, nominal bank profile, altitude rate, required ΔV , and TPS size are obtained. Different parameters are considered, i.e. the ballistic number and L/D , in order to show the optimization of the manoeuvre with the different aeroshells. However, what the EDL SA Team study underlined, was the possibility to consider also these two architectures, together with the rigid aeroshell, as viable means for the aerocapture phase.

Moreover, considering just one of those possibilities is useful to understand how the classical EDL approach, derived from Viking and based on the legacy of the past robotic mission, is not suitable to the characteristics of a human Mars mission. The differences with the past previous mission are notable after the aerocapture, when the spacecraft is going to de-orbit and perform the entry in the Martian atmosphere: the altitude, time, and speed condition derived from this phase prevent the application of classical deceleration methods.

2.2 Parametric studies for entry and descent phase for human Mars class exploration missions

Parametric studies with the mid L/D rigid aeroshell, considering an entry speed of 4 km/s and fixed trajectory enclosed in the flight corridor were elaborated by Braun and its colleagues, in ref. [11] Different features competed in the performances of the spacecraft and determined the conditions useful to study the deceleration methods of the supersonic phase.

In the parametric studies were considered different Mach conditions, lift down or lift up trajectories, single-use heatshield (1 for aerocapture and 1 for EDL) or dual-use heatshield (both aerocapture and EDL), different aeroshell diameters 10-15 m, different payload masses, and L/D values of 0.3 and 0.5.

The results of the studies cleared the road for the NASA's work two years later, where alternatives architecture to those used in robotic missions were considered, and elaborated in order to constitute the basis for the studies focused on the technologies enabling a human mission on Mars's surface.

A similarity among the human class mission and the robotic mission is the strong dependence upon the ballistic coefficient: indeed, this value drives the deceleration from an entry speed to a Mach number at a certain altitude. This dependence tends to prefer large aeroshells, that reduce the coefficient and so enable the same Mach number at higher altitude.

The single-use heatshield, jettisoned after the aerocapture, reduces the entry mass, thus decreasing the ballistic coefficient and so having the positive effect described before.

Reducing the L/D ratio, while maintaining constant the lift and increasing the drag, results in an altitude augmentation at fixed Mach number. This characteristics, coupled with the previous one, increases the available time for EDL operations.

The most notable question regards the behavior of the red lines, the Mach 2 lines, related to the behavior of high mass systems. In many situations is not possible to reach the classic supersonic condition of Mach 2, expected to start the supersonic deceleration, before hitting the ground. As the mass increases, even for Mach 3 there's not an improvement in the trend of the curve. Hence, this trend suggests that the initiation of supersonic deceleration close to Mach 2 condition, used from Viking to MSL missions, won't be feasible with the human class mission. Therefore, the large masses intended for these missions will require a deceleration even before Mach 3-4, overcoming the dynamic limitations to which the previous methods were subjected.

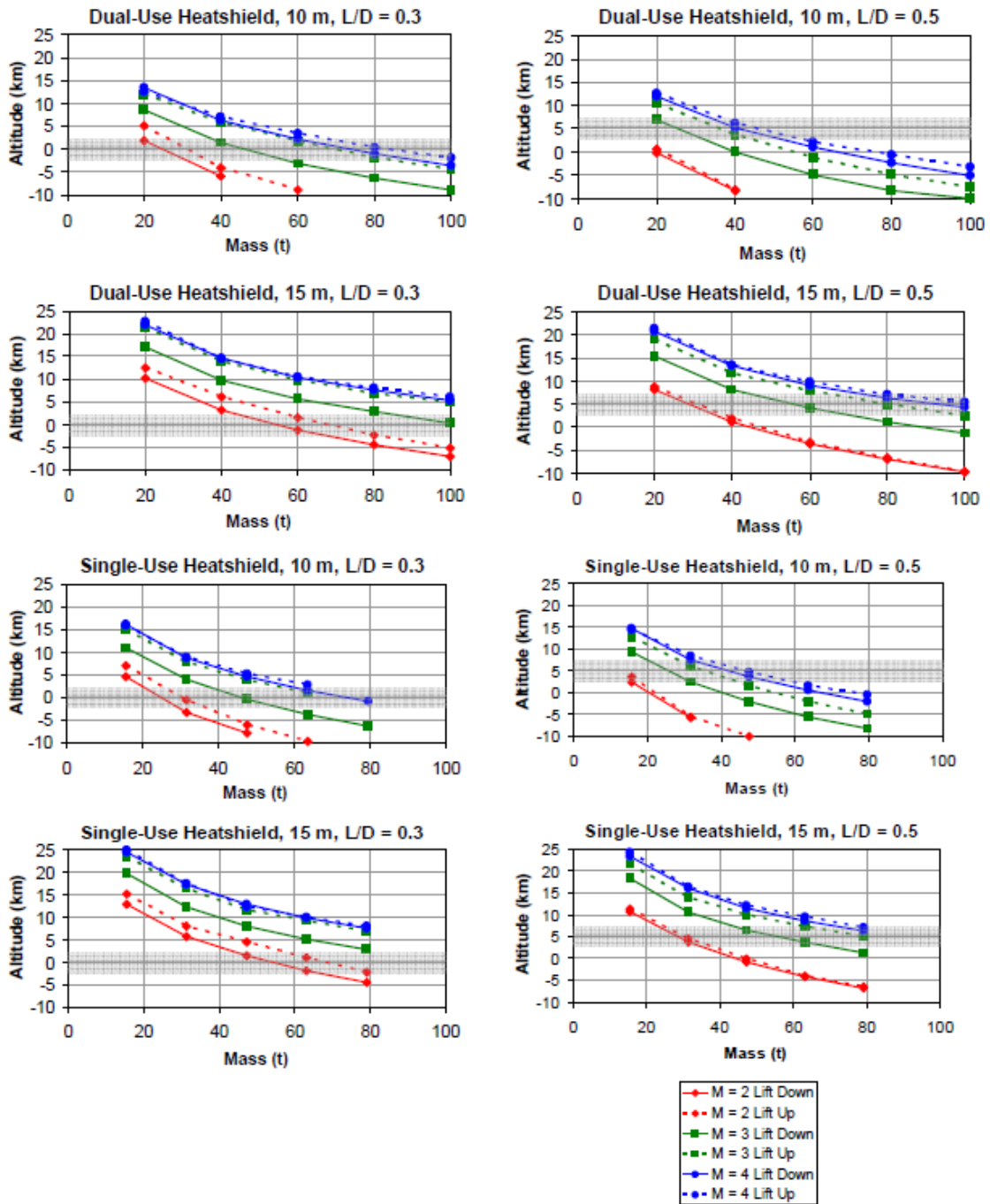


Figure 14 - Mach 2 3 4 transition altitude as a function of L/D, entry mass, single or double use heatshield, heatshield diameter [11]

In order to strengthen the previous supposition, investigations regarding the use of parachutes for heavy systems were carried out, starting with the condition set by the parametric study about the behavior of the rigid mid L/D aeroshell.

At first strong assumptions regarding opening conditions and size were considered: in the simulated scenarios two possibilities with opening Mach numbers of 3 and 2 were taken into account with a parachute diameter of 30 meters. The nature of these assumptions is quite far from the SOA described and

predicted for robotic class missions, however their use is useful to understand the limitations related to the adoption of the parachutes within the descent phase of heavy payload missions.

The use of parachutes was thought as a support for a retropropulsion deceleration, in order to reduce propulsion masses. However, the results underlined advantages lead to the use of the chutes, with its opening at Mach 3, only if the gravity turn phase, and so the burn initiation, took place at Mach 2. Considering an immediate ejection of the chutes at Mach 3, no advantages were found. These advantages consist of the increase of the landed mass, the reduction of propellant masses, and Delta V required.

To quantify the reduction, the mass budget of the backshell, heatshell, propulsive system, and RCS was elaborated with and without the parachute before the supersonic deceleration. The result revealed a reduction of the total mass of the EDL systems only if the parachute size was contained within 2-4 % of the total entry mass and for landed payload greater than 40 tons. Only in this situation the chute's option outperform the all-propulsive deceleration. Moreover, the total benefits lead by this case were extrapolated by a mass comparison for a 60 tons landed payload, same aeroshell configuration, and parachute mass of 3%.

The result of the studies clearly demonstrated the low advantages in terms of saved mass with the use of the chutes, underling how the difficulties related to the development, qualification, and test of this technology won't balance the benefits of its application.

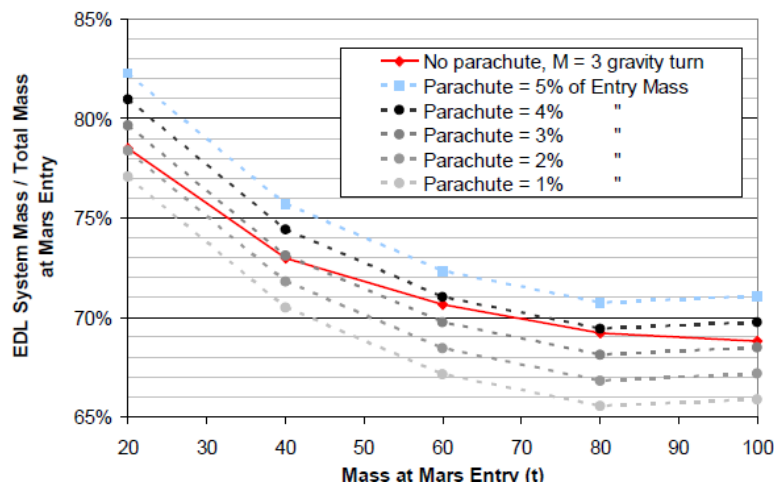


Figure 15 - EDL mass versus Total mass at entry with payload mass set to 60 tons, [11]

Furthermore, these outcomes were elaborated with the assumption of a 30 m diameter parachutes; but, in addition to the low advantages previously depicted, is notable that the chute's diameter grows proportionally to the landed mass, as shown by the following figure.

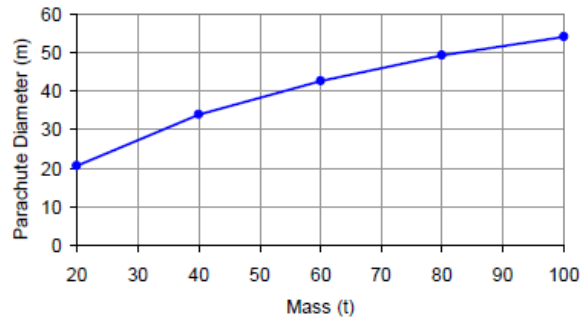


Figure 16 - Parachute diameter chose to allow a supersonic deceleration from Mach 3 to Mach 0.8, starting from 2 km of altitude, with mid L/D rigid 70° cone shape aeroshell 15 m [3].

In addition to the mass drawbacks, opening time penalties and package considerations shall be examined, and the advantages of such architecture weight against all the aerodynamic and spatial issues led to the parachute adoption.

Even if the parachute could be used to jettison the payload from the aeroshell , to reduce the total amount of propellant for the deceleration , and to ease propulsion requirements, decelerating large mass from high entry speed to lower velocity, the large mass entry systems related to human Mars class mission, prevent the use of this method.

In conclusion, the deceleration through aeroshell and DGB is considered likely impractical. This consideration posed important question about the EDL phase for human missions, as far as the complexity of this phase linked to the robust tough event sequencing timeline and presence of crew onboard, requires reliable deceleration method, tested and with low margin error percentage. Further study including large aerodynamic supersonic decelerators and other means to slowdown the spacecraft during the transition from supersonic to subsonic, started to represent a fundamental concern in order to design a feasible human Mars exploration.

2.3 EDL SA and human exploration of Mars DRA 5.0: studies and assessments

Mean, the development of the robotic class mission, NASA in 2005 paved the ground for the next two decade agency's mission regarding human presence exploration. During the studies of the Lunar architecture was recognized that the lunar definition shall be conducted in an environment that considers the most likely follow-on mission. After recognizing the need for an updated and unified reference architecture for human mars exploration, NASA headquarters commissioned the Mars Architecture working group, a multidisciplinary team, involving different NASA mission directorate with the aim of developing the Mars Design Reference Architecture 5.0.

The purpose of the MDRA 5.0 is to provide a common framework for future planning of system concepts technology development and operational testing, indeed providing a vision of one potential approach to human Mars exploration, based on the estimation known; is also provided a common reference for integration between multiple agency efforts, research conducted in the ISS, and future mission plan for lunar exploration. The MDRA 5.0 describes the systems and operations that would be used for the first three mission to explore the surface of Mars by humans. [12]

Despite the huge work and considerations that cover the complete design for future Mars human exploration, the work is focused on the use of supersonic retropropulsion as a viable means to decelerate large entry mass in the range of 20-100 tons, that represent the probable payload needed to establish a human presence on Mars. Moreover, all the results involving the launch phase, cruise phase, landing issues related to Mars surface, system designed for a manned mission, mission goals and objectives, in situ issue for human sustain, alternative propulsion for cruise, trajectory and orbit analysis and optimization studies won't be considered in this dissertation.

Assuming the validity of past work and basing on the considerations and performance of the past landed mission, the EDL reference architecture was a hypersonic aero-assisted entry system with mid L/D aeroshell, ejected a low supersonic Mach number, a LO₂/LCH₄ fuel propulsion system used for de-orbit, RCS and terminal descent: the supersonic retropropulsion was designed as the best option to implement the descent phase for this type of mission.

In similarity with the previous work, this architecture uses aerocapture in the first phase of EDL, in order to save mass compared to a propulsion entry. However, two possibilities of aeroshells were undertaken in the DRA5.0 analysis: the 10m x30m, and a larger 12x36 m aeroshell. While the second one increased the ballistic coefficient, the first one resulted the selected baseline, as far as most suitable to the constraints imposed by the launcher shroud(Ares V). Aligned with the previous considerations, the 10x30 m showed advantages in terms of less TPS mass required, due to the reduction in the surface covered by TPS systems, and consistency results for the packaging density historically obtained for human missions. Moreover, the sizing of the TPS depended on the landed payload.

The DRA 5.0 offered for the first time a precise description of a propulsive stage used for SP deceleration. Indeed, the descent stage is an all-propulsive legged lander concept using four pump-fed LO₂/CH₄ engines designed to be RL10 derivatives, but recognizing that the LO₂/LH₂ RL10 may not be the most appropriate analogy to the LO₂/CH₄ engines, some trade studies were elaborate in order to compare the same engine with two different thrusts to weight ratio, remanding to the RL10, with a T/W = 40 lbf/lbm, (4 Earth's g) and RD180 with a T/W = 80 lbf/lbm, (8 Earth's g).

The Envision software was used for the first estimation of the propulsion mass needed for the descent phase. The engine characteristics involved in the process are :

- Isp of 369 seconds;

- Mixture Ratio of 3.5 ;
- pressure in the combustion chamber of 600 psi;
- and nozzle exit area ratio of 200.

Therefore, taking into account the 40t payload design mass , for 1 sol orbit , the 10 m x 30 m aeroshell jettisoned before the engine start-up, 2 g constant entry profile and a 3 g maximum acceptable acceleration , a mass evaluation was elaborated.

Table 3 - Mass sizing for EDL , elaborated by the DRA 5.0 team [12]

Baseline 1-sol orbit, 10 m x 30 m Aeroshell, 40 MT Payload, 2g entry, T/W _{sys} = 3g's, T/W _{eng} = 80 lb _r /lb _m , 30% delta-V margin.		
Capture to 1-sol orbit		Aerocapture
Arrival Mass	kg	115,549
Post-AC Orbit Insert Prop	kg	4692
Orbit Mass	kg	110,857
Deorbit Propellant	kg	458
Entry Mass	kg	110,399
Aeroshell Structure	kg	22,500
TPS	kg	14,600
RCS Dry Mass	kg	994
RCS Prop	kg	1,218
Terminal Descent Prop	kg	13,887
Pinpoint Landing Prop	kg	3,030
Landed Mass	kg	57,200
Dry Descent Stage	kg	17,200
Payload Mass	kg	40,000
Deorbit DV	m/s	15
Ballistic coefficient	kg/m ²	475
Descent DV	m/s	600
Max heat rate	W/cm ²	462
Total heat load	MJ/cm ²	597
Altitude engine initiation	m	1,455
Mach at engine initiation	M	2.30
Time of flight	sec	494
Time at constant g's	sec	132

The mass sizing realized in the framework of DRA 5.0 is the baseline for the following studies useful to validate new EDL methods and technologies that improve and develop the basic concept enclosed in the report. Likewise , the data regarding Mach engine initiation, and altitude engine initiation are a starting point for the computational analysis that enable the validation of such technologies.

Other methods were mentioned as an alternative to SRP, i.e. supersonic and hypersonic aerodynamic inflatable decelerators, rigid hypersonic deployed aerodynamic decelerator that may reduce the ΔV requirement and loosen up the conditions for the subsequent subsonic propulsion. However at the SOA when the DRA 5.0 was drafted, these systems were felt to be lacking in detail to be considered.

Considering the EDL baseline architecture of DRA 5.0 as a rigid mid L/D aeroshell used both for aerocapture both for the hypersonic deceleration, and SRP in the descent phase, the lack of alternatives required ulterior studies in order to identify other technologies to successfully land a human payload on Mars surface.

The role of the EDL SA Team , was to analyse whether the EDL configuration used as reference by DRA 5.0 was viable solutions or other methods shall be implemented. The result of the brainstorming held by EDL

SA team was that supersonic retro-propulsion with rigid or flexible aeroshell remained the most viable means to decelerate the spacecraft from hypersonic to subsonic speed. [10]

The EDL SA team through one year of work elaborated a set of different architectures, based on five common elements:

- Rigid mid L/D aeroshell ;
- Lifting Hypersonic Inflatable Aerodynamic decelerator (LHIAD);
- Supersonic Retro Propulsion ;
- Drag Supersonic Inflatable Aerodynamic Decelerator (DSIAD);
- Deployable Lifting Supersonic IAD with Skirt ;
- Dual pulse TPS;

The combination of these technologies lead to the elaboration of eight different architectures that mainly differ in the employment of elements in the deceleration from hypersonic to supersonic, and then from supersonic to subsonic.

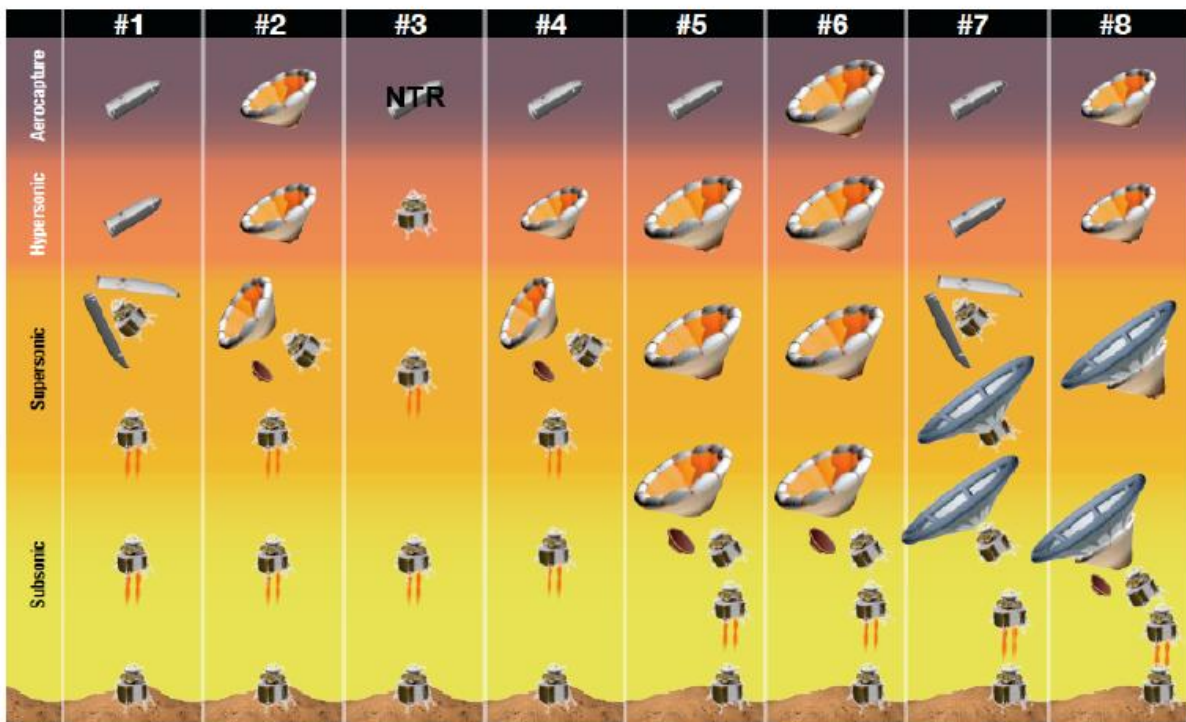


Figure 17 - Exploration class architectures [10]

All the architectures rely on two main systems to implement the hypersonic phase : the rigid mid L/D aeroshell, and the Hypersonic Inflatable aerodynamic decelerator. The first one belongs to the rigid aeroshell decelerators class, the second one is representative of the flexible aeroshell. Both these means deemed to be a reasonable method to achieve this phase.

An example of a rigid mid L/D aeroshell is the ellipsoid, used in DRA 5.0, with an elliptical nose and cylindrical aft section. The design provided in the previous work was leveraged and improved : the 10m x30m aeroshell, with hemispherical nose cap and straight barrel section, displayed, once again, compliance with launchers requirement (Ares V) and proved excellent aerodynamic performance, with simulation covering Mach 1.3 through 50 and AoA 0° through 90°, dynamic pressure of 1.E-7 through 0.75 bars., and optimal structural performance, in terms of FEM analysis and mass sizing. One main peculiarity that

distinguishes the aeroshell from the previous one was that the L/D ratio, enhanced from 0.3 to 0.5, at an AoA of 55°.

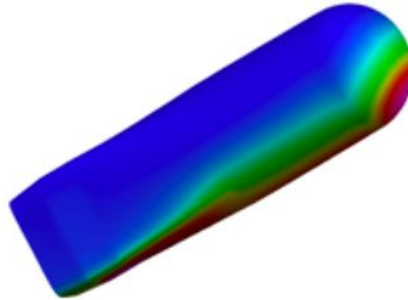


Figure 18 - Aeroshell aerodynamic analysis performed with DPLR code [10]

The EDL SA team, demonstrated also the validity of the HIAD, with a 23 diameter, as an alternative to the aeroshell employed in the aerocapture and hypersonic entry phase. Aerodynamic analysis, covering Mach 1.3 through 50, AoA of 0° through 90°, dynamic pressure to 1e-7 to 0.75 bars, and structural FEM analysis proved that the low L/D, equal to 0.3 flew at 20 degree, flexible aeroshell could substitute the rigid aeroshell in this phase, also leading to important mass savings.

Besides the difference on TPS sizing, depending on flexible or rigid aeroshell, both the methods were described as the only solutions for aerocapture and hypersonic entry, therefore becoming the pillars for these phase for human Mars exploration class mission, and paving the way for further work that shall increase the TRL levels of both these technologies.

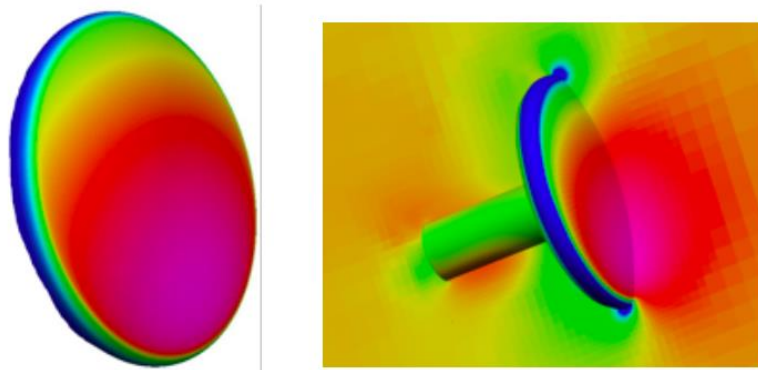


Figure 19 - CBAEREO and DPLR solutions for flexible aeroshell.

The set of the eight architectures, actually represent the backbone in the field of human Mars exploration class mission. The work of EDL SA team was conceptually intended as a mission phase 0-A project, focused only on the aerocapture and EDL of the mission, where different solutions to a problem were evaluated and compared. An assessments of benefits and drawbacks for each configuration could lead to the acknowledgment of the best choice between these possibilities. The understanding of the best architecture has driven the further studies, aimed to increase the TRL level of the technologies involved.

A first comparison between the architecture is based on the mass estimation involved in every solution and on the qualitative considerations about the timeline sequence depending on the deceleration means.

All the architectures are however depending on the same entry, descent and landing strategy and upon important common features that were provided by the DRA 5.0 studies, including:

-Hyperbolic approach velocity set at 7.36 km/s ;

-Target orbit a 1Sol (33793 km x 250 km);

-EDL initiation from the 1 Sol orbit ;

- Deceleration profile within the acceptable margin for a deconditioned crew. [12]

The entry phase includes deorbit, with its related ΔV , atmospheric entry , set at 3255.2 km, pullout manoeuvre and heading alignment, aimed to undo the azimuth error to the landing site at engine initiation.

The starting point of the descent phase is the separation of the drag device used in the aerocapture and entry phase, that requires a certain amount of time depending on the selected architecture, and so, loses the instantaneous hypothesis hold in the DRA 5.0 description: in order to safely divide the aeroshell to the spacecraft, a free fall motion is ensured for a given amount of time. Afterward, the descent phase is governed by the necessity of saving fuels implementing the maximum throttling, set at 80 %, until the maximum nominal acceleration is achieved , and then fly a linear velocity profile in compliance with the altitude change.

The landing phase , involving the touch-down , is based on Viking heritage: when the vehicle reaches 2.5 m/s the velocity is maintained constant until the vehicle reaches the ground at 0km MOLA altitude.

The results achieved by the Mars Architecture Working Group (MAWG) team led to the studies of the DRA 5.0 reference architecture for the EDL phase, namely "architecture 1": thus, as previously depicted, the DRA 5.0 proposed method, still remained a valid solution remarkable of further investigation. The EDL SA team improved inherited knowledge slightly modifying the flight trajectory optimization through guidance's algorithm.

A brief summary of the eight discussed architectures is presented, in order to understand how the supersonic retro-propulsion represents the best choice for the descent phase for this type of mission. All the analysis and results derived from parametric studies with 40 tons useable landed payload and were implemented with POST2 and with Monte Carlo for the dispersion analysis ,that won't be reported here.

- 1) Architecture 1 leveraged the structure elaborated in DRA5 changing slightly the vehicle aerodynamic configuration. As depicted before, the architecture relies on the mid L/D rigid aeroshell for aerocapture and hypersonic flight, which flies at 55 degrees AoA with L/D 0.5, and supersonic retropropulsion starting at 4.6 km above the ground with dynamic pressure of 1721.8 N/m² , Mach number around 3 a T/W system ratio set to 3 g and T/W engine ratio set to 8 g. The total arrival mass is found to be 110 tons , showing compliance with the previous results underlined in the DRA 5.0 studies and implying that the hypotheses made during the elaboration of the DRA 5.0 were adequate. The use of aeroshell coupled with supersonic retropropulsion enhance the TRL of Architecture 1 : if the aeroshell is largely employed with robotic class missions , the propulsion has always been applied in the subsonic phase. Thus implies considerable efforts in adapting these technologies to larger systems and different flow fields, nevertheless valued less onerous than the processes needed to validate other technologies.
- 2) Architecture 2 uses the HIAD for aerocapture and entry, followed by supersonic retropropulsion, for the terminal descent. The HIAD flies with an AoA of 22°, L/D of 0.33, and supersonic retropropulsion starting at 3.3 km above the ground with dynamic pressure of 881 N/m² and Mach number around 2. The use of an HIAD mitigates the operation condition of SRP but also reduces the available time for the terminal descent phase. Moreover, the use of HIAD allows a mass saving of 25 tons of arrival mass compared with Architecture 1. These benefits are balanced by the low TRL associated to the HIAD linked to the use of a dual-use TPS , packaging issue and separations dynamic environment. [1]

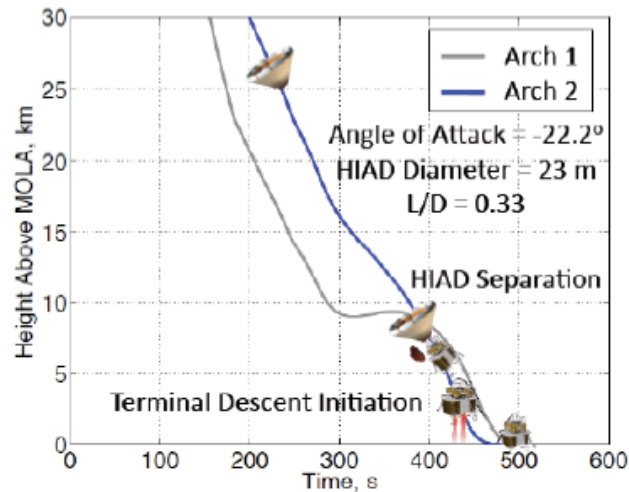


Figure 20 - Comparison between Arch 1 and Arch 2 in terms of time , trajectory and terminal descent initiation altitude [10]

- 3) Architecture 3 is characterized by an all propulsive configuration. Some fundamental hypotheses were adopted to ease the calculation : no drag and no heating characterized the flowfield, reducing the computational cost and the design complexity. The result of this simplified simulation was an increase of the arrival mass of 300% ,in the lowest weight configuration, compared with architecture 1, and a relatively high TRL linked to the adoption of tested engines for the smaller class missions. The baseline engines, as for DRA 5.0 , are the LOX/LCH4 , with a specific impulse of 369 s and a T/W ratio relying upon the arrival mass selected. With a constant Isp, the T/W ratio is inversely proportional to the required ΔV , and with no drag, increases as the arrival mass increases. A second calculation was needed to involve the drag effects: while the trajectory optimization shall avoid the heating concerns, considering the drag varies the behave of the T/W ratio depending on the arrival mass. As the thrust increases, the altitude of engine initiation drops , augmenting the aerodynamic drag losses. The increase in drag losses causes the reduction of propellant employed in the deceleration phase, thus reducing the arrival mass and causing an oppositely behaviour with respect to the no-drag situation. The relatively high TRL associated with Architecture 3, related to the technologies employed, is balanced by many uncertainties associated with a whole propulsive EDL: flow stability, vehicle dynamics, nozzle external and internal performance, and flowfield interaction of the rocket plume are just some of the aerodynamic issues remarkable of further studies and assessments.
- 4) Architecture 4 introduces the innovation of switching between the aeroshell and HIAD when passing from aerocapture to the entry phase. Instead of the utilization of the dual-use HIAD ,i.e. in Arch 2, for aerocapture and hypersonic phase, the rigid aeroshell used in aerocapture allows a reduction on the entry mass despite the augmentation of the arrival mass related to the adoption of both systems. The mass savaqe related to this architecture may not balance the added complexity bought by the coupling of the technologies.
- 5) Architecture 5 and 6 replaced the descent phase implemented with supersonic retro-propulsion, with the use of a very large HIAD. While the architecture 6 uses the HIAD also in aerocapture , Architecture 5 highlights the mass savaqe related to the utilization of the rigid aeroshells in the aerocapture, while adopting the flexible aeroshell for the following phase. The selected diameters were 68 m and 82 m. An important mass savaqe compared with architecture 1 was extrapolated by the use of rigid aeroshell coupled with the HIAD , for the architecture 5 . Also the deceleration with the HIAD mitigates the starting condition of the subsonic phase, allowing less strenghen operation constraints for the subsonic propulsion. However , the large diameters

required for both the HIAD systems, in order to obtain the supersonic deceleration, largely exceed every qualification or prototype design test, leading to the same issues related to the development of supersonic parachutes, including packaging and separation challenges. Also the TPS mass models resulted not-suitable to diameters larger than 50 m, leading to wrong assumptions in the mass sizing procedure.

- 6) In compliance with the intent to avoid the use of SRP, Architecture 7 exploits the Supersonic Inflatable aerodynamic decelerator with 51 m of diameter to achieve the supersonic deceleration, while the aerocapture is still realized with the aeroshell. Architecture 7 reduces the arrival mass of 3 tons compared to architecture 1. Another reduction, as for architecture 5 and 6, is inside the throttling range set to 65% instead of 80%. The use of an inflatable aerodynamic decelerator in the descent phase turns down the operative condition for the subsonic deceleration, i.e. the system T/W ratio is reduced to 2.5g. However, the mass advantages are mitigated with the technical challenges related to the SIAD packaging, inflation and TPS adaptation.
- 7) Architecture 8 aims to substitute the supersonic retro-propulsion with a SIAD which follows the aerocapture and entry phase realized with the 23 m HIAD. The simulation determined the size of SIAD equal to 44 m, which was deployed at Mach 2.6, at an altitude of 11.9 km. This early deployment is related to the slow aerodynamic deceleration possible with the SIAD. The combination of inflatables reduces the HIAD mass compared with Architecture 6 of 38 tons, but with respect to the combination of HIAD plus SRP the reduction is around 3 tons, so neglectable if compared to the complexity of this coupling. Indeed, joining these two IADs leads to compression in the EDL timeline and difficult interactions on the deployment of the SIAD during the transition phase.

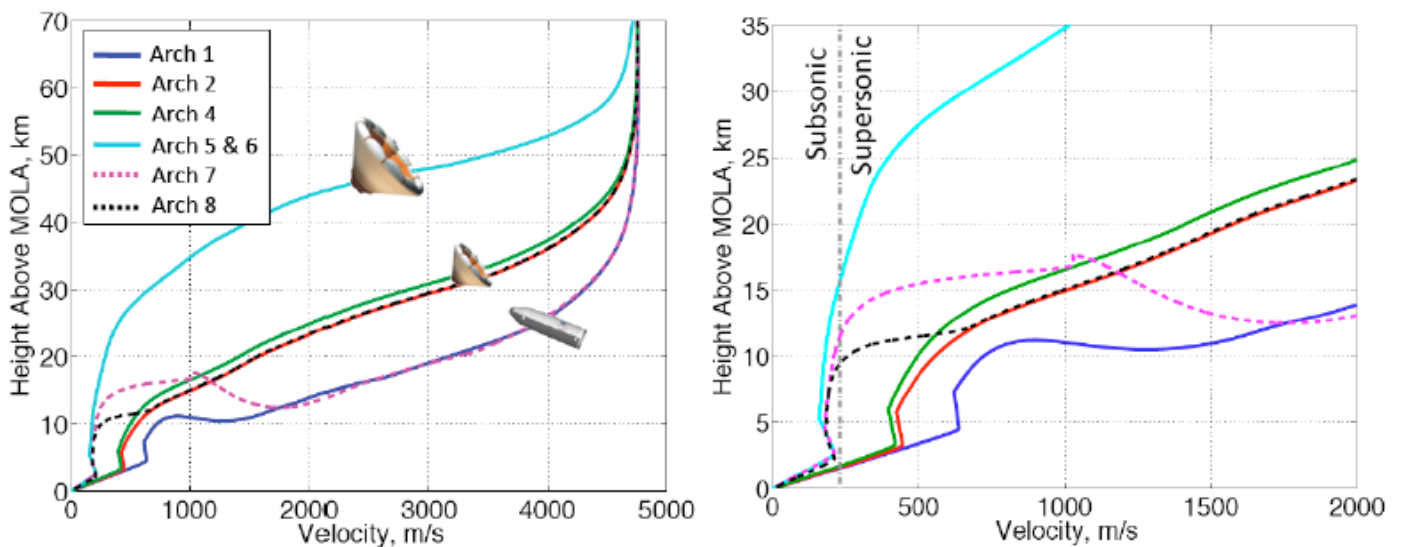


Figure 21 - Altitude versus velocity of the reference EDL SA architectures. [10]

The use of flexible aeroshells allows a higher trajectory in the hypersonic phase. However, the inflation point of each curve indicates the starting point of the descent phase: the behavior of the starting point is regressive passing from architecture 1 to 5-6, indicating a reduction of the available time for the following landing phase. The use of SRP, even if employed at higher speed for the same altitude, permits an increase in the timeline for touchdown, loosening up the constraints for the last EDL phase.

Moreover, the arrival mass comparison is reported for each architecture, aligned with the previous considerations.

	Arch 1	Arch 2	Arch 3	Arch 4	Arch 5	Arch 6	Arch 7	Arch 8
Arrival Mass	110.1	83.6	265.2	109.0	133.5	140.5	107.4	80.6

Figure 22-Mass comparison for the eight architectures

Besides mass and trajectory considerations, carrying and designing separate systems for aerocapture and entry has led to define Architecture 4 and 5 as unlikely candidates for further studies. In addition to packaging, inflation, and separations issue, current TPS mass models are not suitable to inflatable aeroshells with diameters larger than 50 m, leading to incorrect mass modelling for architecture 5 and 6. As depicted by the velocity versus timeline chart, architecture 6, 7, and 8, that use inflatable aerodynamic decelerator instead of SRP, generate a considerable reduction of the available timeline for the terminal EDL phase, and so have been classified as inadequate for human class exploration mission. [10] Architecture 1 and 2 have been so considered as reference for the human exploration class missions. In order to strengthen assumptions and results found in the EDL SA study, other analyses were carried out.

Important considerations were elaborated about the so-called transition event. The transition event is the passing from supersonic flight to power descent, and relative separation of the aeroshell from the lander. The transition event conditions are crucial to define the boundary conditions for the simulation environment.

For the mid L/D architecture, the transition event begins at 7.5 km altitude above the ground and a Mach number of 2.7. Following a trade-off study, either the front exit or side exit clamshell methods were defined as the most appropriate to suit the transition event. The use of one of these methods allows the conclusion of the transition event and the starting of the powered descent phase, at an altitude of 4.6 km and Mach of 2.9.

For the HIAD architecture, the transition event begins at a lower Mach number, 1.8, due to the strongest deceleration related to the use of a flexible aeroshell, and an altitude of 5.7 km. Either the rear exit, the front exit, and the no-aeroshell separation were considered as viable transition methods, and remarkable of further investigations. The end-point of the transition event is already fixed at Mach 2.0 and an altitude of 3.3 km. The whole analysis is depicted in reference [14]

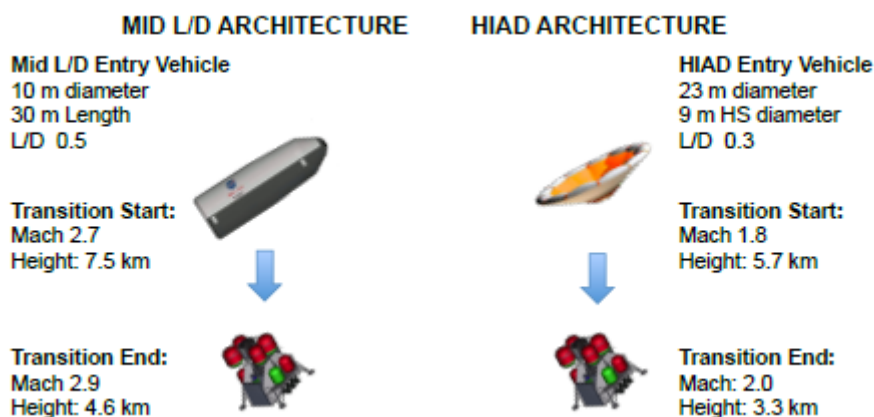


Figure 23 - Boundary condition for transition event for both architectures [14]

In addition to the importance of these considerations upon the global vehicle design and sizing, the data furnished by these analyses are a key-point in the further dynamic simulations regarding the flowfield surrounding the vehicle during the descent phase.

While the development of the last effort that define the SOA for the EDL architectures, namely the Mars DRA 5.0 addendum#2, the agency commissioned a 4-day seminary to JPL's expertise, namely Team X, to independently size and design the systems and technologies involved in the Architecture 1 and 2. The aim of the work was to underline the similarity with the previous EDL SA team's work, and strengthen the assumptions on which the future work of the Human Spaceflight Architecture Team (HAT) should have been based.

The main results of team X studies was defining the sequence of events and elaborating mass sizing. Either the sequence of events and the mass sizing will be reported.

Either for the HIAD and mid L/D aeroshell, the entry started at 129 km, and was followed by the deceleration through the aeroshell, which allowed the passage from the hypersonic to the supersonic flowfield. Both the HIAD and mid L/D, at Mach 3.0 pitched to 0° AoA in order to prepare the spacecraft to the transition phase. This phase started at Mach numbers of 2.96 and 2.02 respectively, and was followed by a free fall motion of 10 and 6 seconds. While for the rigid aeroshell, in a clamshell configuration, the heatshield was jettisoned, for the flexible HIAD configurations the heatshield separations occurred after the initiation of the powered descent. The boundary conditions for the initiation of terminal descent phase, so engine ignition, were Mach number of 2.89 at 7.3 km for the rigid aeroshell, and altitude of 6.8 km and Mach of 2.01 for the flexible aeroshell configuration. The touchdown followed the descent phase, and was defined by a touchdown speed of 2.5 m/s. For the HIAD configuration, the heatshield was jettisoned prior the landing at 1.2km of altitude.

The arrival masses for the mid L/D and HIAD were 98.5 t and 87.5 tons respectively. The results of the study were aligned with the efforts carried by EDL SA Team, and thus constituted the baseline for the initial work of the HAT. The HIAD architecture was more efficient at entry mass, while less volume efficient. Both configurations packaged well in the fairing for EDL, and both required supersonic propulsive engines firing, even at two different starting conditions. [14]

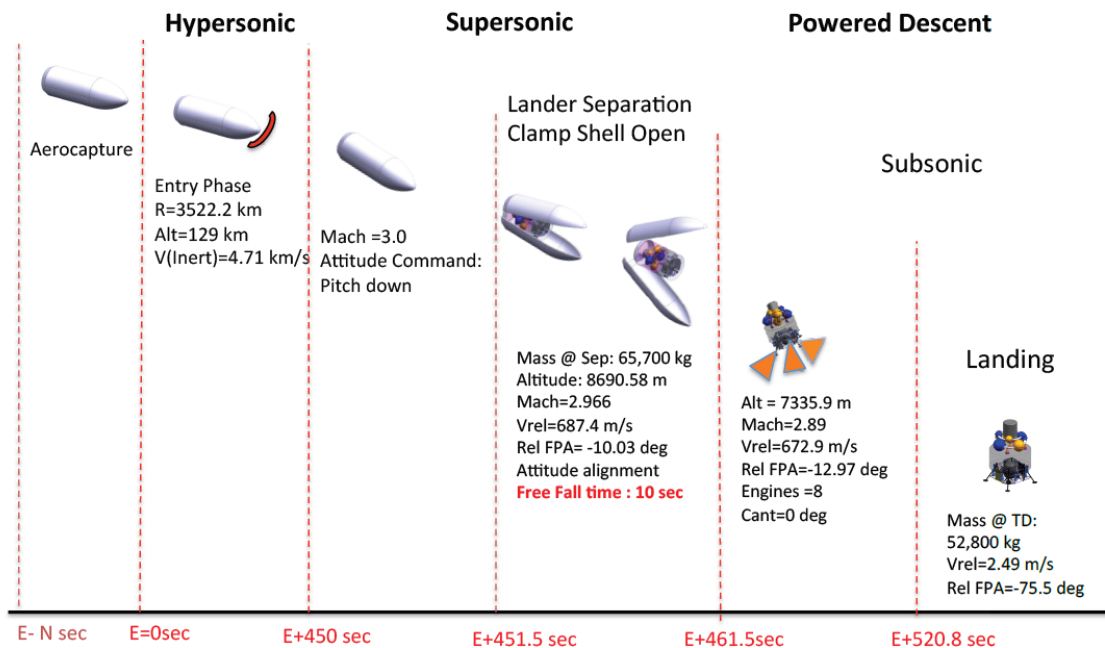


Figure 24 - Event sequence for the rigid mid L/D aeroshell followed by SRP elaborated by Team X [14]

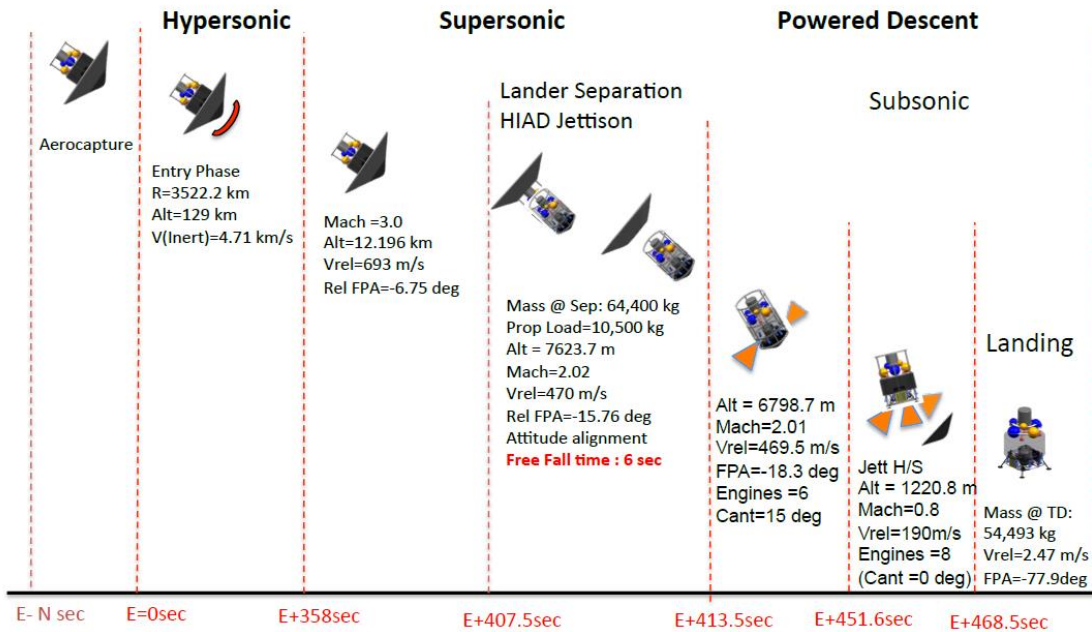


Figure 25- Event sequence for the HIAD aeroshell followed by SRP elaborated by Team x [14]

Indeed the “Design Reference Architecture Addendum #2” report defines the SOA for the EDL architectures; this report was elaborated by the HAT and was strongly based on the EDL SA team and previously MAWG team work.

High-level size investigations in order to elaborate a Mars lander concept were conducted and based on the EDL SA Architecture 1 and 2. The innovation lead by the HAT was the development of a Mars Ascent Vehicle concept, that influenced the configuration and the design of the whole mission. Indeed, the EDL phase was thought to be implemented by a Mars Descent Module, which was based upon all the previous investigations about Mars EDL systems.

Besides the whole considerations regarding trade-off studies on Earth-Mars trajectories, advanced in-space transportations, launch systems, deep space habitat, surface strategies, systems to establish a human presence on Mars surface, human research objectives/goals, and EDL systems, the HAT work defined the SOA for the design of a propulsive system able to implement the supersonic powered descent in Mars condition.

The design of the propulsive architecture of the descent stage was strongly dependent on the MAV concept, that won't be reported here, as far as increasing the commonality between the systems ease the design of the whole structure.

Two different types of propellants were compared : LOX/LCH4 and LOX/LH2. These propellants are both able to utilize in-situ resources, reducing the overall structure mass, which depends on the propellant mass brought from Earth. Even if LH2/LOX has better Isp performance , the LOX/LCH4 is easier to store, reducing cryogenic fluid management requirements, and has also a higher mass density, thus reducing the tank volume.

Therefore, for the conceptual design activity, the LOX/LCH4 propulsion system was selected. The payload mass, including Mars surface human cargo modules and MAV was set to 40 tons , in compliance with DRA 5.0 and EDL SA previous assumptions. The thrust level for the descent stage was found to be 1,2 kN, with a

T/W engine ratio varying from 1.5 to 2.0. At that thrust level, with that propellant requirements and packaging considerations, a turbopump-fed engine was needed. The descent stage would have required 12 engines, too many from a reliability standpoint, so an engine concept was created whereby two thrust chamber assemblies were connected to a larger common turbopump. The result configuration involved six engines with a maximum thrust of 200kN, assembled as depicted in the following figure (26). The specific impulse was 360 second, based upon a moderate combustion chamber pressure that varied from 900 psia to 1000 psia, thus easily achievable through multiple liquid propellant rocket engine cycles; the mixture ratio was set to 3.5. [14]

Different throttle strategies coupled with vertical or horizontal lander strategies and aero-assist systems were examined to understand the impact on payload performance, entry mass, and trajectories optimization. The trade-off studies and results are summarized in ref [14], and represent the SOA for the design of a propulsive system able to implement the supersonic retro propulsion in Mars relevant EDL condition. In the dissertation have been reported just some of the engine characteristics useful for the following simulation analysis.

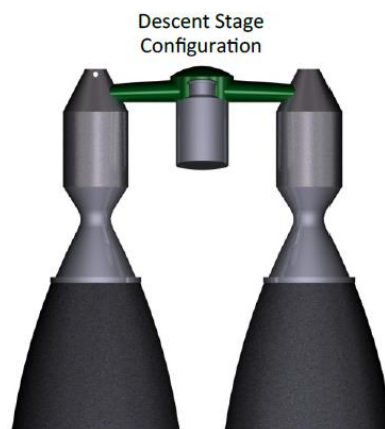


Figure 26- Propulsion system design [14]

Liquid LOX/LCH4 engines are so considered as the reference propulsive design for supersonic retropropulsion, able to execute the powered descent in the framework of a human Mars exploration mission. Even numerous studies have been conducted (from 90 to 400kN of thrust), actually no large throttle engine (more than 300 kN) technology is available, and therefore the TRL is considered quite low. The main concerns are related to throttle considerations: the lower limit for throttling of the pump fed engines is set to 50% because the injector dynamics pump and turbine performance drop off at lower throttle level. A solution might be the adoption of engines in multiples of 3, as designed by the HAT team, in order to reach the 10% of total thrust at the shutdown through low thrust level of just one half of the engine, instead of the whole system. The state of art for this type of propulsive system is driven by development efforts carried out by the Exploration Development Technology Program in the framework of Lunar exploration, with the adoption of a LOX/LCH4 engine for the ascent/descent lunar vehicle. [14]

In order to bring the technology to a good TRL level, allowing the built and test processes, several obstacles must be overcome and among them the most important ones are:

- Interaction between a large nozzle and the unsteady flow stream around the vehicle;
- Engine start-up;
- Throttle limitations;

- Dynamic interaction between the bow shock and supersonic flow field with the mass flow ejected by the nozzle;
- Multiple nozzle interactions in a relevant environment;
- Vehicle structural response to supersonic retro propulsion during the descent phase.

Since 2011 the ongoing work, focused on smaller systems, is developed through CFD analyses, wind tunnel tests and subscale flight tests aimed to overcome the several problems discussed before.

The dissertation is focused on CFD simulation of the flow-field defined by the supersonic retro-propulsion in Mars similar condition, with two different configurations that will be depicted later. A brief introduction about the predicted theoretical flowfield will be described. In order to plenty explain this complex environment, also the description of a blunt body in supersonic flow and high under expanded flow will be presented.

Chapter 3

Supersonic retropropulsion, aerodynamic main features

3.1 Blunt body in supersonic flow field

The blunt body is an important shape in the framework of EDL technologies: the rounded leading edge is the preferred shape for entry vehicle, due to the inverse proportionality between the bending radius and the incoming heat flux.

$$Q \propto 1/R$$

When the blunt body flies into the supersonic regime is always characterized by the formation of a detached shock. The shock envelops the blunt body. The peculiarity of this shock wave relies on the flow field downstream of the shock. The flow behind the nearly normal portion of the shock is subsonic, but when the subsonic flow sweeps over the body it accelerates, expanding and becoming sonic and then supersonic. The shock vanishes far away from the body and its inclination is asymptotically aligned with the Mach waves, bent with the Mach angle, in the direction of the freestream.

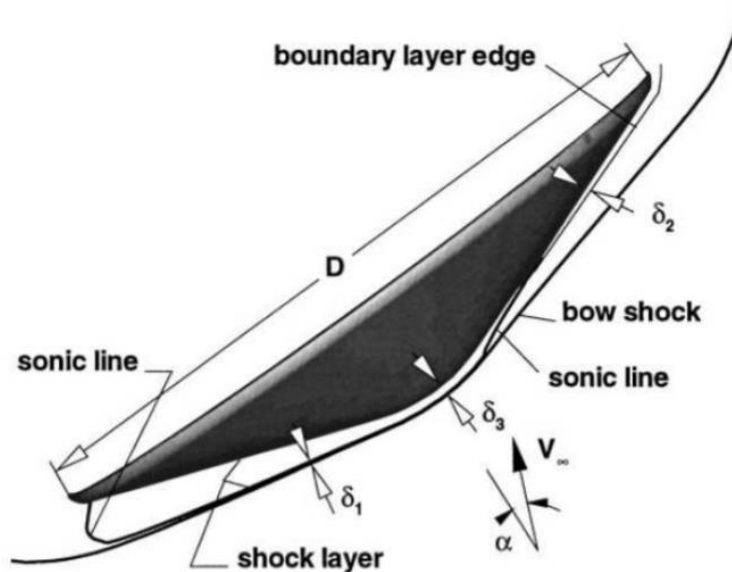


Figure 27 - Figure for an entry vehicle [15]

As a result of the shock wave, the entropy rises at the expense of a loss of the total pressure, depending on the bow shock shape and the free stream Mach number; the higher is the shock inclination, the higher is the total pressure loss and the entropy rise. The consequence of a loss of total pressure is the wave drag, which grows with the increase of the bow shock portion with large inclination.

The blunt body problem consists of the determination of the position and structure of the shock wave and consequently of the flow-field structure behind the shock. Fully understanding this flow field enables the calculation of important parameters for an entry vehicle as :

- Heat transfer distribution on the vehicle , with a particular interest in the stagnation point

- Structure of the entropy layer
- Surface pressure distribution
- Characteristics of the boundary layer.
- Shock/boundary layer interactions causing thermal and mechanical loads to the vehicle.

Some considerations about the boundary condition, solving hypothesis, and governing equation will be introduced to clarify the difficulty of the problem.

At the high Mach number of hypersonic, or supersonic entry, the Reynolds number, defined as $\frac{\rho LV}{\mu}$, enables the separation between viscous and inviscid portions. With the inviscid flow approximation is possible to determine the aerodynamic characteristics of a supersonic vehicle, while considering the viscous phenomena constrained in a small region around the body, the boundary layer. Thus, the assumptions regarding the boundary layer, such as velocity profile, temperature profile, and boundary layer interaction with the shock waves, won't be considered. With the inviscid hypothesis, the shock wave is treated as a discontinuity embedded in an inviscid flow field.

The criticality in this computation relies on the structure of the shock layer behind the shock wave. The shock layer is defined as a dynamic region within the shock wave and the body. In the case of a detached bow shock, this layer is shaped as a mixture of supersonic and subsonic flow-field divided by a sonic line. The overlapping of these two regimes prevent the application of classical analytic solutions and requires the application of numeric methods.

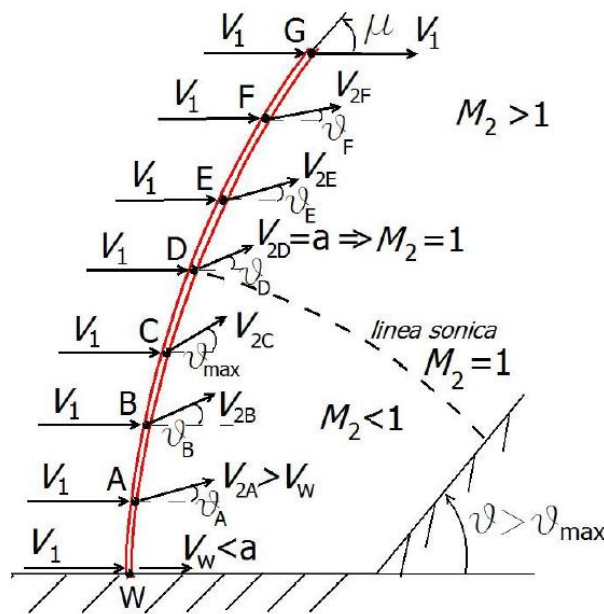


Figure 28 - Representation of a detached bow shock

The definition of a detached and curved shock is introduced in the framework of the oblique shock theory. The corner angle, θ , is the angle that defines the downstream flow direction with respect to the upstream direction and is related through the Beta-Teta-Mach relation to the upstream Mach number and the oblique shock angle. For a specified upstream Mach number, assuming a θ angle, is possible to extrapolate the oblique shock angle and through the relations of the oblique shock, the downstream flow main features, i.e. the downstream Mach number, total pressure, etc. When θ exceeds the maximum value predicted for a specified incoming Mach number, the oblique shock wave is no longer attached to the body and is replaced by a detached bow shock. Even if the above chart represents the situation existing for a

supersonic flow encountering a corner that turns the flow, the main features of the detached shock wave are in common with the bow shock enveloping an entry blunt body. The consideration related to this case are still valid for the bow-shock analysis regarding the blunt body, though the inferior wall is substituted by a symmetry plan for the blunt-body case, thus assuming a symmetric situation for a 2 D flow : an ideal case with flow incidence of 0° AoA.

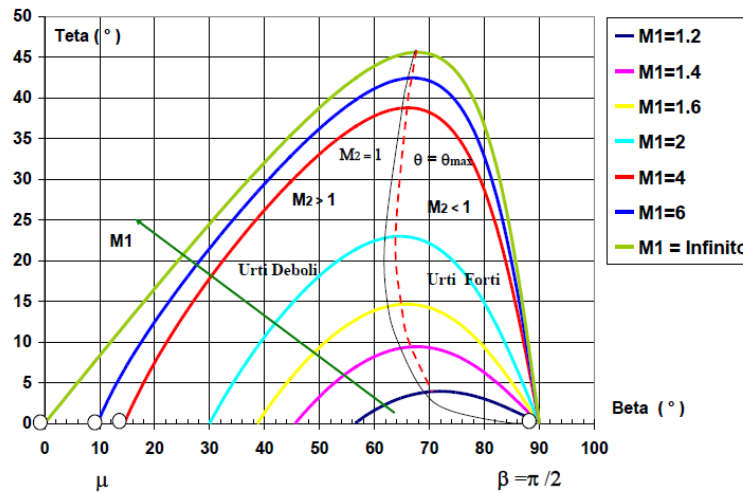


Figure 29 - θ - β -Mach curve

Exceeding the maximum inclination for a fixed Mach number prevents the application of the oblique shock theory to compute the flow-field characteristics beyond the shock: there's no matching between a horizontal line for a fixed Mach number competing to a $\theta > \theta_{max}$. However, immediately downstream the shock the field could be computed with the theory of oblique shock; besides this position, the streamlines follow a curved trend in order to be aligned with the wall direction, to respect the tangency condition, and thus the particles velocity increases indicating a dynamic expansion.

In the lowest point, defined as W, corresponding to the symmetry axis, or inferior wall, the shock has an inclination of 90° . There, the shock assumes the characteristics of a normal shock, with subsonic flow downstream. Moving away from the symmetry plane, the local shock inclination β , defined by the tangent of the shock itself, slightly decreases. On the contrary, the downstream flow deflection, θ , immediately downstream the bow shock, starts to increase till the maximum value. This situation could be compared to a motion on a fixed curve defined in the above chart : starting from the point at the bottom right and moving to the left direction, the β angle drops, the θ increase till the maximum value, and the resulted shock intensity decreases. Indeed, overcoming the maximum θ , corresponds to a continuous reduction of the shock intensity. From a certain distance from the symmetry plane, the shock is so weak to become a Mach wave with no changes in flow deflection ($\theta = 0^\circ$) and flow speed. In conclusion moving away from the symmetry plane, or inferior wall, causes the gradual weakening of the shock wave, until it vanishes, leading to undisturbed propagation of the upstream flow. Inside the shock layer is possible to underline a sonic line, that divides the subsonic inferior field to the supersonic superior field.

The post-shock conditions are computed by the Rankine-Hugoniot relations, obtained from the normal shock relations substituting the Mach number with the normal Mach number; thus, these shock conditions represent one of the boundary conditions for the governing equations of the whole flow-field behind the shock wave. Moreover, the other boundary condition is that the normal component of the velocity to the wall is always 0.

$$V \cdot \vec{n} = 0$$

While the boundary conditions are defined, the physical boundaries of the problem are not completely determined, as far as only the shape of the blunt body is known a priori: the bow shock and the position of the sonic line should be found, and represent the other physical boundaries of the problem.

Considering the previous assumption of inviscid flow, the steadiness of the phenomena and the subsonic-supersonic shock layer, the governing equations are the steady Euler equations, which appear mathematically elliptic in the subsonic region and hyperbolic in the supersonic region. The difficulty of the blunt body problem resides in solving elliptic and hyperbolic equations in the same flow-field. Thus, as later depicted, a time-dependent solution, able to solve the unsteady Euler equations, is considered the most viable approach for this kind of problem. As consequence, is better to consider the Euler's equations in the inviscid unsteady form:

$$\frac{\partial \rho}{\partial T} + \nabla(\rho \mathbf{v}) = 0 \quad \text{Mass balance equation}$$

$$\frac{\partial \rho u}{\partial T} + \frac{\partial (p + \rho u^2)}{\partial x} + \frac{\partial (\rho uv)}{\partial y} + \frac{\partial (\rho uw)}{\partial z} = 0 \quad \text{Momentum balance x-direction}$$

$$\frac{\partial \rho v}{\partial T} + \frac{\partial (\rho vu)}{\partial x} + \frac{\partial (p + \rho v^2)}{\partial y} + \frac{\partial (\rho vw)}{\partial z} = 0 \quad \text{Momentum balance y-direction}$$

$$\frac{\partial \rho w}{\partial T} + \frac{\partial (\rho wu)}{\partial x} + \frac{\partial (\rho wv)}{\partial y} + \frac{\partial (p + \rho w^2)}{\partial z} = 0 \quad \text{Momentum balance z-direction}$$

$$\frac{\partial E}{\partial T} + \frac{\partial [u(E+p)]}{\partial x} + \frac{\partial [v(E+p)]}{\partial y} + \frac{\partial [w(E+p)]}{\partial z} = 0 \quad \text{Energy balance equation}$$

Where :

- p is the pressure;
- ρ the mass ratio per volume unit;
- u, v, w , the speed component
- $E = C_v \rho T + \rho(u^2 + v^2 + w^2)$, which is the total energy per volume unit

Analytical methods are inadequate to predict the detail of a flow field near the blunt nose for the supersonic blunt body problem.

The first, complete, practical blunt body solutions were elaborated through three different reports, by Moretti, Abbett and Bleich [16]: in their dissertations the blunt body problem was solved through a time-dependent method, used at first in two-dimensional problems, and then enlarged to the axisymmetric computation.

The time-dependent blunt body approach leads to the solution of the unsteady Euler's equation, partial differential equations, that describe the transient flow field characterizing the blunt body problem. The first step for elaborating the solution is defining the region of the analysis: this region is bounded by the shock, body surface, the plane of symmetry, and an upper boundary involved in the supersonic region, to avoid the return of any disturbance to the upstream direction. Also, this region of interest is divided into three different parts: the shock itself, the body surface, and the inner points. Once again, this area is divided into square elements to constitute the calculation domain for the difference finite element method.

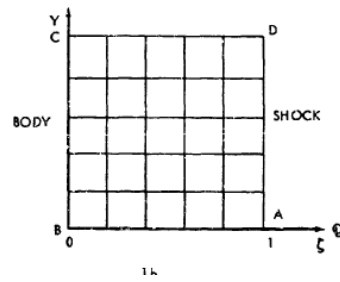
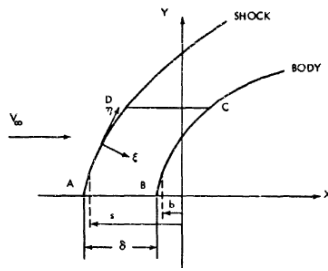


Figure 30 - Region of interest for the calculation [16]

Once the calculation region is determined, the solution starts by assuming arbitrary initial values for the flow field variables, shock wave, and shock location. Indeed, the free stream conditions and the body shape are assigned and fixed. In this theory, the detached bow shock can be incorporated within the flow being analysed. Then the solution is structured upon by a finite difference scheme used for discretizing the unsteady equations, and obtaining new values of the variables, shock wave shape and location in steps of time. The solution following a relaxation process converges to a steady state, indicating, as predicted by the steadiness hypothesis, that the use of the time-dependent equations is just useful to avoid the solution of steady flow equations that, as depicted before, are elliptic in the subsonic region and hyperbolic in the supersonic regime. The unsteady Euler's equations are hyperbolic in time, and for this reason, they allow the use of a finite difference approach, with starting arbitrary condition at a given initial time. The converged solution flow values are assigned at each mesh point, or computational cell, and considering the whole calculation domain is possible to build the global solution of the blunt body problem. [17]

The use of this method brought to the resolution of the blunt body problem for several Mach upstream numbers, Ma , different blunt bodies (i.e. parabolic cylinder, cubic cylinder, sphere cone, blunted wedge), and leads to the definition of :

- Body pressure distribution;
- Mach number distribution on the body;
- Shock shape and shock position definition;
- Sonic line position;
- Stagnation point position and stagnation point pressure.

Besides these outcomes, the solution raises the knowledge of the physical phenomena characterizing the blunt body flow field. For instance, the pressure waves originate behind the initially unsteady bow shock, propagating and interacting downstream, appeared to be the physical mechanism able to stabilize the unsteadiness and brought to converge to a steady state the flow field. A higher Mach number showed the capability to accelerate the convergence and reduce the bow shock distance and the downward shift of the sonic line. Moreover, passing from the 2 D situation to the axisymmetric 3D problem, leads to a closer approach of the shock to the body and to thin up the shock layer, due to the higher flow rate disposed of a tri-dimensional situation.

Additionally, the results showed agreement with Bilig empirical correlations for bow shock shape and location [17]. These correlations are simple engineering relations based on experimental data, useful for finding the bow shock standoff distance, defined as the distance between the stagnation point on the body and the closest point on the shock front. With the assumption of hyperbolic shock shape, either for sphere cone blunt body or cylinder-wedge, is possible to define the standoff distance as a function of the incoming Mach number :

$$\frac{\Delta}{R} = 0.143 \exp\left(\frac{3.24}{M_\infty^2}\right) \text{ sphere cone}$$

$$\frac{\Delta}{R} = 0.386 \exp\left(\frac{4.67}{M_\infty^2}\right) \text{ cylinder wedge}$$

Where:

- R and is the radius of the nose
- Δ is the standoff distance.

The time-dependent solution was considered the most valuable numerical method for the blunt body problem. As a direct and exact numerical method with the body shape and free stream properties given, can solve large portions of the supersonic flow field, upstream and downstream the sonic line, and also doesn't involve any simplification or reduction in the governing equations. The validation of the Moretti and Abbett's numerical method laid the foundation for the numerical computation resolutions methods, implemented nowadays in CFD program, which can easily compute and solve the blunt body problem and overcome some limitations of the time dependent method (i.e. application to body shapes with a local discontinuity in surface curvature, or the enlargement of arbitrarily initial conditions).

Typical CFD modern methods are based on finite volumes discretization of the unsteady Euler's governing equations. Such equations are solved numerically in a physical domain based on that one predicted by Moretti, which is then divided into computational cells. For the inviscid computation, the boundary condition used to solve the equations are:

- The velocity component normal to the wall equal to 0;
- The Supersonic outflow boundary condition;
- The symmetric boundary conditions if AoA is equal to 0 and the body has a symmetrical geometry.

While the subsonic pocket is completely inside the physical domain, there are two different approaches employed to define the inflow boundary:

- Shock capturing technique : which doesn't consider the bow shock wave as the outer boundary and leads to the automatic computation of the shock within the solution of the flow field.
- Shock fitting technique, which considers the shock as a discontinuity which constitutes the outer moving boundary.

Either shock capturing or shock fitting are considered as valuable techniques to compute this kind of flows, but shock capture, which is affected by the problems related to the computation of a discontinuity in a finite number of grid points, provides a more robust approach in practical applications, where the shock may interact with other discontinuities.

3.2 Underexpanded and highly underexpanded jet flow

During an engine ignition while crossing the atmosphere, it is difficult to match the atmospheric pressure for the jet exhausting a convergent-divergent nozzle. The aerodynamic flow field related to the exhausting jet is strongly dependent on the ratio among the jet exit pressure and the local ambient pressure. In the majority of the physical situation, due to high working pressure of the engine, the jet exit pressure is greater than the ambient pressure, leading to the situation of under or highly underexpanded jet flow: the jet should continue outside the expansion started within the divergent part of the nozzle to match the atmospheric pressure

Considering an exit jet pressure 1-2 times greater than the ambient local pressure, the flow field derived is characterized by an underexpanded situation. In order to complete the expansion and lead to the adaptation condition, at the nozzle lip the jet undergoes to Prandtl Meyer expansion waves. These waves strongly reduce the jet pressure through subsequent expansion until achieving a pressure value lower than the ambient local pressure. Hence, due to this pressure reduction, the expansion waves propagate downstream and reflect off to the ambient boundary as a compression wave. The ambient boundary, namely the jet boundary, is a mixing region resulting from the viscous interaction of the supersonic jet with the surrounding quiescent medium. The compression waves coalesce forming an oblique shock aimed to increase the jet pressure. As a result the pressure increases again to values larger than the ambient pressure and the process starts again. The structure, namely the diamond shock pattern, repeats consecutively downstream until viscous and turbulent mixing phenomena within the jet flow and the ambient dissipate the plume configuration.

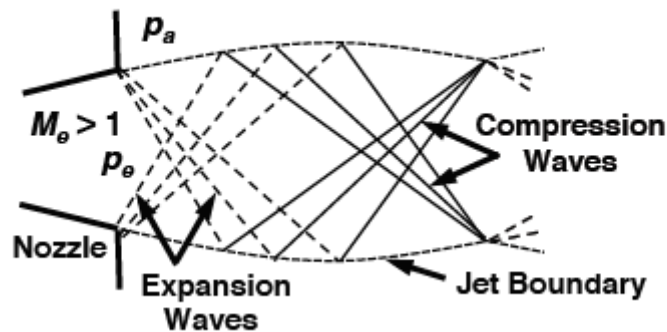


Figure 31 - Jet underexpanded configuration [18]

If the jet exit pressure among local ambient pressure ratio exceeds the value of 3-4, the flow field varies from the underexpanded condition to a highly underexpanded mode, indicating that engines are running with a high underexpanded situation. The flowfield presents a similar trend to the underexpanded situation near the nozzle exit. Indeed at the nozzle lip, the flow is subjected to an expansion fan, the Prandtl Meyer expansion waves, aimed to lower the pressure.

The expansion waves propagate downstream toward the jet boundary. Likewise the previous case, the jet boundary is a mixing region resulting from the viscous interaction of the supersonic jet with the surrounding medium: the pressure interaction at the boundary tends it back toward the centreline, while a high-velocity shear layer embeds it.

After the expansion waves, the jet pressure returns to a level lower than the ambient pressure, and a mechanism similar to the under expanded situation occurs. Indeed, the expansion waves reflect off the boundary jet as compression waves which coalesce into a barrel shock structure. This barrel shock constitutes a boundary shock wave, which separates the expanding plume from the ambient flow, and propagates downstream, bending to the jet centreline as a consequence of pressure interactions. Despite the regular reflection and intersection of the oblique shock waves for slightly underexpanded jet, either on the jet boundary and the axis of symmetry, the barrel shock irregular reflection induces the formations of a lens-shaped normal shock, namely the Mach disk or Riemann wave, upon which the flow field passes from supersonic to subsonic conditions. the presence of the normal shock induces a sonic throat like region, and at the intersection of the barrel shock and Mach disk, an oblique reflected shock occurs. So, the flow particles which remain inside the jet flow field could follow two different paths:

- Expanding through the jet core region and undergoing a normal shock through the passage upon the Mach disk, resulting in subsonic conditions downstream the shock.
- Expanding through the jet core region and passing through the oblique reflected shock wave, resulting in supersonic conditions downstream the oblique shock.

The interaction of these two possible motion regimes induces the creation of a slip line, originate at the triple point, where the Mach disk, the oblique shock and barrel shock interact, which separates the subsonic condition from the supersonic condition and upon which the flow pressure and direction coincides for both supersonic and subsonic particles : this leads to the creation of a subsonic inner shear layer.

Behind the Mach disk, the flow accelerates to supersonic speed, inducing the reduction of jet pressure and leading to the repetition of the depicted structure. While propagating downstream, as a result of the viscous interaction and turbulent mixing whit the ambient, the Mach disk gradually disappear after a number of cycles depending on the pressure ratio, meanwhile the flow field undergoes additional weak expansion and compression waves.

Is also remarkable the presence of the boundary layer which envelopes the nozzle exit wall : the subsonic part of the boundary layer leads to reversal exhaust flow to the baseplate, inducing heat transfer issues on the vehicle base and propulsion elements. [19] [20] [21] [22].

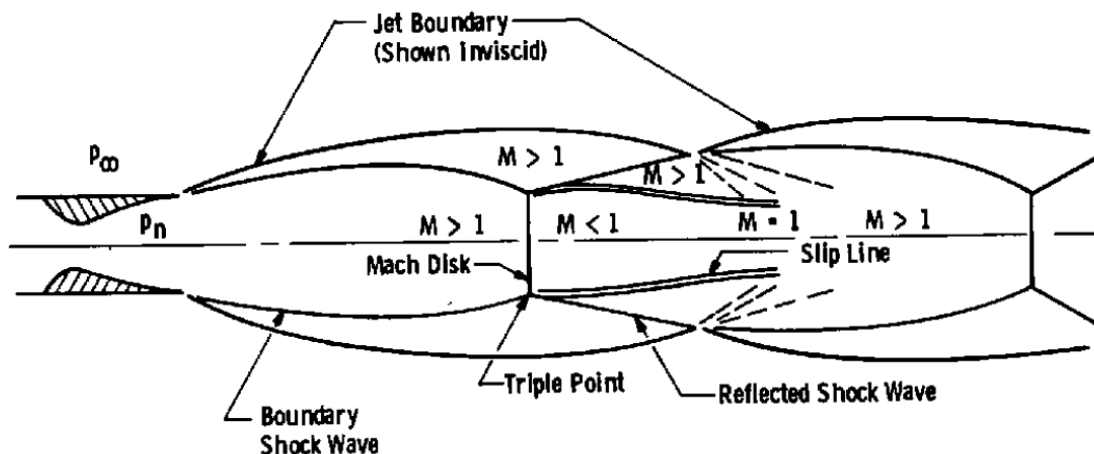


Figure 32 – Underexpanded jet structure [23]

To obtain a fuller understanding of under expanded and highly under expanded supersonic jet, either for the aerodynamic and thermodynamic behave, several investigations through analytical studies, CFD methods, laboratory experiment, and empiric simulations have been conducted through the years.

3.3 Supersonic retropropulsion flowfield

The configuration (location, number, and size) of the nozzle determines the structure and behavior of the flowfield. In the dissertation will be simulated a central nozzle configuration, with incoming freestream flow inclined of 0° AoA, and therefore the described flowfield is related to such condition.

The supersonic retropropulsion is characterized by the interaction between a supersonic jet flow, in high under expanded condition, counteracting a supersonic freestream. The interaction behavior is dictated by the value of the ratio among the total pressure of the exhausting jet and ambient pressure; as for the description of a jet exhausting into a quiescent medium, this ratio determines the intensity of the expanding jet, which influences the interaction with the freestream. The aerodynamic resulting flowfield is a complex structure due to the penetration of the shock layer by the exhausting jet.

The flow primary features that distinguishes the SRP flowfield are :

- Bow shock ;
- Free stagnation point;
- Mach disk ;
- Recirculation regions;
- Shear layers;
- Jet plume;
- Triple point.

At first, the jet plume constitutes an obstruction to the supersonic incoming freestream, hence a bow detached shock is generated. In the framework of a Mars descent phase, the jet's plume is not the primary cause of the bow shock creation: indeed, as previously depicted, is the blunt body shape that determines the detached shock.

The interaction of these two aerodynamic flowfields determine unique physical regions that characterize the SRP flowfield.

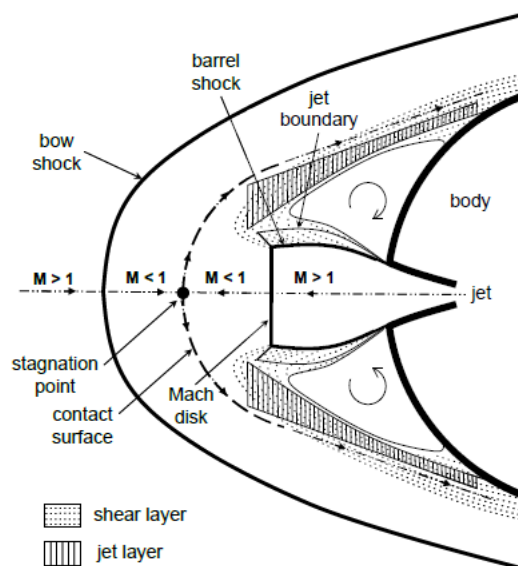


Figure 33 - SRP flowfield [24]

In the left part of the chart, along the symmetry axis, is remarkable the subsonic stagnation region originated by the interaction of two subsonic areas. The supersonic freestream is decelerated through subsonic speed behind the bow shock while the highly under expanded situation leads to the jet expansion through the jet cores and afterward, a strong deceleration related to the presence of the Mach disk occurs, leading to subsonic condition also the jet exhausting flow. Combining these two situations induces the creation of a contact surface: the two subsonic listed flows, continue to decelerate until the achievement of a stagnation condition, get in the stagnation point, which is situated along this surface and also separates the two regions.

The exhaust jet structure reminds to that one depicted without a counteracting flow: indeed, while at the nozzle exit the flow is subjected to Prandtl Meyer expansion waves, a barrel shock impinges the jet core and terminates with the Mach disk's shock structure. The jet core is clearly bounded by the boundary jet which divides the supersonic jet flow from the outer region behind the bow shock. Like the high under expanded situation, a shear layer surrounds the jet boundary and represents a remarkable mixing region responsible for the diffusion of the jet away from the nozzle and the mixing within the flow surrounding the jet core. Large recirculation regions are created by the interaction of the shear layer and the freestream flow moving backward to the aft body, that are affected to the low pressure zone near the nozzle exit. The recirculation regions and the high pressure condition behind the bow shock, induces strong mixing phenomena.

With the central nozzle configuration the contact surface previously depicted represent the effective obstruction seen by the freestream, which then substitutes the obstruction created by the blunt body case without the exhausting jet. The obstruction in the propulsive case is larger than the blunt body situation with no propulsion. The increased stand-off distance and the perturbations induced by the shock, that weaken the bow shock, leads to a reduction of the surface pressure on the forebody compared with the no-propulsive case. Either the pressure reduction and the shock weakness are enhanced with the increase of the freestream Mach. As a result, an annular region of constant pressure surrounds the forebody and allows maintaining quite laminar flow within the shock layer. The pressure reduction on the forebody explains the reduction in the aerodynamic drag for the SRP compared to the blunt body configuration. The thrust coefficient is also related to the constant pressure enveloping the entire body. After the separation of the boundary layer occurring at low C_t values, the flow heading to the vehicle's shoulders reattach at C_t near 2, and a further increase in C_t contributes to the formation of the constant pressure region that characterized the SRP configurations.

To explain the relation between the thrust coefficient and the aerodynamic drag reduction, the thrust coefficient is plotted as a function of the total axial force, defined as the sum of the C_t (thrust coefficient) and the Drag coefficient (C_d).

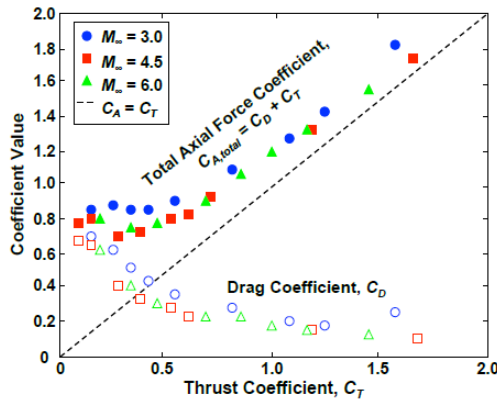


Figure 34 - Variation of axial coefficient and drag coefficient related to thrust coefficient with a central nozzle [25]

The above chart demonstrates how increasing the thrust coefficient at first rapidly reduces the drag coefficient up to 5-10% of the reference value for a non-propulsive case and then induces a constant trend of C_d despite further augmentation. Above 0.5, C_t is the prevalent term for the axial force, which grows proportionally with the coefficient increase. In conclusion, the axial coefficient for the propulsive case outperforms the non propulsive condition. To complete the aerodynamic overview is also important to underline that even in an unstable or unsteady situation, the pitching moment slope is negative, and therefore the entry body is considered statically stable [26] .

The increase in C_t , and therefore in thrust , leads to a drag reduction , implicating that all the deceleration shall be furnished by the propulsive system .

Moreover, increasing the thrust coefficients results in increasing the Mach disk dimension, enhancing the interaction strength between the freestream and jet flow, and so augmenting the subsonic wake region in the aft body, and the effective obstruction surface saw by the freestream. Indeed in the SRP framework, the importance of C_t is related to its direct relations with the pressure ratio: the exhausting jet conditions are described by this parameter, which substitutes the pressure ratio when the freestream conditions are fixed.

The variation of C_T induces important consequence on the flow field stability, that differs from flowfield steadiness. The flowfield stability in the supersonic retropropulsion studies, refers to the transition from two different configurations related to the penetration of the bow shock by the exhausting jet : a blunt penetration mode (BPM) and a long penetration mode (LPM).

The main parameters that distinguish these two modes are the ratio among the total jet pressure and the total ambient pressure and the mass flow rate of the exhausting jet.

Starting from low values of the pressure ratio, a first BPM occurs : the viscosity dissipates the jet power reducing the jet speed to levels comparable to those of the flow downstream the bow shock; in this situation the jet isn't strong enough to penetrate the bow shock because the total pressure doesn't allow a remarkable expansion downstream the nozzle exit. This blunt penetration first mode difficulty appears in the interesting studies case: the low-pressure ratio may occur just during the engine ignition and may survive for a relative neglectable time, associated with a transient event.

Increasing the pressure ratio induces the strengthening of the jet power, which is, therefore, able to penetrate the bow shock and to induce an unstable configuration, namely LPM. In this condition. The standoff distance increases proportionally to the incoming mass flow rate of the jet, reaching a maximum

displacement of 8-9 body diameters. The upstream displacement of the bow shock and the strong interaction between these two phenomena leads to the augmentation of the unsteadiness of the flowfield. The long penetration mode corresponds to a moderately underexpanded jet mode.

However, the unstable regime could be considered as a transient event that characterizes the engine ignition during a descent or ascent phase. As previously depicted the working pressure of the engine causes a pressure ratio much larger than 2-3, hence inducing the highly underexpanded situation for the exhausting jet. In this regime, that characterizes many cases of interest and simulations, the penetration mode returns to a stable condition while reducing the stand-off distance.

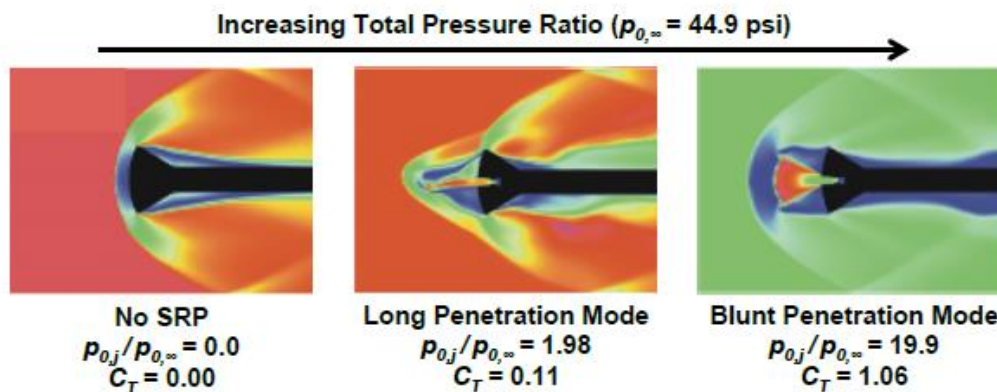


Figure 35 - Transition between long and blunt penetration mode [25]

The transition from LPM to a stable BLM reduces the unsteadiness level of the flowfield, but it still presents unsteady events. The unsteadiness of the stable configuration is heavily related to the behavior of the triple point. The disturbances generated in this point, propagate through the large subsonic recirculation regions, the velocity shear layer, the stagnation subsonic region and also downstream towards the aft body.

The triple point presence strongly characterizes the flowfield of the supersonic retropropulsion; this interesting point is located at the intersection of the Mach disk, the shear layer, and the subsonic region behind the bow shock. In correspondence of this point, the jet flow turns back in order to be aligned with the oncoming supersonic flow and to undergo the mixing phenomena characterizing the shear layer. Its presence is defined either in Mach isocontours scenes and in the streamlines paths. Moreover, the streamlines indicate the location of the contact surface and the free stagnation point.

The unsteadiness is related to the triple point oscillations, which generate pressure waves that propagate through the shear layers and recirculation regions. These waves, also defined as vortex shedding, reflect off the model face and off the barrel plume shear layers, generating the self-excitation of the oscillations. The frequency of the triple point oscillation is the predominant frequency of the unsteady events, hence its value has been taken as a reference data to compare the quality of CFD simulations. [18]

Even if the mixing layer leads to a laminar configuration, turbulence models approach may constitute a significant improvement in capturing the viscous dissipation phenomena dominating the shear layers. To date, is still unclear when the transition from laminar to turbulent state occurs, however appropriate turbulent modelling may lead to enhance ability of capture flow structures and thus to obtain better output values. Moreover, even is not well quantified how viscosity could decrease the degree of the unsteadiness, is evident, from CFD and laboratory simulations, that viscous dissipation reduces the

unsteady phenomena, embodying a damping effect for the unsteadiness, and therefore considering a turbulent dissipation mode may lead to quantify this unsteady reductions. [22]

However, given the nature of the dissipative phenomena, a viscous approach is strongly preferred to the inviscid approximation, as far as could lead to precisely defining the jet structure and interactions regions.

In conclusion, the recirculation regions near the body and the mixing layer induce an augmentation of the wake aft of the body compared to a non-propulsive configuration. However, this wake region is regulated by different parameters and varies with the freestream conditions, nozzle area, total jet pressure, and nozzle configurations.

Due to the viscous nature of the flowfield, considering the high Mach number involved, and the unsteady phenomena the governing equations are the Navier Stokes equations. These equations enable the complete description of a fluid motion basing on the following three physical principles :

- Conservation of mass, which determines the mass balance equation
- Conservation of momentum, which determines the momentum balance equation
- Conservation of energy, which determines the energy balance equation.

To model a fluid flow with the Navier Stokes equations is important to asses some crucial hypotheses that restrict the applicability of the equations :

- The fluid shall be a continuum, achieving a Knudsen number equal or lower than 0.01.
- The fluid shall be in thermodynamic equilibrium, with no chemical reaction occurring and the equation of state shall describe the relation between temperature , density, and pressure.



Navier–Stokes Equations

3 – dimensional – unsteady



Coordinates: (x,y,z)	Time : t Pressure: p	Heat Flux: q
Velocity Components: (u,v,w)	Density: ρ Stress: τ	Reynolds Number: Re
	Total Energy: Et	Prandtl Number: Pr

Continuity: $\frac{\partial \rho}{\partial t} + \frac{\partial(\rho u)}{\partial x} + \frac{\partial(\rho v)}{\partial y} + \frac{\partial(\rho w)}{\partial z} = 0$

X – Momentum: $\frac{\partial(\rho u)}{\partial t} + \frac{\partial(\rho u^2)}{\partial x} + \frac{\partial(\rho uv)}{\partial y} + \frac{\partial(\rho uw)}{\partial z} = -\frac{\partial p}{\partial x} + \frac{1}{Re_r} \left[\frac{\partial \tau_{xx}}{\partial x} + \frac{\partial \tau_{xy}}{\partial y} + \frac{\partial \tau_{xz}}{\partial z} \right]$

Y – Momentum: $\frac{\partial(\rho v)}{\partial t} + \frac{\partial(\rho uv)}{\partial x} + \frac{\partial(\rho v^2)}{\partial y} + \frac{\partial(\rho vw)}{\partial z} = -\frac{\partial p}{\partial y} + \frac{1}{Re_r} \left[\frac{\partial \tau_{xy}}{\partial x} + \frac{\partial \tau_{yy}}{\partial y} + \frac{\partial \tau_{yz}}{\partial z} \right]$

Z – Momentum: $\frac{\partial(\rho w)}{\partial t} + \frac{\partial(\rho uw)}{\partial x} + \frac{\partial(\rho vw)}{\partial y} + \frac{\partial(\rho w^2)}{\partial z} = -\frac{\partial p}{\partial z} + \frac{1}{Re_r} \left[\frac{\partial \tau_{xz}}{\partial x} + \frac{\partial \tau_{yz}}{\partial y} + \frac{\partial \tau_{zz}}{\partial z} \right]$

Energy:

$$\frac{\partial(E_T)}{\partial t} + \frac{\partial(uE_T)}{\partial x} + \frac{\partial(vE_T)}{\partial y} + \frac{\partial(wE_T)}{\partial z} = -\frac{\partial(up)}{\partial x} - \frac{\partial(vp)}{\partial y} - \frac{\partial(wp)}{\partial z} - \frac{1}{Re_r Pr_r} \left[\frac{\partial q_x}{\partial x} + \frac{\partial q_y}{\partial y} + \frac{\partial q_z}{\partial z} \right]$$

$$+ \frac{1}{Re_r} \left[\frac{\partial}{\partial x} (u \tau_{xx} + v \tau_{xy} + w \tau_{xz}) + \frac{\partial}{\partial y} (u \tau_{xy} + v \tau_{yy} + w \tau_{yz}) + \frac{\partial}{\partial z} (u \tau_{xz} + v \tau_{yz} + w \tau_{zz}) \right]$$

Figure 36-Navier Stokes equations

Chapter 4

4.1 Introduction to CFD and test reference case

To date, the Technology Readiness Level set for SRP for human Mars exploration purpose is being elevated to 3. Referring to the NASA definition about TRL level, the technology concept and eventual application are formulated. So physical principles are observed and described and an application may be defined, and active studies are ongoing in order to determine with analytical test and laboratory-based studies the proof-of concept of the concept/applications previously validated. [27]

The achievement of the TRL 1 has been obtained through technologic tests developed in 60s-70s. The importance of these tests and studies was identifying the main fluid dynamic features and aerodynamic trends. Also in these years were introduced, in the framework of SRP, the scaling parameters able to simulate the chemical propulsion system using subscale models. A precise description of the definition of the scaling parameters, i.e. Mach number, thrust coefficient, and pressure sensitivity, is presented in the reference. [28]

Computational simulations will support the extension of the TRL level to elevate the technology from a feasibility state to a useful-proof viable means.

The key-point of applying CFD in fluid dynamic problems is related to the wide range of conditions and situations that can be implemented and studied through the computation. Setting different assumptions as initial conditions could lead to capture only targeted phenomena, as well as flow properties or some flowfield regions.

CFD past simulations enabled to better understand the uncertain phenomena predicted in SRP flowfield through wind tunnel test experiments, as the plume-vehicle interaction, flowfield unsteadiness, and jet-bow shock interaction.

In addition to the depicted purposes, CFD results are nowadays also needed to determine constraints on TPS and propulsion control and for constructing a viable aerodynamic vehicle database upon which the entry trajectory simulations will be implemented.

Indeed the coupled application of CFD validating methods and ground test data in terms of aerodynamic and aeroheating is considered a milestone during each technology validation steps. The complete process and technology area of improvement in order to bring the SRP to a 6 TRL level is summarized in reference [27].

In the framework of SRP is important that a CFD simulation can capture :

- Flow main features as shock Mack disk, bow shock, recirculation regions, presence of the triple point, jet flow boundary, presence of the stagnation point;
- Shock layer viscous interactions;
- Unsteady phenomena related to the oscillatory behavior of the triple point even in stable flow fields;
- Relevant equilibrium thermodynamic situation.

To support technology level elevations, considerable efforts have so been made in order to validate CFD methods, enhance confidence in CFD prediction and pay the ground for the CFD utilization as a backbone during the whole TRL augmentation process.

The validation of the CFD methods occurs with a comparison of certain computed quantities against the acquired experimental data; the validation of CFD codes occurs through laboratory experiments based on

scaling methods able to full scale the involved flow-field and engine elements and simulate the flow structure with cold gas jets. The validity of the scale approach is enabled by the normalization of the governing equation.

Indeed the achievement of TRL 3, regarding the aerodynamic technological area of SRP, is strongly based on accomplishing ground tunnel tests only designed to validate CFD method, which clearly represents an easy method than reproducing Mars's relevant condition for ground test facilities. Moreover, all the recent ground tests simulations have been approached just as CFD validation efforts.

Two wind tunnel tests of supersonic retropropulsion were completed by Nasa's ETD-TDP program one in July 2010 in the NASA LARC 4x4 ft UPWT and the second in August 2011 in the ARC 9 x 7ft UPWT. These were the first tests targeting conditions approaching flight relevance for high mass Mars exploration mission and dedicated to producing a data set for the validation of CFD tools. [29] These two tests constituted the baseline for CFD validations of 3 different Navier Stokes codes, DPLR, OVERFLOW, FUN3D. Even the difference presented each code reproduced the general shape of the SRP flowfield, captured the unsteadiness of the triple point, and showed good qualitative and quantitative agreements with the test results.

The optimum quality of the results obtained both from the comparison and from the tunnel tests, together with the wide range of tested configurations lead to define as reference case the data obtained from these two tests, and, particular aligned with the dissertation purpose, with a test case obtained in the LARC 4x4 UPWT, which will be soon introduced.

The model was a slender body with a 5 inches diameter 70° sphere cone forebody and cylindrical aft body of 10 inches. High pressure air was used for simulating the incoming freestream and the exhausting jet. The model was equipped with static pressure ports and high frequency pressure transducers in order to gather and compute data about surface pressure on the model. The whole model structure, its relevant geometric features, the whole test settings, the uncertainty calculations and whole tests conditions are reported in reference [30].

The configurations tested differ in terms of :

- Number of nozzle tested : 0-1-3-4;
- Freestream Mach condition : 1.8, 2.4, 3.5, 4.6 .
- Thrust coefficient up to 6.0
- Roll angle 0-180°
- Angle of attack sweeping from -8° to 20°

As previously depicted the dissertation purpose is at first to validate a CFD simulation able to reproduce the main features of SRP flowfield and then to verify against this validated simulation, a no-nozzle simplified situation where the starting conditions for the exhausting jet are set at the nozzle exit instead of the reservoir.

Hence, as depicted in ref. [31], the experimental run chosen for comparison is the run 165, because "represents the simplest jet case available that has a quasi-periodic flowfield structure, and the 0° AoA case has a largely axisymmetric behavior with a periodic unsteady frequency of 2 kHz". Also increasing the Mach test number decrease the wall-flow interface, as far as boundary layers are not neglectable for such a test section

Thus, the freestream condition, jet exhausting condition, and qualitative/ quantitative results for the 165 run will be reported. The initial conditions will serve to align the initial conditions of the simulation, and results will serve to compare the quality of the simulation, and therefore validating the CFD code.

Table 4-Freestream conditions run 165

Mach number	Static pressure	Static temperature	Reynolds Number	Angle of Attack	Roll angle	Nozzle configuration
4.6	536.65 Pa	65 K	1.5*10e6	0°	180°	1 central nozzle

From the listed values is possible to obtain all the flow derived conditions, i.e. density, total temperature, total pressure, dynamic pressure.

Table 5-Exhausting Jet conditions

Total pressure	Total temperature	Nozzle exit area/ throat area ratio	Thrust coefficient	Mass flow rate	Total temperature/ static freestream temperature	Total pressure/static freestream pressure
4137363.6 Pa	347. 1 K	4:1	1.97	0.62 lbm/s	5.34	7724

Moreover, the nozzle exit area ratio coupled with total temperature and total pressure furnish the other flowfield parameters as the exit Mach number, which computation will be later illustrated.

The thrust coefficient is computed considering the following relations

$$C'_T = \frac{T}{q_\infty A_{ref}}$$

Where the reference area is the projected surface area , 19.625 in².

The following results for the run 165 are presented to constitute a solid baseline aimed to validate the simulation results implemented in the dissertation. In order to furnish viable sets of comparable results, also some data obtained with the validated Navier Stokes codes, FUN 3D DPLR, OVERFLOW are reported, allowing a code-to-code comparison.

The results are split into qualitative outcomes and quantitative ones.

The qualitative results are high speed shadowgraph images and static frames aimed to compare the main features and structures of SRP flowfield. Through the streamlines and isocountors surface is possible to visualize the critical flow features.

On the contrary, quantitative analyses are realized through comparison of surface average pressure data either on the forebody and aftbody, both for the tunnel experiments and for the CFD simulation. No integrated force coefficients are given in tunnel test data , as the coefficients given in the experimental

data set were originally integrated from a very limited number of surface pressure and no information regarding the uncertainty in these measurements is given in the test report [30]

High-pressure transducers positioned on the forebody also provide additional dynamic data regarding the unsteady dynamic frequencies, that could also be computed with CFD codes.

In conclusion, Schlieren data were used to extract the dimensions of relevant flow features for the central nozzle case.

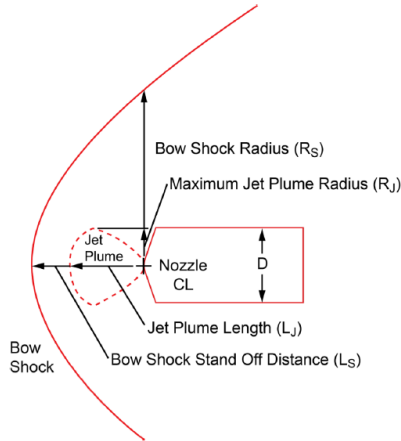


Figure 37-Relevant flow dimension computed for run 165 ref. [30]

The Schlieren images, pseudo Schlieren images, and Mach isocontours scenes allow the representation of all the SRP flow features. For instance is possible to visualize the Mach disk , jet boundary, triple point, bow shock standoff distance and subsonic regions(i.e. stagnation and recirculation) . As predicted the flowfield is globally steady except for the presence of the triple point oscillation, which determines the unsteady shedding vortex phenomena. Indeed, even if with a single image frame is quite impossible to evidence the unsteadiness, sampling image frames with time steps greater than the fundamental unsteady frequency allows a visualization of the unsteady vortex shedding propagating from the triple point.

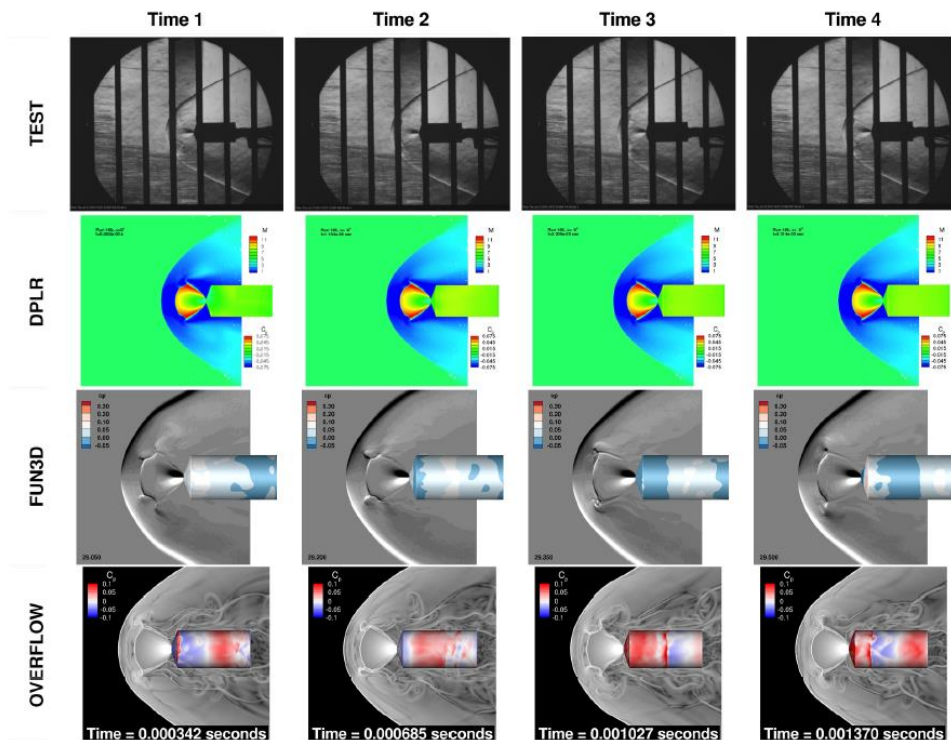


Figure 38-Schlieren, pseudo Schlieren and Mach isocontours scenes, from reference [29]

The surface averaged pressure coefficient computed as a function of the ray from the centerline to the shoulder, for the forebody, and of the ratio of longitudinal dimension to total length for the aftbody, reveals a severe reduction in surface pressure, compare to the no nozzle case; this pressure reduction is aligned with theoretical prediction previously described. Moreover, the flat pressure profile indicates a flow separation zone due to the recirculation in the subsonic mixing region. Indeed, the whole situation in terms of pressure coefficient indicates a quite constant pressure profile, strictly derived from the physical condition depicted before.

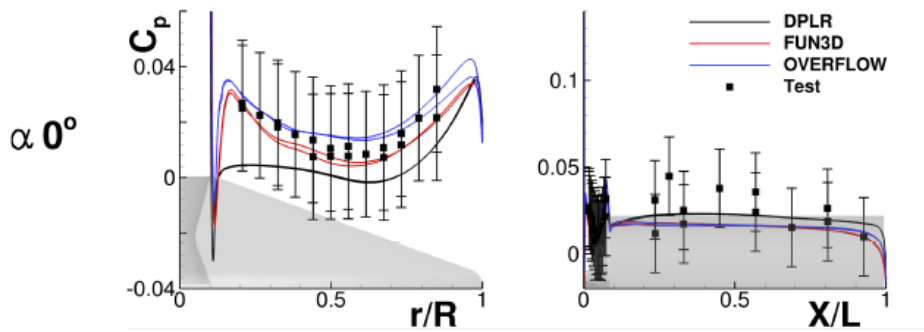


Figure 39-Forebody and Aftbody averaged surface pressure coefficient distribution [29]

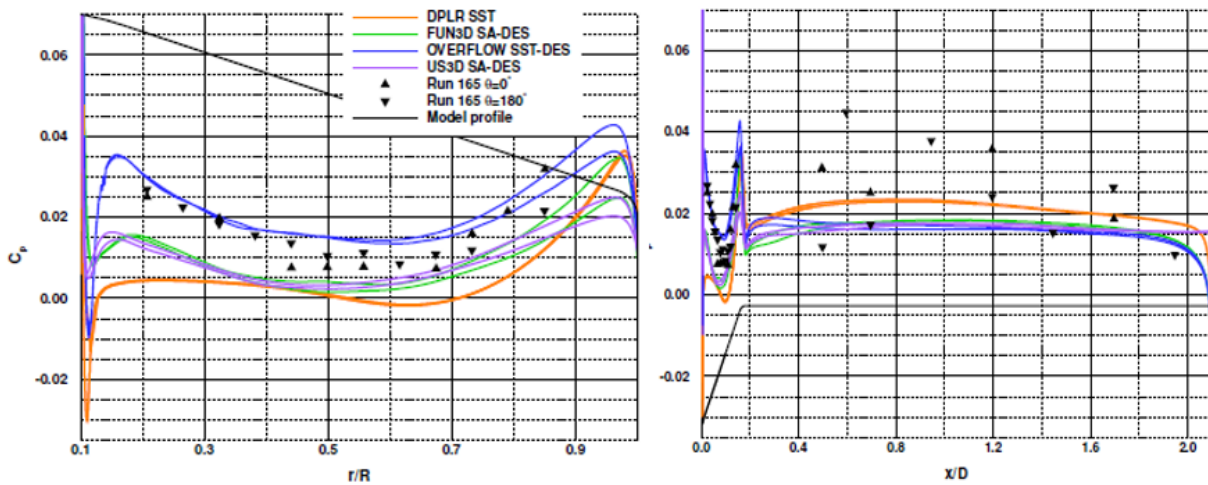


Figure 40-Forebody and aftbody averaged SA-DES surface pressure coefficient distribution from reference [31]

Despite the low C_p levels, is remarkable the increase in the pressure coefficient near the nozzle exit, related to the ability of most CFD codes to capture the unsteady pressure wave reflecting off the body as consequence of the vortex originate in the triple point propagating into the flowfield.

Flow features dimension are also reported because are an important and easy options to extrapolate a comparison between different simulations results. [29]

	Bow shock standoff distance	Bow shock radius	Jet plume length	Maximum jet plume radius
--	--------------------------------	------------------	------------------	-----------------------------

Flow features dimension in cm	18.33	24.56	12.92	7.82
--------------------------------------	--------------	--------------	--------------	-------------

The most part of resulted flowfield is quite steady, apart from the annular triple point region whose oscillation causes the vortex unsteady shedding in the flowfield regions. Different dissertations and studies approach the unsteady behave of this single test case [32] [33] [31], and a brief introduction to the description of the phenomena will be now reported.

A first dynamic frequencies analysis of tests results showed peak frequency within the range of 1-2.2 KHz.

Is important to discern between the tunnel test sampled data and those gathered through CFD software. While the tunnel test data are obtained through the analysis of sample extrapolated with 172 high pressure frequency transducers, with sample interval of 0.1s or 0.0333s, the whole physical time of the CFD simulations was 0.05 s. Therefore, the difference in this sample time date may cause a slight difference in the averaged sample, indeed the CFD simulations may obtain a converged average but not covering the whole physics tunnel experiment time. Also, the level of captured unsteadiness for CFD simulation is a strong function of the turbulence model applied and of the grid refinement.

The tunnel test analysis defined the 165 0° AoA case as periodic characterized by sharp distinct peak double peak with relatively large amplitude and with 2.0 and 2.2 kHz. Moreover, related to the lack of sinusoidal waveform, the analysis revealed the presence of a series of frequency components multiples of the fundamental frequency, namely harmonics. (i.e. 4.5 kHz, 6.7 kHz). Hence, showing good agreement with the test analysis data, the computational calculation predicts a dynamic peak frequency within 1.7-2.1 kHz, depending on the model applied(i.e. grid used, mesh refinement, turbulence model etc).

In conclusion, the dynamic frequency analysis confirmed the predicted unsteadiness related to the triple point oscillation, which generates ring vortex shedding within the subsonic regions , and defined the shape and magnitude of the dynamic peaks.

4.2 Introduction to Star CCM+

STAR CCM+ (simulation of turbulent flow in arbitrary regions-computational continuum mechanics) is commercial software for Computational Fluid Dynamics based on the finite volume element method.

The finite volume method is based on the discretization of the governing equations written in integral conservation forms. The integral form allows the presence of discontinuities inside the control volumes and then is preferred to the derivative form. Indeed the application of the integral form of the governing equations is needed when using balance equations to calculate a flowfield containing shock wave. The discretization of the unsteady Navier Stokes equations, the governing equations, is either a spatial and temporal discretization. The adoption of these methods allows the transformation of the partial differential equations into a system of algebraic equations. Therefore the physical domain is divided (discretized) into control volumes, finite volumes cell, characterized by a computational node assigned to the center of each cell: the variable relies upon the cell center, and the solution of the discretized equation is obtained in the node of each volume cells. The set of these control volumes forms the mesh. Each control volumes contain also a series of face planes and to represent the solutions within the faces, surface and volume integrals interpolation methods are also required. In conclusion, the conservation laws hold for each cell but also for the computational domain as a whole and

boundary conditions are applied to the boundary surface of the computational domain.

The CFD analysis through STAR CCM+ could be divided into three main steps:

Pre-processing: where the geometry, the fluid domain, the mesh adopted, the physics of the model, the boundary conditions and solvers adopted are described;

Simulation: where the software solves the flowfield through the application of numerical methods contained in the solvers adopted.

Post processing : where the analyses of the results are obtained through qualitative and quantitative studies.

4.3 Simulation Setup

4.3.1. Geometry

The geometry used is strongly dependent on the model adopted for the Langley Research Center Unitary Plan Wind tunnel test, which was elaborated after pre-test CFD solutions aimed to avoid tunnel interface during the experiment. The baseline for the model is reported in the following picture.

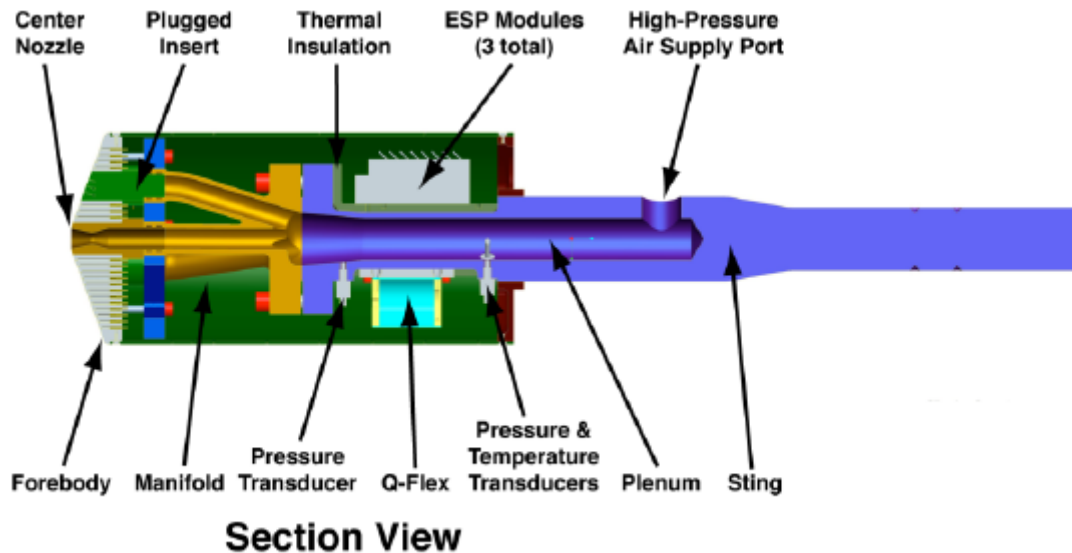


Figure 41-Section view of the model baseline

As depicted before the baseline is a 5 inch diameter , 70 degree sphere cone forebody, with a nozzle characterized by a 4:1 exit-throat section ratio. The aftbody is a cylindrical body with a main length of 10 inches. The main difference between the experimental model and the geometry adopted in the simulation relies on the simplification adopted when simulating an expanding flow through CFD. The sting which originally feeds an internal plenum connected to each nozzle via manifold is eliminated, together with the plenum and corresponding manifold. Taking into account the baseline configuration of the 165 test run case, only the central nozzle configuration was modelled . Thus, despite the huge amount of instrumentation and the complexity related to the geometry adopted for the validation experiment, only the nozzle design, and the forebody-aftbody main features were useful for the realization of the geometry. This simplification between the reference geometry and the simulated one is related to the lesser difficulty to implement the same physical problem through CFD.

Moreover, considering the test reference case 165 as axisymmetric , the whole simulation is realized considering half of the model. Thus the geometry drawn represents half of the complete model. Also , due to the simplicity of the body to be represented, there was no need to use CAD software, but the drawing of the geometry was made in the STAR CCM+ section.

The sketch drawn to represent the nozzle will now be reported. As introduced, the values used to build these sketches are derived from Appendix A of reference [30], which contain a complete description of the geometry adopted in the experiment.

For simplicity, a conversion from inches to meters is also reported.



Figure 42-Nozzle section , derived from the sketch of the geometry adopted in the simulation

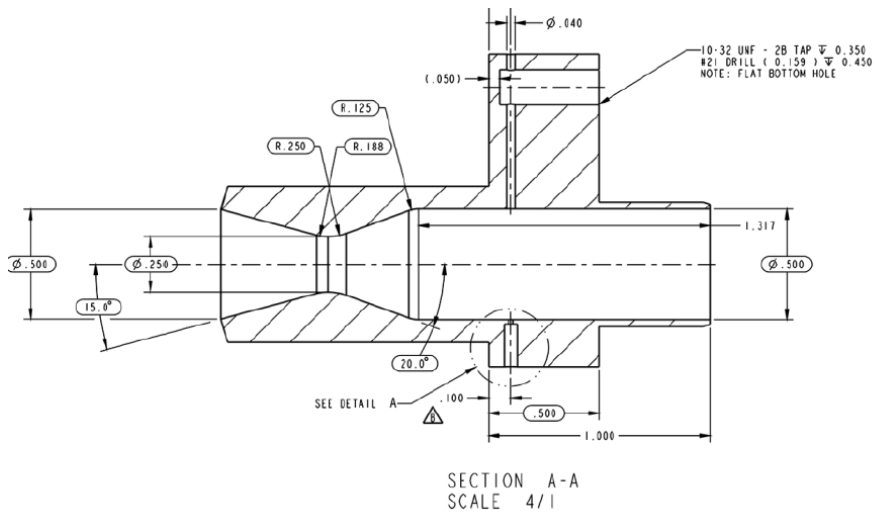


Figure 43-Centerline nozzle section adopted from appendix A

Table 6- nozzle main features dimension

	Reference values (inch)	Converted values (m)
Nozzle exit section radius	0.25	0.00635
Nozzle throat section radius	0.125	0.003175
Nozzle convergent part	0.457	0.0116
Nozzle divergent part	0.3	0.0763
Nozzle reservoir length	1.317	0.03345

Following the nozzle construction, the forebody and aftbody were drawn. The aftbody , which were composed of two thin half cylinders, is now a single cylindrical block built through a straight line and connected by a circular junction to the forebody. Hence, the forebody is inclined 70 degrees from the forebody, in accordance with the initial assumptions.

The aftbody and forebody sketch will be reported, with a table summarizing the dimension of the main features.

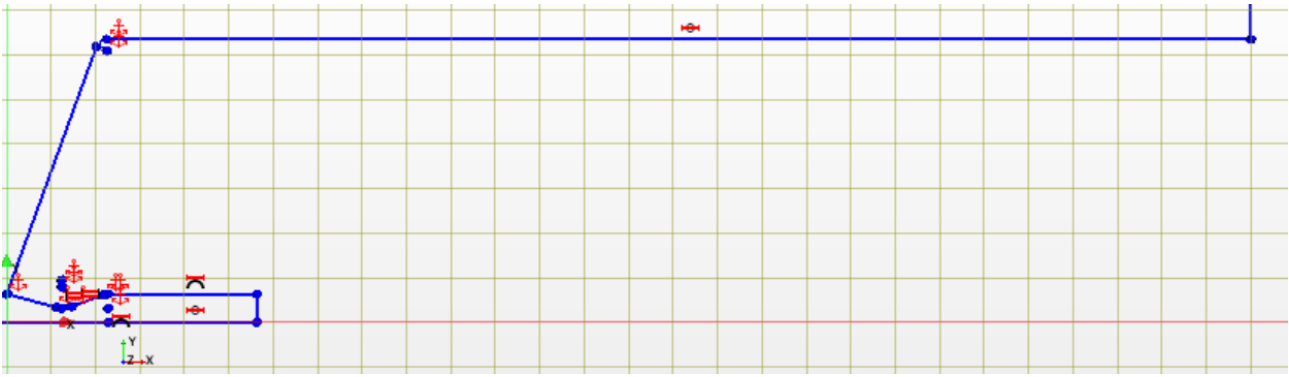


Figure 44-Aftbody and forebody sketch, with the blue line highlighting the contours of the bodies

Table 7-aftbody and forebody main features dimension

	Reference values (inch)	Converted values (m)
Aftbody length	10	0.254
Forebody convergent part	2.328	0.059
Rounded junction radius	0.1	0.00254

Once the nozzle and body sketch was completed, the whole structure was located into a square control region.

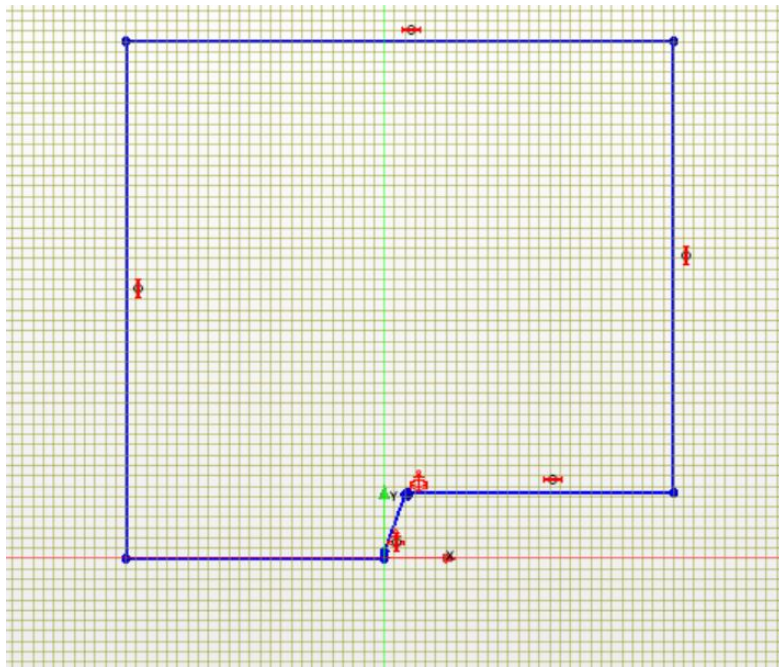


Figure 45-global sketch

This square region has a characteristic size of 0.53 m and reproduces the attribute of the wind tunnel test where the 70-degree sphere cone body was tested. Indeed the region allows the simulation of the freestream propagation, and the dimension of the region are selected in order to allow the complete evolution of the flow.

However, the passage from sketch to the 3D CAD happens through an extrusion though the body is subtracted to the volume extruded : the simulation is aimed to study the flowfield interaction between the

freestream and exhausting jet, and the effect on the body surface. For the nozzle case simulation, the only internal part of the body extruded is the nozzle, where the expansion of the flow through the convergent-divergent is simulated and studied.

The extrusion has been carried out in the direction of z-axis perpendicular to the x-y plane for only 2 mm, as a two-dimensional approach was used to study and solve the problem. The dimension along the z-axis is negligible, as far as control surfaces instead of control volumes will be created.

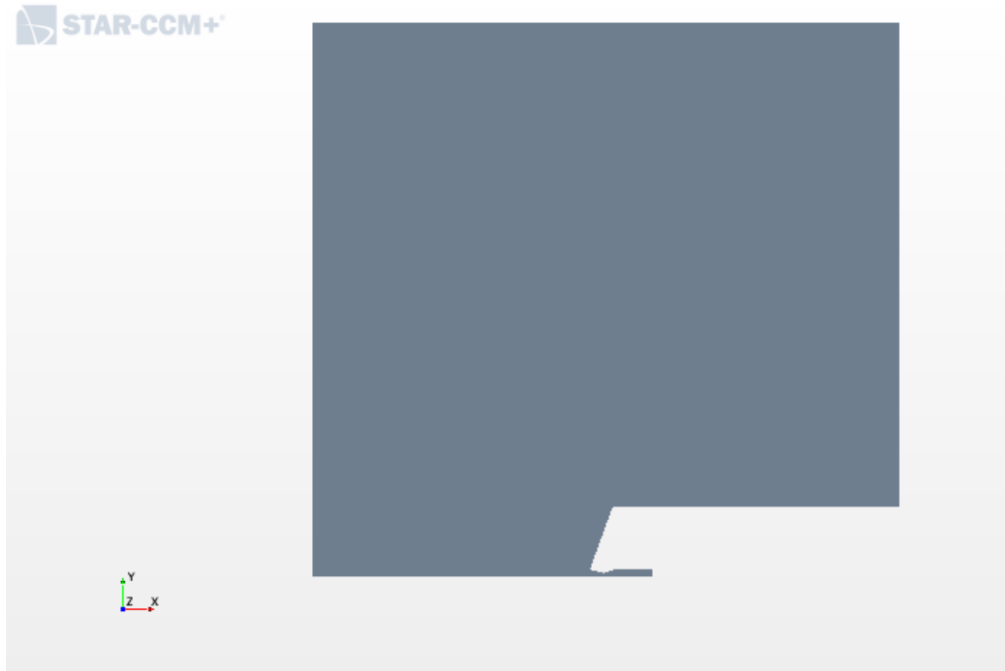


Figure 46-global view of the extruded model

4.3.2. Regions and boundary condition

Subsequently to the CAD creation, it has been possible to determine the several parts composing the whole body. These parts, are geometry parts, defined as a collection of surface curved addressed to one object (the body). In order to execute the mesh to these part, they must be assigned to one or more region: it is not possible to execute the mesh for a part by itself, but the mesh model shall be generated for one or more regions.

Regions are volume domain, or area in the 2 D case, surrounded by boundaries. Regions are discretized by continuum mesh, composed of connected faces, cells, and vertices. In the elaborate simulation, only one region has been created through the tool "assign parts to regions".

This region is characterized by the mesh and physics continuum later specified, and defined as fluid, so associated with a gas continuum, excluding any porous modelling. Even if the elaboration of just one region, several boundaries exist.

Boundaries are dependent on the part definition, indeed during the assignation of parts to region, boundaries are created for each part surface. Boundaries are surface surrounding and defining a region: discretizing a boundary corresponds to the surface bounding the volume mesh for the region. [34]

The boundary types used in the simulation are the following :

- Axis: constituting the axis of an axisymmetric region;

- Free stream condition: describe the evolution of a freestream, generate at the far-field boundary, and based on the assumption of irrotationality and quasi-1D flow in the normal direction of the boundary. This condition allows the simulation of external, compressible flow generated far from the body. The three input parameters needed to build this condition are the Mach number, static pressure, and static temperature; the software is then able to extract the other field's values through the compressible gas equation.
- Stagnation inlet boundary: is used to stabilize the inlet flow condition through the definition of total pressure, total temperature, and flow direction and simulate an internal flow with known stagnation condition. For the supersonic flow condition, the supersonic exit pressure is also required, and by the definition of this value is possible to obtain the Mach number characterizing the flow. The stagnation inlet refers to the conditions in an imaginary plenum far upstream and is useful to introduce the inlet condition for supersonic flow, which is defined by a hyperbolic regime
- Wall : represent an impermeable surface confining with the fluid regions. For this viscous computation, the no-slip condition is applied : this condition imposes that the fluid is stick to the wall , and the tangential velocity of the fluid corresponds to the tangential velocity of the wall. In other words, for a fixed wall , the tangential velocity of the fluid in contact with the wall is 0. In addition, an adiabatic condition is imposed, preventing the heat transfer across the boundary.

The several boundaries with their characteristics are summarized in the following table and figures.

Table 8-boundary types

Boundary	Type
Capsule flat part	Wall
Capsule rounded junction	Wall
Capsule conic part	Wall
Freestream outflow	Freestream
Freestream inflow	Freestream
Top wall	Freestream
Nozzle convergent joint	Wall
Nozzle divergent	Wall
Nozzle convergent	Wall
Nozzle throat	Wall
Inlet	Stagnation inlet
Reservoir	Wall
Symmetry	Axis
Inferior reservoir	Axis

To simulate the jet expansion , a stagnation inlet condition with total static pressure set to 0 has been set in the reservoir lateral wall: this condition allows the simulation of the jet expansion starting from a quiet condition in the reservoir ,till supersonic condition at the nozzle exit.

The freestream conditions have been set up in the lateral and superior boundaries of the region; the values characterizing the freestream flow are depicted in the following table, and are aligned with test case 165 freestream condition.

Table 9-freestream conditions

Mach number	Static pressure	Static temperature
4.6	536.65 Pa	65 K

Wall condition has been imposed on the body parts : for the nozzle component and the aft-body and fore-body parts an adiabatic condition coupled with fixed wall has been set, imposing tangential velocity equal to 0.

In addition , the lower boundaries represented by the inferior part of the reservoir and the inferior boundary of the region, have been simulated as a symmetric axis, aligned with the physics model that will be soon described.

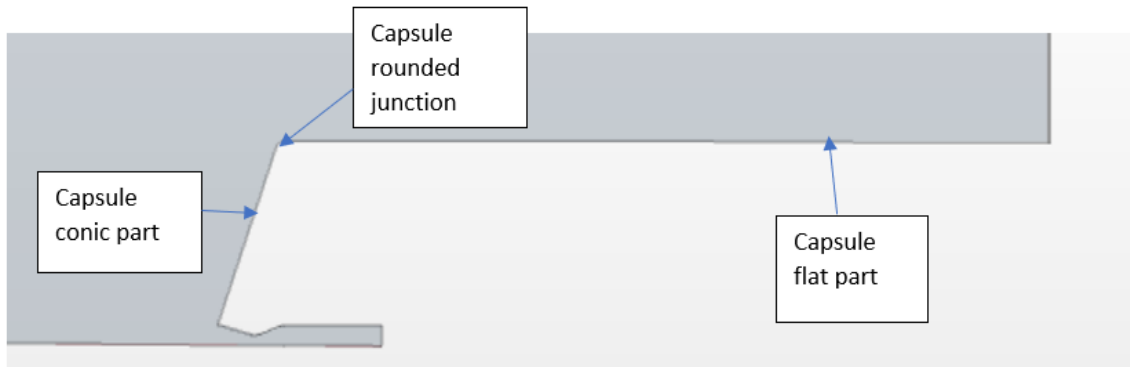


Figure 47- aftbody and forebody boundaries

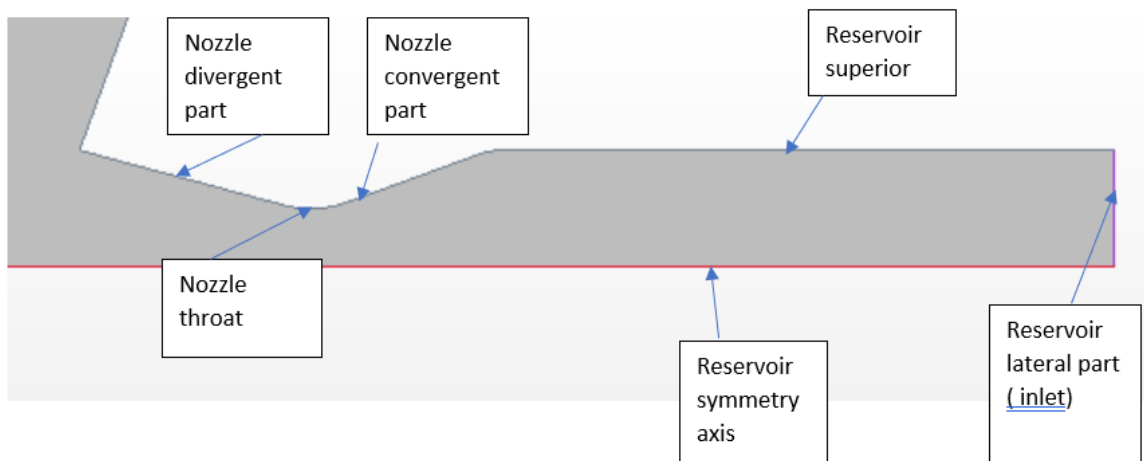


Figure 48-nozzle and reservoir boundaries

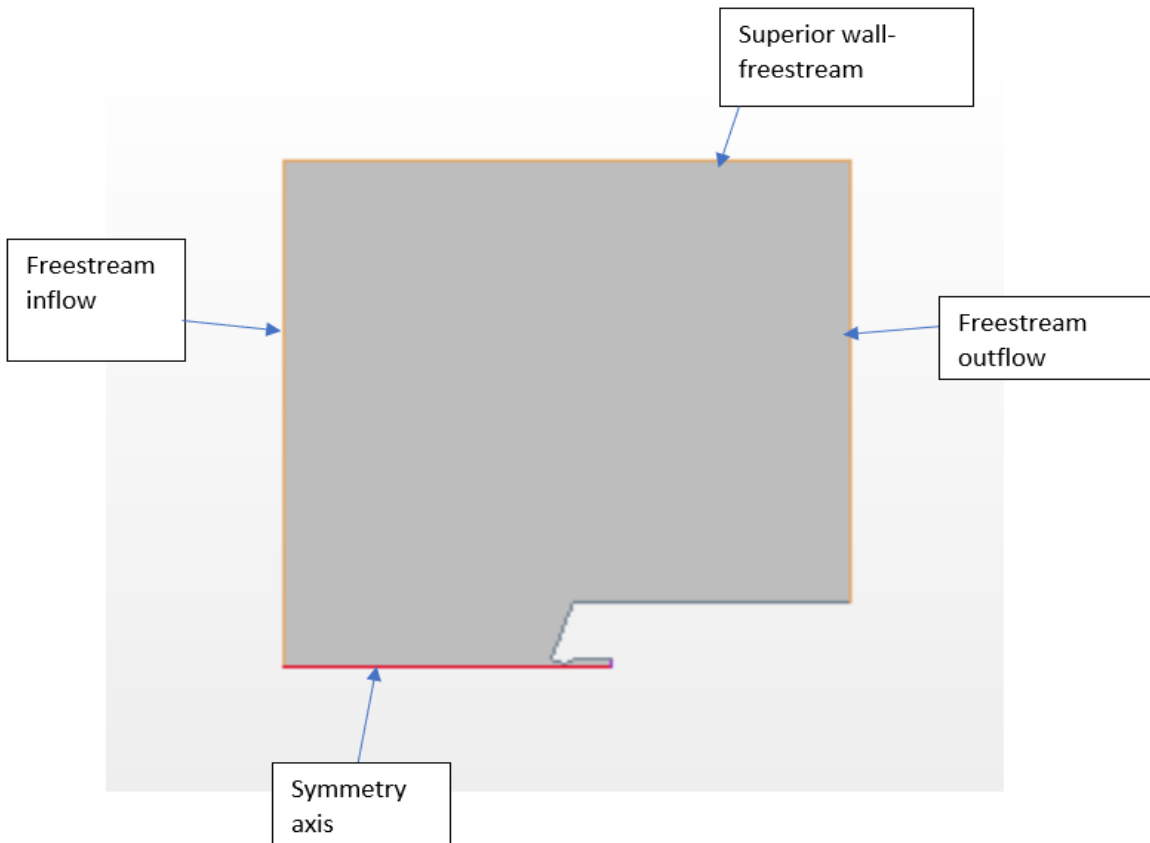


Figure 49- lateral boundaries of the region

4.3.3. Physics models:

The physics continuum allows defining the whole set of models that describe the physics of the problem. Indeed these characteristics are independent on the mesh and determine whether :

- The continuum is 3 D or 2D;
- The model comprises a solid, liquid or gas
- Stationary or unsteady approach;

The aim of the physics model selection is to identify the primary variables of the simulation and mathematical formulation used to generate the solution.

Axisymmetric model : considering the reference test case 165, the predicted flowfield with 0° AoA is axisymmetric. Thus, the adopted model is the two dimensional axisymmetric, which works with a two dimensional mesh. The use of this model requires that the boundary edge lies along the inferior axis must be a symmetric axis, as depicted in the section before.

Gradients :allows the calculation of gradients variable, required at cell centres and at cell face centre for different purposes. This calculation is computed through the Hybrid Gauss LSQ method.

Gas : aligned with test reference case, and CFD simulation, air with its standard parameters is used for simulating the expanding jet and the incoming freestream.

Ideal gas equation : is used to express the ideal gas laws in order to compute the density value as a function of pressure and temperature; the validity of the ideal gas state equation is also ensured for compressible flow regime.

Coupled flow and coupled energy models, are suitable to compressible flow, or flow involving in high supersonic or hypersonic regimes. These models induce that the conservation equation for continuity, momentum and energy are solved in a coupled manner, simultaneously as a vector of equations. The velocity field is obtained from the momentum equations, and the continuity equation provides pressure useful for evaluating density by the equation of state.

In the simulation the discretization of convective and diffusion terms is implemented with a second-order scheme. Moreover, it is possible to set the discretization of inviscid flux with Liou's AUSM + flux vector splitting scheme, based on upwind concept.

The coupled flow model solves the conservation equations using a pseudo time marching approach. The solver is used for implicit spatial integration in the unsteady approach using a coupled algebraic multi-grid method for solution.

Implicit unsteady : the implicit unsteady approach is used to describe the nature of SRP flowfield, considering the unsteadiness predicted in both experimental and numerical studies; the implicit unsteady model uses the implicit unsteady solvers, matched with the coupled implicit solver. In this type of simulations, time is a variable that shall be discretized in addition to the spatial discretization. The discretization divides the initial interval into time steps; each physical time step involves some number of inner iterations to converge the solution for that given instant of time. These inner iterations can be accomplished using implicit spatial integration: the integration scheme uses, as depicted before, a time marching method, thus marching inner iteration using optimal pseudo time steps that is derived from the Courant number.

The implicit unsteady setup, requires the determination of the time step adopted and the discretization of temporal terms. The discretization is implemented with a second-order temporal scheme, and physical time step size is 10×10^{-6} ; this time step is based on the transient phenomena that governs the phenomenology, and is also aligned with reference predictions. [31]

Viscous laminar approach : due to the viscous phenomena related to the SRP flowfield, a viscous approach is required. In this flow regime, as depicted before, the governing equations are the Navier Stokes. Despite the assumptions led by a laminar approach, i.e. orderly particles motion, or fluid thin layers sliding all parallels to each other, the transition from laminar to turbulent is not yet well understood for SRP flowfield and a laminar approach has been retained enough to predict the whole flowfield.

Solution interpolation : is useful to interpolate the solution computed on certain volume mesh to a newly generated volume mesh. The technique applied is the nearest neighbour which "maps the solution data from one mesh to another comparing the cell centroids in each mesh, thus the new cell gets the solution data from an old cell whose cell centroid is closest to its own". [34]

Wall distance : represents the distance from a cell centroid to the nearest wall face with a non slip boundary condition, various models require this calculation to account for near wall effects, and the calculation is computed through the implicit tree method. [34]

To conclude the description of the physics models is important to introduce the initial conditions adopted for the simulation and the stopping criteria used for stopping the simulation. The initial conditions have been obtained through a field function programmed with the STAR CCM+ programming language : this field function placed into the initial conditions tool, distinguishes between the initial conditions inside the nozzle and outside. Indeed, the initial conditions adopted outside are the freestream condition, while inside the nozzle the initial conditions are described in terms of total jet pressure and total jet temperature

to correct simulate the jet expansion starting from the reservoir and proceeding into the convergent-divergent nozzle.

With regard to the stopping criteria, maximum physical time of 10 s, maximum 1000 iteration and 10 inner iterations have been set; however this parameters doesn't affect the simulation results and could be modified in progress.

4.3.4.Mesh

Considering the axisymmetric physics of the problem, a 2D mesh has been carried out. The discretization of the spatial domain has been achieved through the STAR CCM+ tool “automated 2D mesh”, which exploits a specified mesher to generate the grid.

The selected meshers are :

- “polygonal” , which allows the creation of a grid initially composed of triangle or quadrilateral shaped cells which then are converted to polygon shaped cells.
- “prism layer mesher”, which allows a better discretization of the region domain near the wall surface or boundaries, and is important to improve the accuracy of flow solution in characteristics regions as the boundary layer. The prism layer mesher creates layers of orthogonal prismatic cells next to the wall surface.

The resulted unstructured mesh allows an easier grid refinement and the representation of complex geometries without increasing the mesh resolution.

The main feature of the mesh adopted was the customization of the calculation domain through the surface and volumetric controls. The outer region where the freestream flow is unperturbed has been defined by the global mesh conditions, which results in the increase of the cell size. Indeed the default controls within the mesh definition have been mainly

applied in this flowfield region, and constitute a baseline for the definition of the mesh characteristics in the other domain zones.

Therefore, in regions of interest, refinement has been adopted. These regions are either regions where fluid dynamic phenomena occur and surface with curvature, corner, or particular geometry. Thus a finer mesh, reducing the cell size, augmenting the number of faces, and thickening the whole mesh structure has been adopted. Mesh refinement increases the precision of the numerical computation and thus solution.

The mesh thickening has been obtained through control surfaces and volumetric control, which enable the creation of several refinement parts inside the simulation. The surface controls have been adopted to model body surfaces and boundaries such as the whole nozzle, the aftbody and the forebody. The volumetric control has been used to refine the

parts of the calculation domain that simulate the fluid dynamics interactions and fluid evolution.

Surface controls specify alternative mesh and prism layer settings for the selected part. The customized parameters have been the minimum surface size, target surface size, prism layers values and surface curvature.

Volumetric control, enables the specification of the cell size in a specified zone, exploiting the creation of volume shapes. To implement the volumetric controls, the volume shaped adopted has been a cone, positioned in the region where the relevant fluid dynamics interactions have been predicted. Implementing the volumetric control through the creation of the conic shape enables the mesh refinement in the whole region surrounding the body, which is interested in the interaction of the exhausted jet plume and incoming freestream. During the volumetric control, prism layer parameters have been maintained constant, to maintain unaffected the resolution of the near-wall layer of the body parts. The growth rate for each core mesh model determines the transition in cell size from the volumetric control to the core mesh. The possibility to modify the mesh refinement in this area through the parameter

set in the “custom-size” window, makes further grid refinement really simple.

The following tables summarize the mesh conditions and main controls

Table 10-Default mesh condition, unperturbed outer region<

Base size	0.00635 m
Cad Projection	Enabled
Part Priority	Default
Target surface size	500 (percentage relative to base)-0.03175 m
Minimum surface size	50 (percentage relative to base)-0.003175
Surface curvature	#Pts/circle-36
Surface proximity	Search floor technique-minimum gap size : 0 m
Surface growth rate	1.3
Number of Prism layers	2
Prism layer near wall thickness	1e-05 m
Prism layer total thickness	33.33(percentage relative to base), 0.00211 m

The following table summarizes the surface control conditions adopted for the mesh refinement of the nozzle convergent, nozzle divergent, nozzle throat and the superior part of the reservoir. The refinement has been carried out by decreasing the target surface size, the minimum surface size and the prism layer total thickness, while increasing the number of prism layers maintaining constant the thickness of the first prism layer near the wall. In addition, the increase of points/circle values, allows a better refinement of surface curvature. Moreover, surface proximity and surface growth rate have remained unchanged with respect to the default controls of the outer region.

Table 11-Default mesh conditions, nozzle parts

Target surface size	2.0 (percentage relative to base) 1.27*10e4 m
Minimum surface size	1.0 (percentage relative to base)6.35 *10 e-5 m
Number of prism layer	10
Prism layer total thickness	4.0 (percentage relative to base)2.54 *10 e-4 m
Prism layer wall thickness	1.0 *10 e-5 m
Surface curvature	#pts/circle 180

To reduce the total cell amounts , the prims layers mesher has been disabled for the superior top wall, which constitutes the upper boundary of the calculation domain .

The mesh refinement controls adopted for the forebody, aftbody and rounded junction at the corner of the forebody are summarized in the following table. Moreover, the refinement has been carried out acting on the prism layer values and the surface curvature. The number of prism layers is increased up to 10, while the prism layer total thickness is decreased with respect to the default condition of the outer region, while not varying the prism layer thickness near the wall. Even in these regions a surface curvature refinement has been applied, augmenting the number of points over a circle. However, target surface size, minimum surface size, surface growth rate and surface proximity have remained unchanged with respect to the default control of the outer region.

Table 12-Default mesh conditions, aftbody, forebody and rounded junction

Number of prism layers	10
Prism layer total thickness	6.0 (percentage relative to base) $3.8 * 10^{-4}$ m
Prism layer wall thickness	$1.0 * 10^{-5}$ m
Surface curvature	#pts/circle 72

In conclusion a mesh refinement has been applied to the inferior part of the reservoir. The following table summarizes the refinement controls adopted. The only difference with the nozzle parts refinement is the absence of the prism layer mesher, due to the nature of the inferior part of the reservoir, which is model as a symmetric axis.

Table 13-Default mesh condition, inferior boundary of the reservoir

Target surface size	2.0 (percentage relative to base) $1.27 * 10^{-4}$ m
Minimum surface size	1.0 (percentage relative to base) $6.35 * 10^{-5}$ m
Surface curvature	#pts/circle 180

The volumetric control realized through the conic shape, set the refined surface size that is applied to faces within the volumetric range of the parts in the control. Thus the selected size is elaborated as a function of a reference size, namely “csize_min”, which is related to the nozzle diameter. Indeed, as for the base size, this reference length is set to the scale of the object of interest.

Table 14- Default mesh condition, volumetric control

Csizemin = Nozzle diameter/50;	4.0 (percentage relative to base) $2.54 * 10^{-4}$ m
Custom size for the volumetric control	16(percentage relative to base) $1.16 * 10^{-3}$ m
Nozzle diameter	0.0127 m (2*base size)

The following table reports the whole set of elements that better describes and discretizes the whole geometry.

Table 15-total number of cells, interior faces and vertices for the adopted mesh

Total number of cells	189910
Total number of interior faces	560134
Total number of vertices	362021

In order to study how the grid definition affects the ability to capture the unsteady phenomena, in the frequency analysis depicted in section 4.7.1. a mesh refinement has been applied, with a modification and

refinement of the region inside the cone shape. To refine the grid in this region, the custom size of the volumetric control has been halved to $5.8 \cdot 10^{-4}$. Even in this simulation, the prism layer parameters have been maintained constant. The comparison between the total number of cells, vertices, and faces between the basic mesh and the refined mesh in 4.7.1. section, is reported in the following table.

Table 16.-comparison between the two adopted mesh

	Initial mesh	Refined mesh
Total number of cells	189910	713752
Total number of interior faces	560134	2132947
Total number of vertices	362021	1421184

The following figure summarize the depicted assumptions and represents the mesh generated .

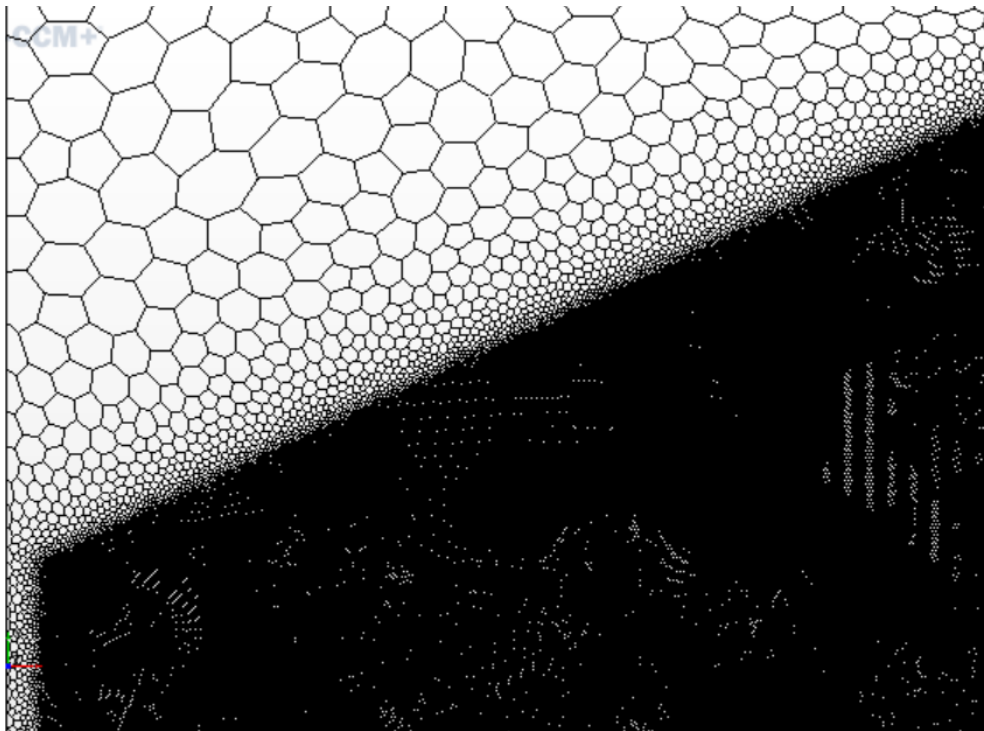


Figure 50-outer unperturbed region mesh vs mesh elaborated inside the volumetric control

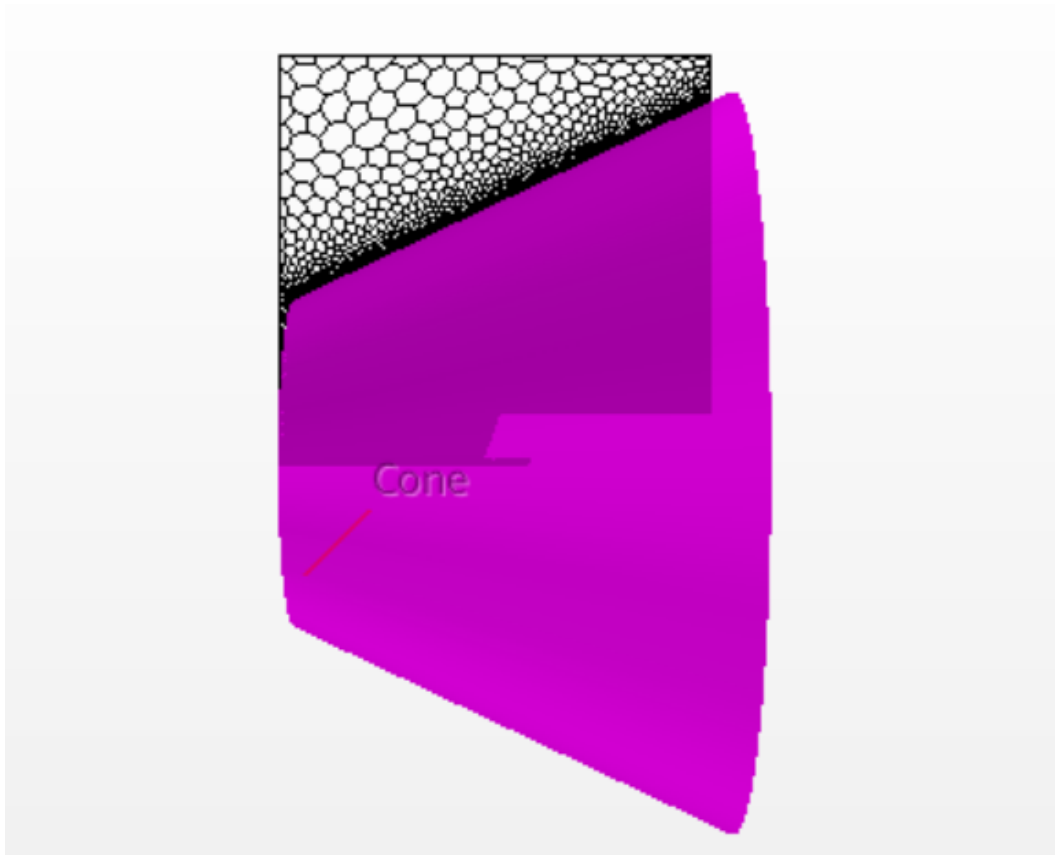


Figure 51-cone shape adopted for the volumetric control

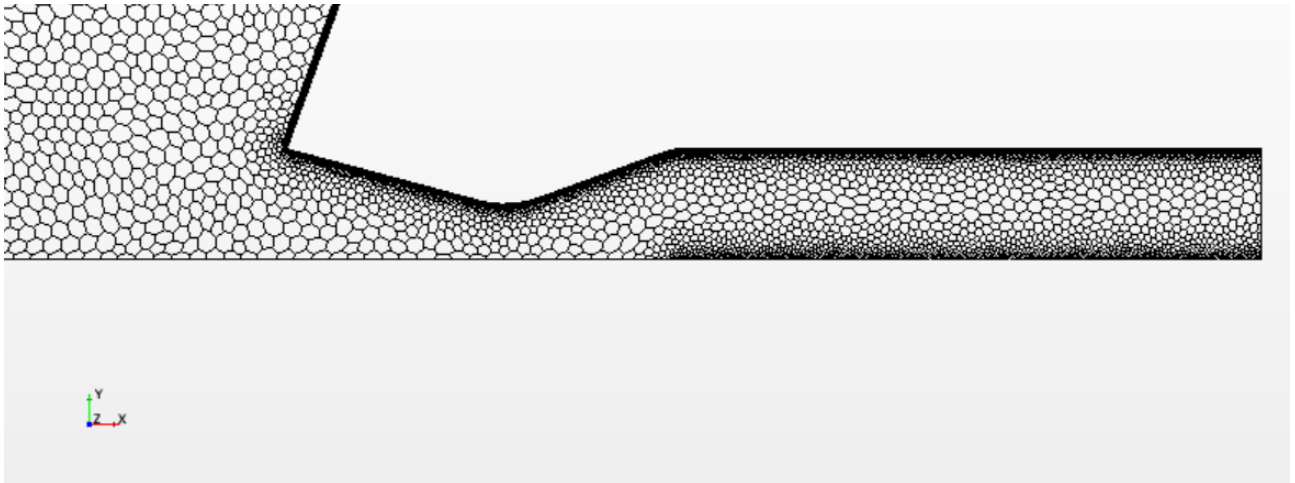


Figure 52-Nozzle and reservoir grid



Figure 53- aftbody, forebody and rounded junction grid

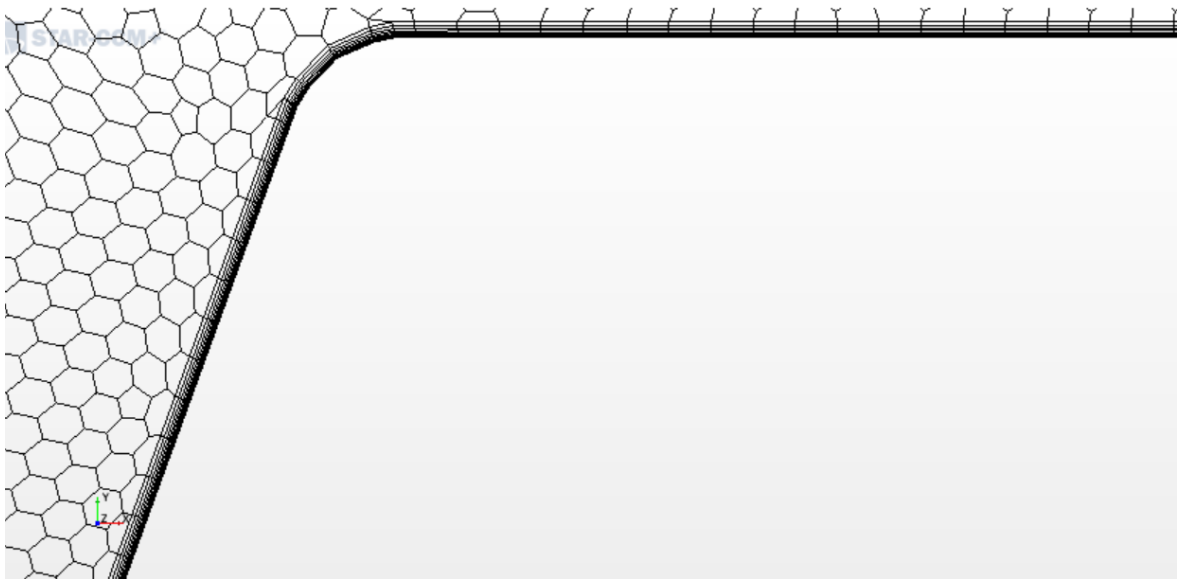


Figure 54-zoom on the prism layers structure

4.4. Results- Nozzle case

For unsteady simulations, the study of convergence through the residual plot loses its meaning. While for a steady simulation residual plots may be indicative of a converged solution when the values are reduced toward or below $10e-03$, for a transient simulation the residual monitors is mainly used to understand if the solvers are behaving correctly.

For an unsteady simulation is expected a “saw tooth” pattern : within each time steps the residuals decrease , showing convergence of the solution during that time step, but the decrease is interrupted when passing to the following time step. Moreover with the increasing of the iterations a good residuals plot profile expects a relatively smooth variation, and successive spikes with the same eight.

Thus, the residuals plot elaborated for the simulation for the last 50000 iterations up to the solution time considered is here reported.

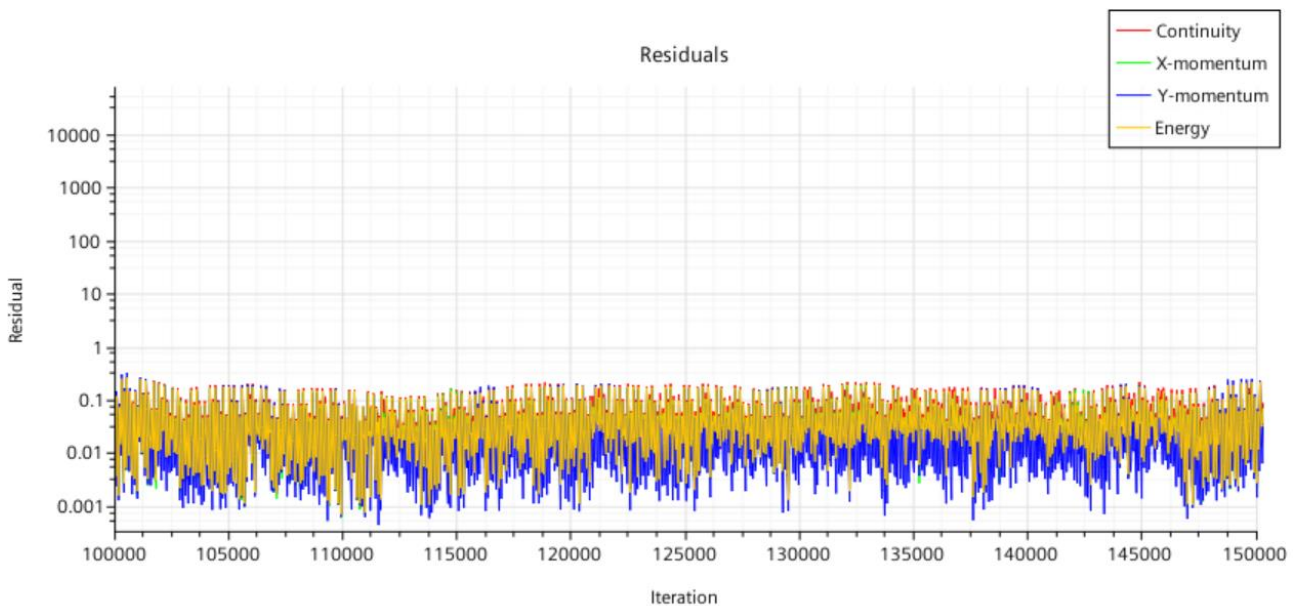


Figure 55-residuals plot for the las 50000 iterations up to the current solution time

The plot is aligned with the previous consideration, underlying the stable solvers behave, which not presents any instabilities .

During the computational calculation, the Courant number controls the size of the local time steps used in the time marching procedure. In order to maintain the stability through the simulation, and considering the implicit methods used , a linear ramp has been applied, in order to start with a small courant number and progressively increase the value.

The comparison with experimental data, either tunnel test and CFD is both qualitative and quantitative.

4.4.1. Qualitative Comparison

The qualitative comparison is based on images representing the pressure, temperature and Mach isocontours field for an arbitrary solution time, 0.0156 s . Considering that these images refer to a fixed time, is quite impossible to underline the unsteadiness of the phenomenon and indeed a frequency analysis of dynamic peaks characterizing the unsteadiness will be later computed.

The purpose of this qualitative comparison is to highlight the flowfield main features depicted in the previous section, and demonstrate the ability of the simulation to correctly reproduce the complex interaction between a freestream flow and an exhausting jet.

The analysis of Mach , pressure, and temperature isocontours image results in demonstrating the capability of reproducing all the main features of SRP :

- Bow shock;
- Barrel shock and jet boundary;
- Stagnation region :
- Jet plume ;
- Mach disk;
- Recirculation region
- Free shear layer near the jet boundary;
- Triple point.

From the Mach isocontours plot is possible to describe the jet evolution starting from the reservoir. Indeed, the flow accelerates through the convergent-divergent nozzle , reaching a first supersonic condition in correspondence of the throat section ($M=1$), and then continuing to expand into the divergent part of the nozzle, in order to have supersonic exit condition at the nozzle exit section(i.e. $M\approx 3$) . The expansion is also remarkable in terms of pressure and temperature : starting from high values of pressure and temperature corresponding to a quiet condition, the flow expands and there's a strong decrease in these quantities notable by the tendency to assume a colour corresponding to lower values.

The expansion continues outside the nozzle exit, where the characteristic jet plume associated with high under expanded jet is formed. This region is delimited above by the boundaries of the expanding jet, constituting by the jet barrel shock and jet boundary. Inside the jet plume, the jet continues its expansion, reducing the pressure and temperature values and increasing the Mach number. Is also remarkable the pattern of the barrel shock, in accordance with theoretical predictions, which tends toward the jet axis.

The barrel shock and jet boundary surrounding the jet plume, define the separation from the supersonic zone of the exhausting jet to the subsonic region surrounding the plume. The differences between the plume core and the surrounding zone are evident in terms of pressure temperature and Mach number.

As predicted for a high under expanded jet, a Mach disk occurs and terminates the jet expansion. The Mach disk is visible in terms of pressure, temperature and Mach number: this normal shock leads to pressure and temperature increase, and a strong Mach number reduction.

As for the Mach disk, the bow shock is clearly visible and as predicted theoretically, it leads to an increase in temperature and pressure downstream the shock and a strong reduction in speed, and thus in the Mach number.

Behind the Mach shock is visible the subsonic shear layer characterizing the SRP flowfield. Indeed this region is characterized by the interaction of the exhausting jet decelerated through the Mach disk, and the oncoming freestream flow subjected to the bow shock: this subsonic region is bounded by the two supersonic regions. The interaction between the subsonic jet core and the subsonic flow behind the bow shock generates a contact surface, acting as an interface between the two subsonic flows. In this subsonic region, is also remarkable the presence of a free stagnation point formed along the contact surface in correspondence to the body axis. The free stagnation point and the interaction region, are both identified by relatively high pressure and temperature values that resume the values inside the nozzle, for temperature, or at the beginning of the jet expansion , immediately after the nozzle exit, for pressure.

As expected, due to the strong velocity gradient existing between the supersonic exhausting jet and the subsonic freestream flow moving downstream toward the aft body, a shear layer along the jet boundary is created: this shear layer is a parallel velocity mixing region formed between the barrel shock and the above subsonic flow. Either the jet exhausting flow, moving toward the aftbody after the Mach disk, and the shear layer are affected by the low pressure area near the nozzle exiting, thus forming the recirculation region between the barrel shock and the shear layer. The recirculation region is composed by a subsonic zone embedded into supersonic flow; for the shear layer above the jet plume, the boundary between subsonic and supersonic region is not clearly defined, as the flowfield evolutions along the aftbody is characterized by several interaction and different flowfield regime. The recirculation region and the high pressure behind the bow shock force mixing within the shear layer, and along the outer jet boundary between the supersonic flow and parallel subsonic recirculation flow.

In conclusion, the triple point is notable at the intersection between the Mach disk, the barrel shock, and the subsonic flowfield behind the bow shock. The presence of this point is one of the main features characterizing SRP flowfield, and its unsteadiness determines the unsteady characteristic associated with this flowfield. However, the frequency analysis will be depicted later. The presence of this point is underlined either in the Mach, pressure, and temperature isocontours and through the use of streamlines.

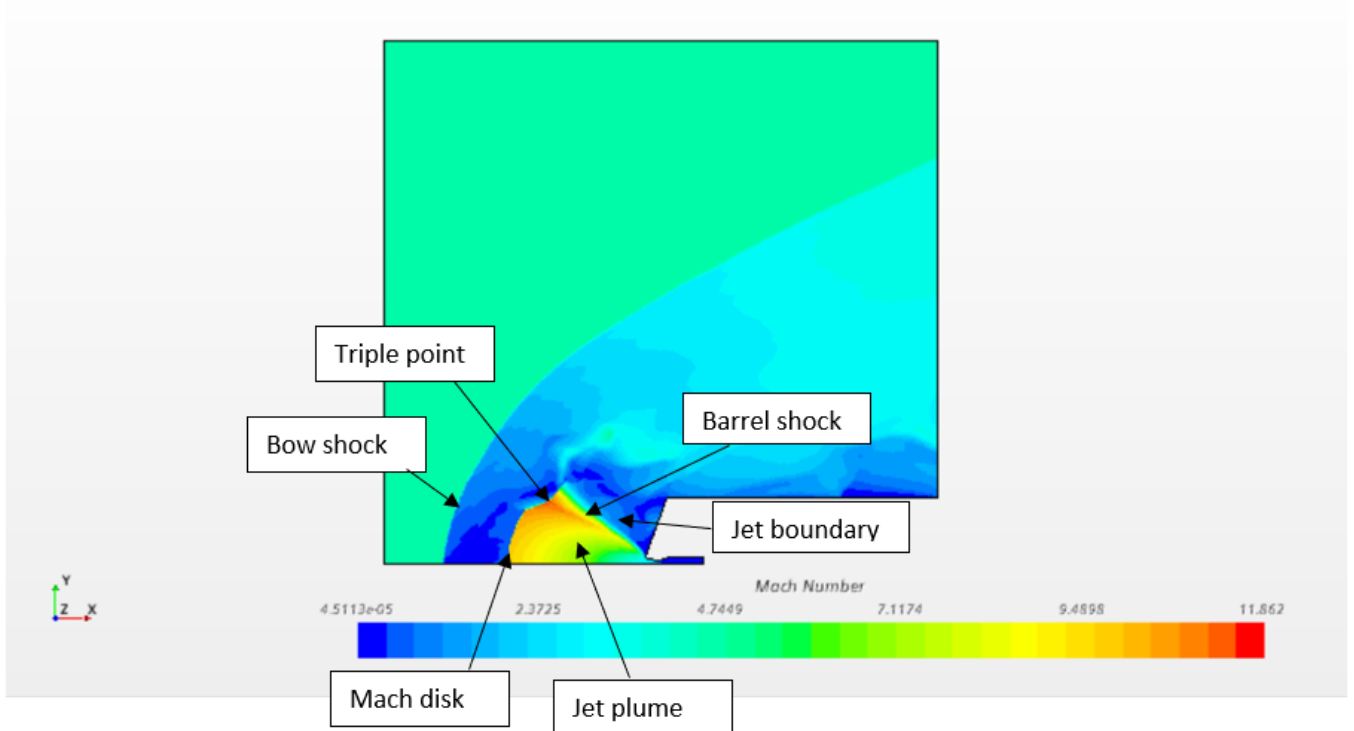


Figure 56-Mach isocontours

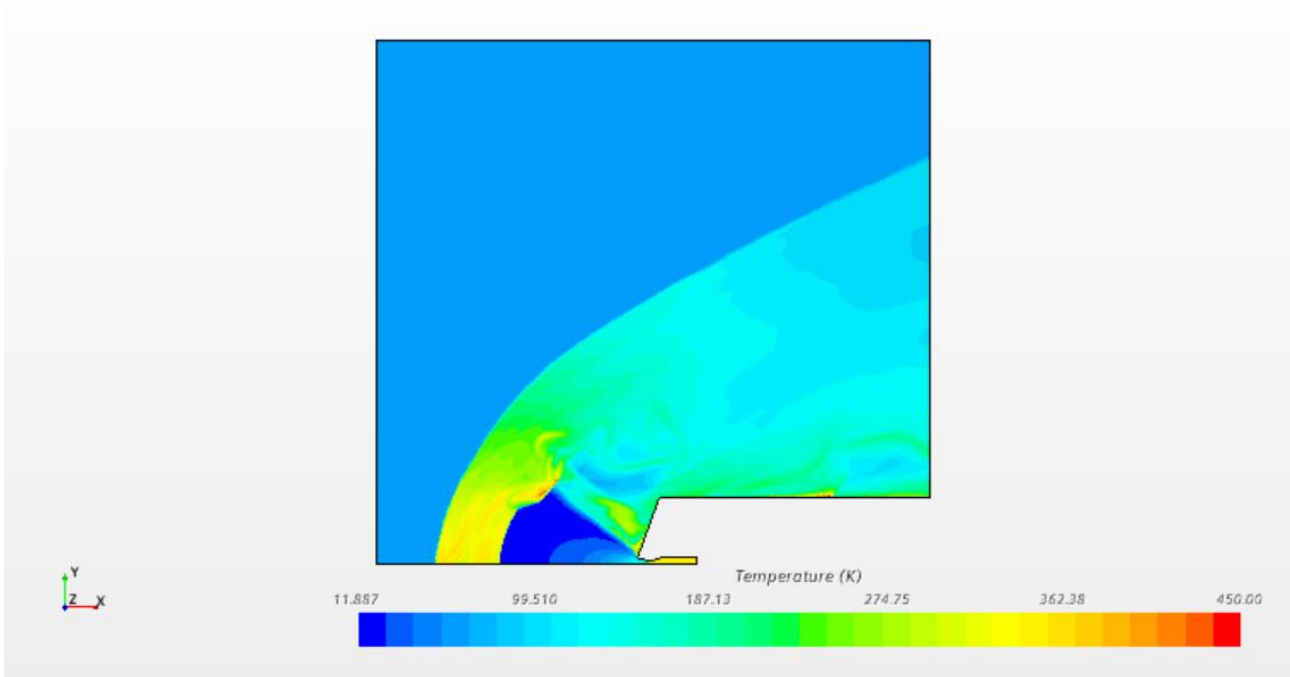


Figure 57-temperature isocontours

From the pressure plot, is remarkable the presence of a region of relatively constant pressure enveloping the body. This zone, as anticipated, is related to the presence of recirculation regions and results from the interaction between the freestream and the exhausting jet.

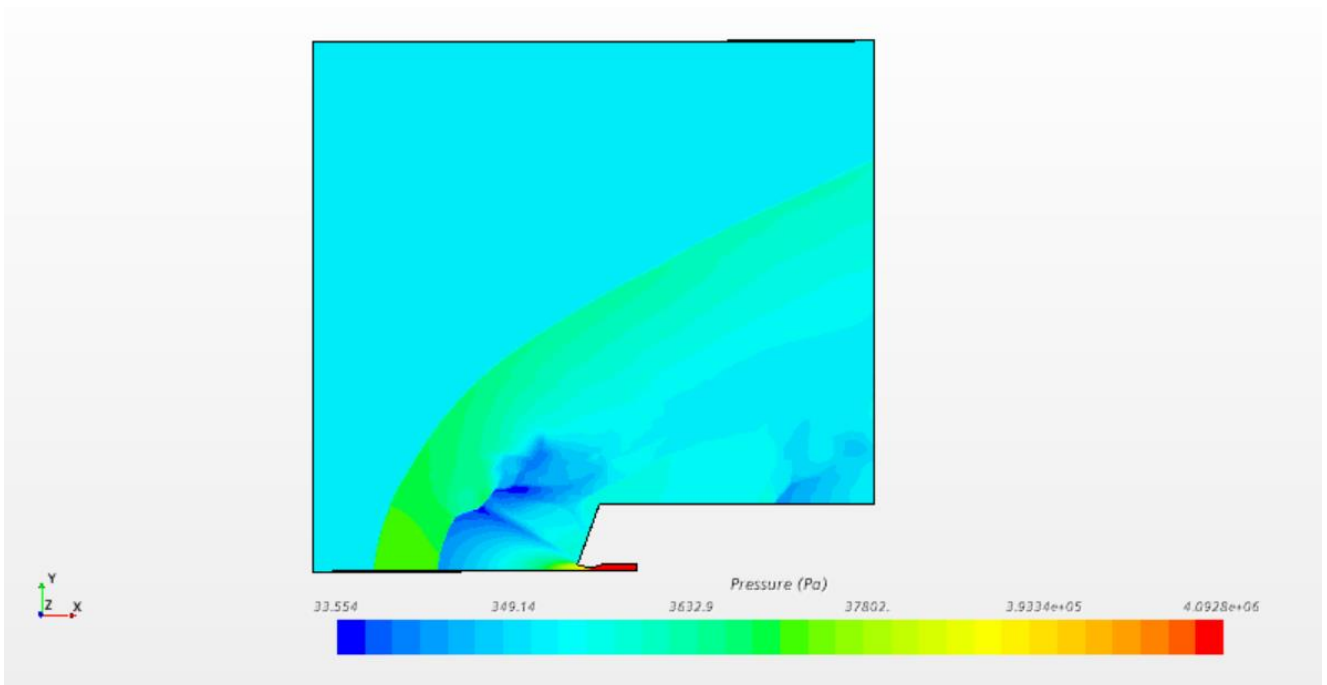


Figure 58-Pressure isocontours

Through the streamlines is possible the visualization of the contact surface and free stagnation point in the subsonic region existing between the bow shock and the Mach disk. The free stagnation point is located in correspondence of the variation of the direction of the freestream streamlines, indeed the flow is

deflected in correspondence of the contact surface and subsequently turned towards the aft body. This deflection occurs until the jet plume represents an obstruction to the bow shock: in the above region of the freestream, the freestream streamlines aren't affected by any interaction with the exhausting jet.

The streamlines also reveal the shear layer created above the jet plume, where the freestream flow and the jet exhausting flow run parallel. Indeed even the exhausting jet is turned toward the aftbody after the Mach disk.

With the visualization of the streamlines is also strongly noteworthy the presence of the recirculation region.

Even the ability to represent important flowfield features, the streamlines represent the instantaneous tangent of the velocity vector at a given point and a given instant and differ from the pathlines; to fully understand the trajectory and interactions during the evolution of fluid-particle motion, pathlines should be used.

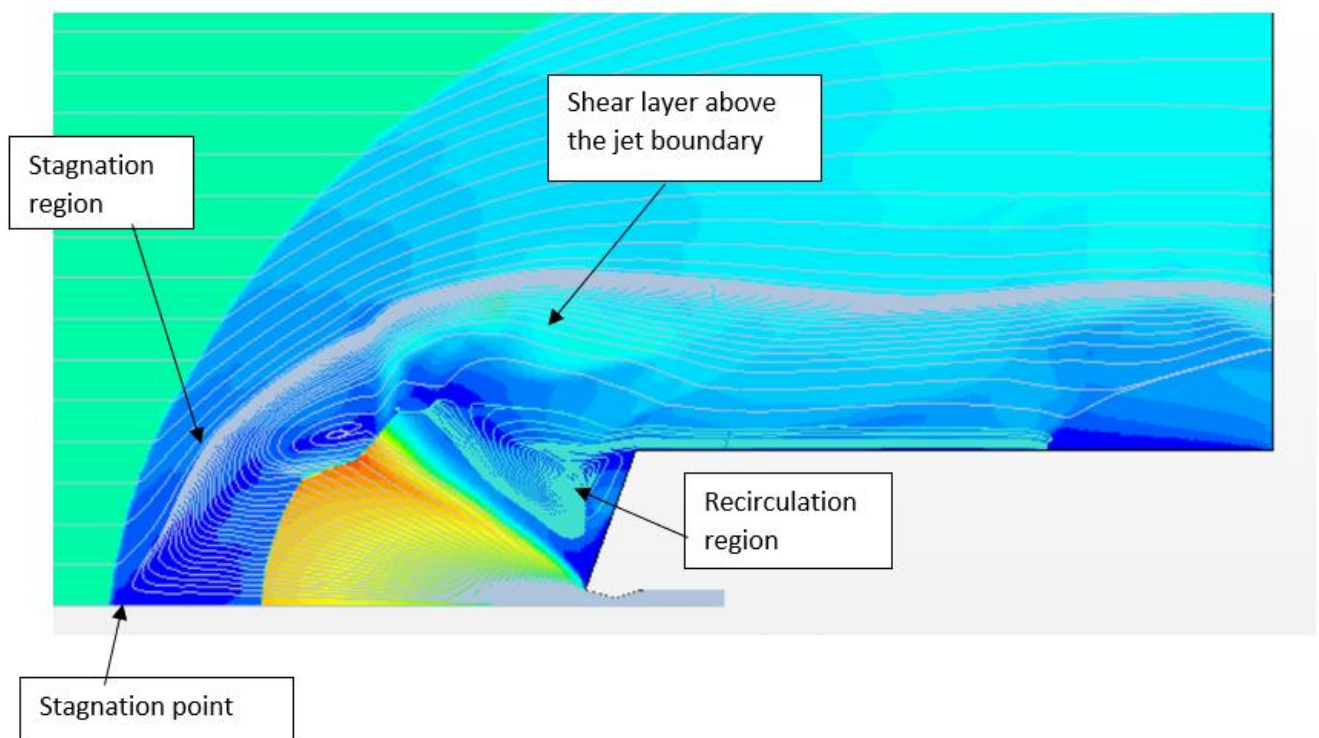


Figure 59-streamlines visualization on Mach isocontours scene

Pseudo Schlieren image

The schlieren method is used to photograph the flow of fluids of varying density and for visualize complex phenomena as shock wave, expansion waves, slip lines or shear layers, which induces pressure, temperature and density gradients. The physical principle exploited in the Schlieren technique, is based on the fact that light rays are bent when they encounter changes in fluid density, because density gradients cause variations of the refractive index. The result of the Schlieren method is the visualization of the density discontinuity through dark lines occurring where density gradients are present. Besides the difference with the experimental set up of Schlieren visualization, is possible to reproduce with a CFD simulation a pseudo Schlieren image, visualizing the density gradient inside the flowfield. With this

visualization is indeed possible to observe the flowfield structures that induce density gradient (shock wave, compression wave etc. etc) and comparing with the Schlieren images of the test reference case.

The pseudo Schlieren images are implemented through a field function where the absolute value of the density gradient is calculated and then represented into the flowfield.

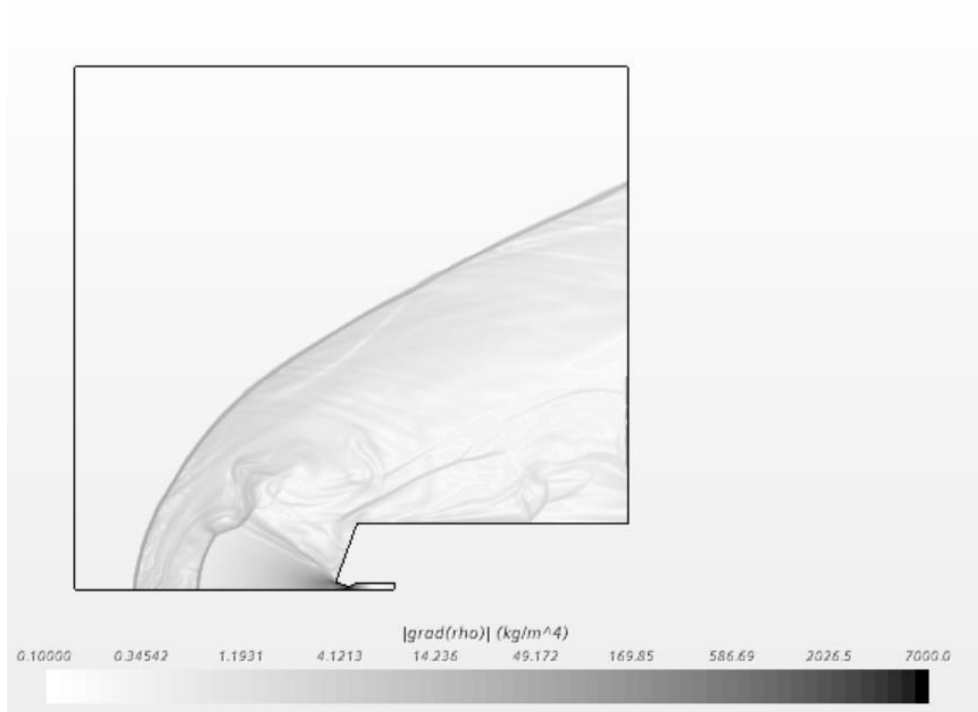


Figure 60-Pseudo Schlieren image

Through the analysis of the pseudo Schlieren image is remarkable the presence of all the SRP flowfield structures that induces density gradients: indeed the bow shock, Mach disk, barrel shock, subsonic shear layer, triple point, and the supersonic/subsonic shear layers above the jet plume are clearly visible; thus, the presence of all these features underline that the computed mesh is sufficiently refined to fully resolve the impinging shock structures.

Moreover, a qualitative comparison between this pseudo-Schlieren image and the reference images reported in the 4.1. section, demonstrates the ability of the simulation to faithfully reproduce the SRP phenomenology.

The ability of CFD code to correctly reproduce the complex flowfield of SRP emerges from the qualitative comparison between the different Mach, temperature, pressure and pseudo Schlieren plots: the code is indeed able to represent all the main features distinguishing SRP flowfield, maintaining the quantities variations range within those predicted by the experimental reference test case and the other CFD validated codes. Analysing and comparing the several frames with the reference ones, the same quantities values are encountered in the same field regions, i.e. maximum Mach number close to the triple point, pressure values into the stagnation region, temperature, and pressure values surrounding the aftbody etc.

4.4.2 Flow main features dimension

Besides the analysis of Mach, pressure, and temperature isocontours, the determination of main flow features dimension has been carried out. Therefore, despite the calculation of these quantities through the Schlieren images for the reference test case, the computation has been here implemented through the “measure distance” tool of STAR CCM+, applied in the pseudo Schlieren frame.

The comparison of these dimensions is a viable means to evaluate the ability of the simulation to produce the experimental condition and results. Moreover, this comparison represents a first quantitative comparison computed on the simulation and is useful to understand if exists a strong consistency between the simulation and the reference case.

The following table summarizes the sampled dimension, reports the main flow features dimension for the reference test case, and presents the percentage difference between these two conditions.

Table 17-dimensions comparison

	Bow shock standoff distance	Bow shock radius	Jet plume length	Maximum jet plume radius
Flow features dimensions in cm for test reference case	18.33	24.56	12.92	7.82
Flow features dimensions in cm for the simulation	18.8	25.03	12.89	7.420
Percentage difference between the two cases	2%	2%	<1%	5%

The flow features main dimensions measured for the simulation case are aligned with the experimental measurements. Indeed, the percentage difference between the two cases is less than 5% for each computations; the CFD code, underpredicts all quantities expect the bow shock radius, but as showed by the above table, this difference is neglectable either in absolute and percentual terms.

This first quantitative comparison demonstrates the capability of the simulation code to faithfully reproduce the conditions created in the tunnel test reference case.

4.4.3. Pressure coefficient comparison

The pressure coefficient analysis represents the quantitative comparison needed to validate the CFD simulation. The pressure coefficient is defined as follow :

$$C_p = \frac{p - p_{ref}}{\frac{1}{2} \rho_{ref} V_{ref}^2}$$

Where:

- p is the pressure detected at a certain point
- $\rho_{ref}, p_{ref}, V_{ref}$ are the reference density, pressure and speed of the incoming freestream in the unperturbed condition.

Therefore, to compute the pressure coefficient, the reference values of pressure, velocity, and density shall be introduced in the pressure coefficient definition within STAR CCM+.

	Reference values
Pressure	535.65 Pa
Density	0.0287 kg/m ³
Velocity	743.6 m/s

The computation is possible through the STAR CCM+ monitor “ mean field function” which is able to compute the average of a field function, in this case the pressure coefficient, for all the points on which it has been calculated.

Considering the unsteady nature of the flowfield, the pressure coefficient varies over time. Indeed, to compute and compare the pressure coefficient between the simulation and reference data, a temporal average is needed. Therefore the pressure coefficient is sampled in each point of interest for each time step; then the average of the sampled values on each point is processed, and finally, the graph representing the C_p distribution over the body is plotted.

The pressure coefficient trends for the aftbody and the forebody are now reported. The expected result is a pressure profile similar to the reference cases, with values varying within the same range at the same points. This range of variation is introduced because even the validated codes are not perfectly superimposable but present slight differences in the numerical values of C_p , which however are very small in absolute terms.

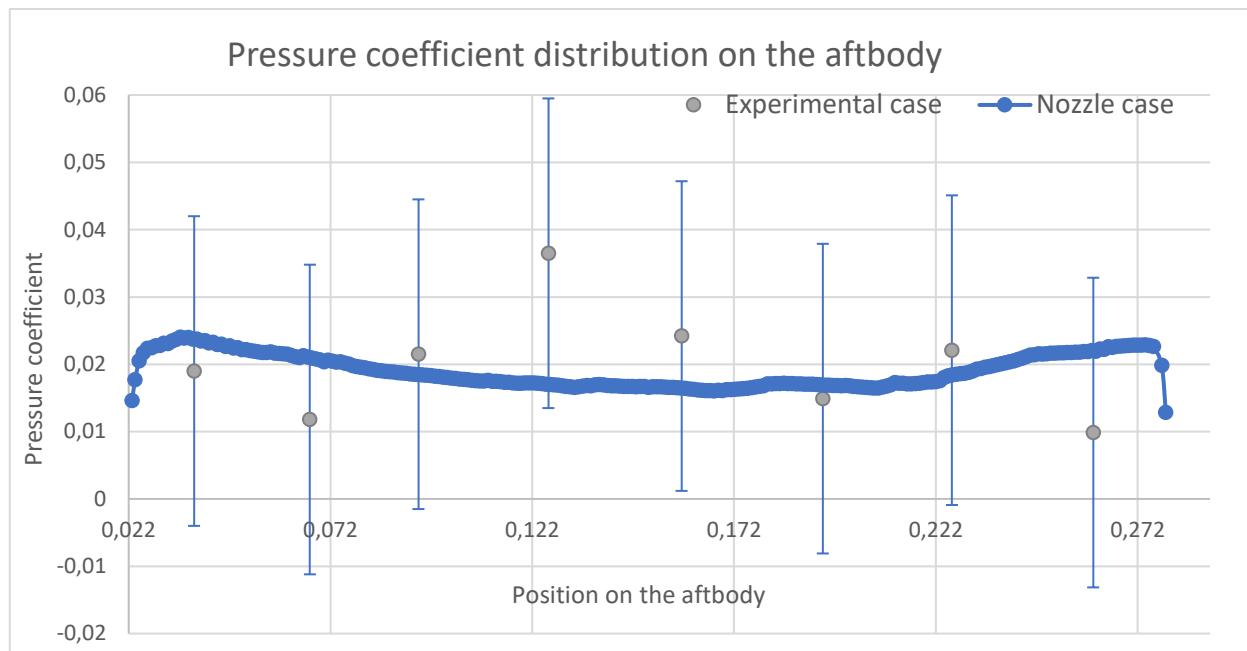


Figure 61--Aftbody averaged surface pressure coefficient distribution

The x-axis shows the position on the aftbody with respect to the X coordinate of the local reference system, indeed the beginning of the aftbody is set to 0.022 m.

The curve starts with a local minimum which is observable in the left part of the graph corresponding to the beginning of the aftbody near the junction with the forebody; this minimum value is around 0.015, as predicted by the test reference case and the other validated codes. Subsequently, the positive slope of the line indicates that the coefficient is growing. Indeed at 0.04 m there's a local maximum value around 0.023. Then the coefficient remains almost constant for the whole length of the body with slight fluctuations around the value of 0.02. This trend reflects the experimental data, where C_p is also constant around the value of 0.02. Finally, in correspondence of the end of the aftbody is remarkable the presence of a zone of strong C_p reduction, that starting from 0.02 decreases up to values of -0.015. Moreover, this zone is even notable in the pressure coefficient trend of the validated NASA codes.

In conclusion the aftbody averaged surface pressure coefficient distribution is perfectly aligned with the CFD validated codes predictions, and the coefficient values are contained within the variation range predicted by the test reference case, as showed in the above figure.

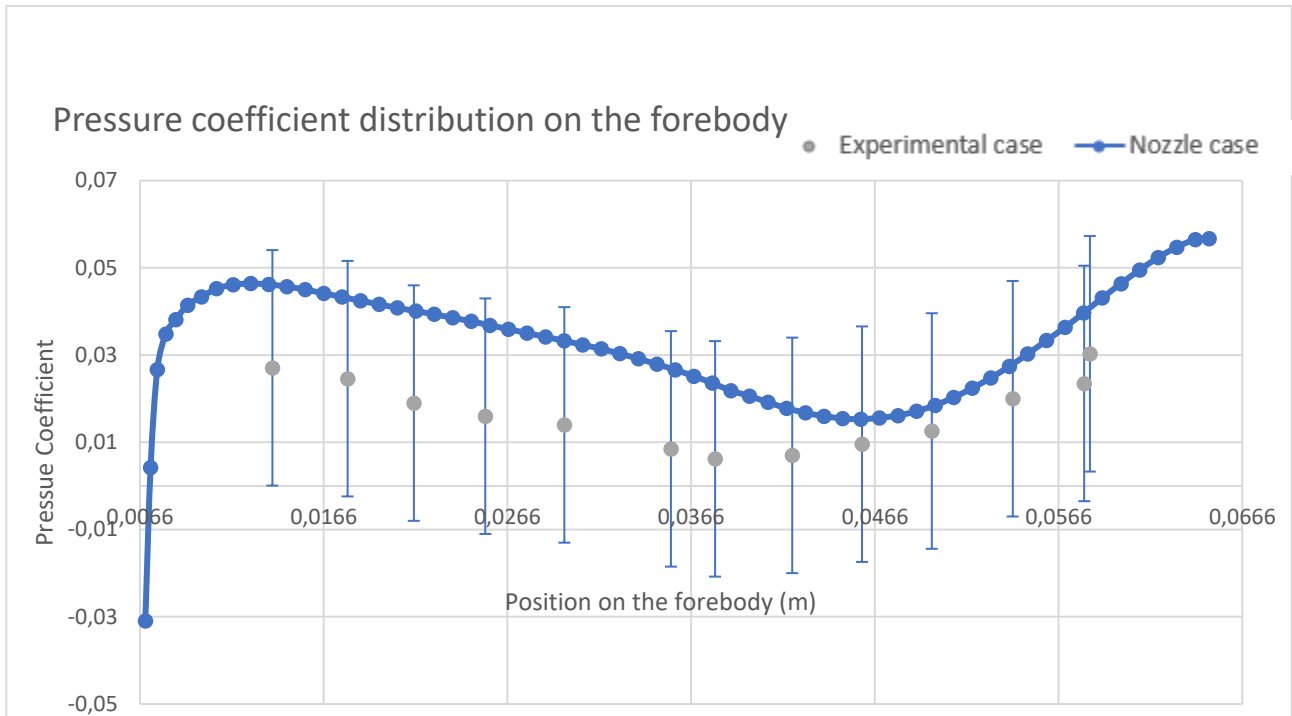


Figure 62-Forebody averaged surface pressure coefficient distribution

Concerning the values of the pressure coefficient at the forebody, the constant profile presented in the previous case is not here replied; values of the same magnitude order of the previous computation are obtained but a more marked variation of the coefficient is notable moving on the forebody surface.

The x-axis shows the position on the forebody with respect to the Y coordinate of the local systems, indeed the beginning of the forebody is set to 0.0066 m.

Really high-pressure values are computed at the beginning of the forebody due to the high pressure of the expanding jet which is felt near the nozzle exit, thus are not reported in the chart to avoid the modification of the representation scale of the coefficient.

Immediately afterward, as can be seen on the left side of the graph, there is a strong pressure reduction, which leads the C_p to negative values, around -0.03. This negative peak is also remarkable in the reference plots, where it varies between -0.25 and -0.05, depending on the considered code.

Subsequently there's a rapid increase of the C_p values: the line is distinguished by a remarkable positive slope. The coefficient achieves one of the two local maxima highlighted in the graph, around 0.045. The maximum is placed at 0.013 m, aligned with the position of the maximum in the reference data, where is comprised between the 10-20 percent of the length of the forebody and its value oscillates between 0.2 and 0.45, depending on the adopted code.

Then, the curve decreases progressively until it reaches a minimum value located at 0.046 m. This point is characterized by a pressure coefficient value of 0.015 and concavity upwards. This minimum point is aligned with the reference data prediction, which located the minimum between the 60-70% of the forebody length and described its value varying between 0 and 0.18.

Finally, the last part of the chart shows an increase in the pressure coefficient until it reaches the second local maximum, at 0.061 m with 0.054.

To the end of the plot, there is a reduction of the coefficient, to assure a continuous profile with the values of the aftbody. This trend is remarkable in the pressure coefficient of the rounded junction, that connects the two bodies and represents the final part of the forebody. However, considering the very small size of the joint, its pressure coefficient plot will not be reported here.

Moreover, the pressure coefficient values on the forebody are contained within the range predicted by the test reference case, thus showing the ability of the code to correctly reproduce the experimental case.

The quantitative analysis of the average pressure coefficient distribution on the forebody and aftbody, has confirmed the simulation capability to properly reproduce the reference test case conditions and results. The comparison between the pressure coefficient distribution upon the body, shows results strongly aligned also to the already CFD validated codes in most of the considered body surface, with values varying within the same range at the same points.

In conclusion, given the excellent results obtained both from a qualitative and quantitative point of view, it can be considered that the simulation implemented has met the necessary requirements for validation and can therefore constitute a solid baseline for further analysis and simulations, i.e. changing the physics condition, simulating the 3D situations, substituting of the air as the exhaust gas, modelling the freestream with gases reproducing Martian atmosphere etc.

4.5.No nozzle case-set up

In order to decrease the number of points involved into the calculation domain, ease the computational cost, and reduce the computational complexity, a simplified simulation has been carried out. In this simplified situation, the jet exhausting into the supersonic freestream expands directly from the nozzle exit, thus the internal expansion, starting from the reservoir and proceeding to the nozzle exit, is replaced with the substitution of the jet exit condition at the nozzle exit section. The removal of the jet expansion inside the convergent-divergent nozzle is possible through the calculation of the jet exhausting condition at the end of this internal expansion.

4.5.1. Geometry

The only difference with the previous simulations relies on the elimination of the nozzle. The nozzle wall divergent, nozzle wall convergent, nozzle wall throat, reservoir, wall reservoir, nozzle convergent joint are substituted by the creation of the nozzle exit section: a straight line from the end of the capsule conic wall until the symmetry axis. The nozzle exit is represented in the following picture with its length set to 0.00635cm.

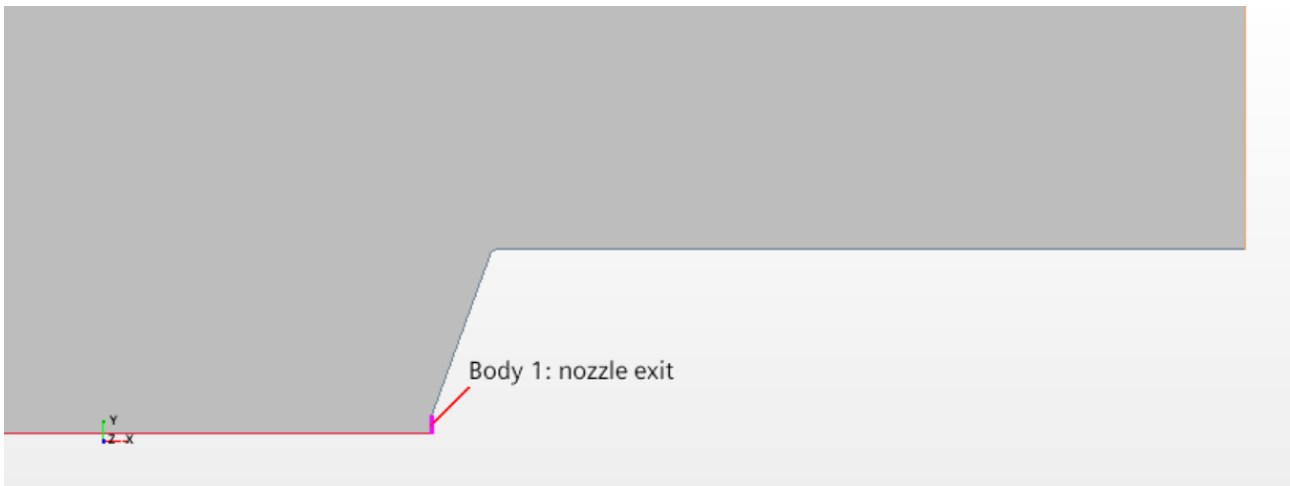


Figure 63-Nozzle exit instead of the convergent-divergent nozzle

The nozzle elimination leads to a reduction of the total number of cells, vertices and faces, in the mesh computation, summarized by the following table.

Table 18-Number of cells, vertices, and faces

	Nozzle simulation	No nozzle simulation
Number of total cells	189910	183345
Number of total interior faces	560134	545222
Number of total vertices	362021	362964

4.5.2. Difference with the previous simulation

The only variation with the previous case in the pre-processing resides in the setup of the boundary condition at the nozzle exit: this boundary is now model as a stagnation inlet, and characterized by total jet pressure, total jet temperature, and supersonic exit pressure. Hence, mesh set up, solvers adopted,

physics models adopted, and the other boundary conditions are unaltered with respect to the previous case. It is important to underline how the mesh refinement should be aligned to the comparison case: indeed, changing the grid resolutions will lead to different solutions output.

To compare the no-nozzle situation with the nozzle condition, three different points have been selected, which are collocated in three relevant regions of the flowfield. For each point the average values and the variation over time of pressure, Mach number, and temperature are compared: with these three field parameters it is possible to obtain the other field functions, and hence they're representative of the whole flowfield.

Point 2, belongs to the supersonic region, where the jet expands at supersonic speed; therefore, due to the inability of any disturbance to ascend the supersonic region, this portion of the flowfield is quite steady, and not influenced by the unsteadiness of the triple point. The convergence of field parameters in this region, represents the convergence of the steady state of the solution.

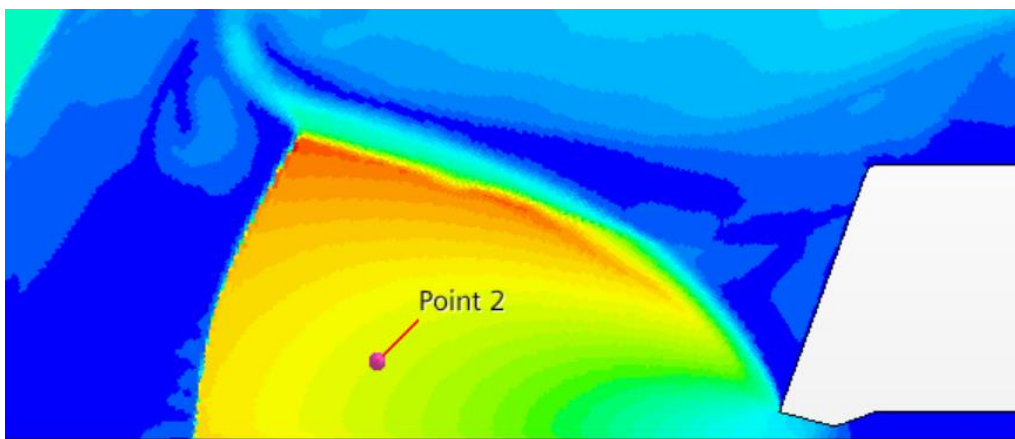


Figure 64-point 2, nozzle case simulation

Points 3 and 4 are located in subsonic regions. Point 4 is collocated along with the capsule conic wall near the capsule corner. This location has been selected for three main reasons:

- Proximity to recirculation subsonic region ;
- Proximity to the shear layer above the jet plume;
- Positioning on the body allows intercepting the disturbance generated by the pressure waves originated in the triple point which reflects off the body surface.

In addition to the comparison between the field parameters in this probe point in order to verify the no-nozzle situation, point 4 is also useful to implement a frequencies analysis aimed to describe the fundamental peak frequencies related to the propagation of the pressure waves generated in the triple point along the subsonic region, and reflecting off the body. For instance, the behavior of pressure values in this probe point is plotted over time, and frequency analysis is implemented exploiting this plot

Point 3 is also located in another subsonic region, between the bow shock and the Mach disk. The subsonic nature of this region allows the backward propagation of pressure wave originated in the triple point, but the complexity generated by the interaction of the freestream propagating downstream the bow shock, the jet flow slowing down behind the Mach disk, and the pressure wave propagating backward, prevents the application of dynamic frequency analysis upon this probe point. However the comparison between field quantities assesses that the simplified simulation doesn't affect the validated solution in the considered region.

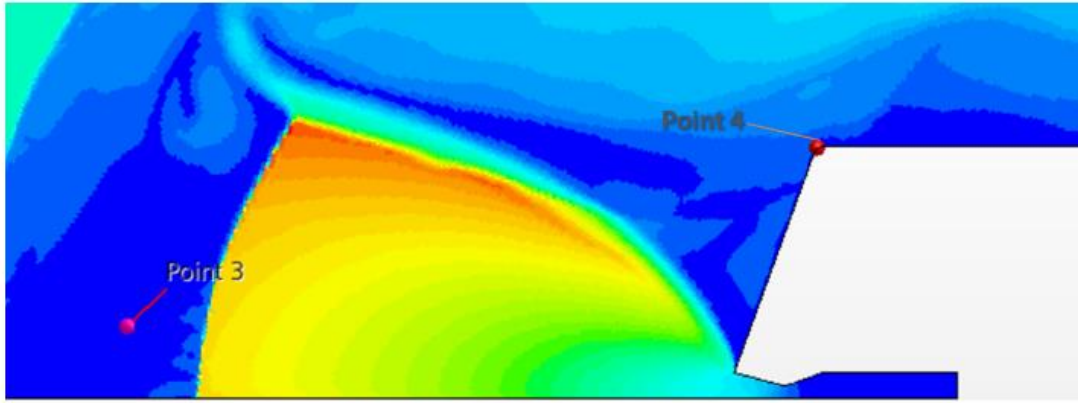


Figure 65-point 3 on the bottom left and point 4 upon the body corner, no nozzle case

4.5.3. Calculation of the nozzle exit condition.

Some assumptions shall be done to set the stagnation inlet conditions. In particular, considering an isentropic expansion where the total temperature and pressure are preserved, the parameter useful to compute the other quantities is the Mach number.

An isentropic flow, as defined, both in the compressible regime and not, could be described by the following equation that binds total pressure to exhaust section pressure:

$$p^o = p_e \left(1 + \frac{\gamma-1}{2} M_e^2 \right)^{\frac{\gamma}{\gamma-1}}$$

Where p^o , is the total pressure, M_e , is the exit mach number and p_e is the supersonic exit pressure.

The computation of the Mach exit number requires other assumption in addition to the isentropic propagation hypothesis :

- during the jet expansion in the convergent-divergent nozzle the viscous dissipation losses are neglectable;
- during the jet expansion in the convergent-divergent nozzle the losses derived from the nozzle divergence are neglectable;
- during the jet expansion in the convergent-divergent nozzle no heat phenomena are considered : a thermal equilibrium situation is established;
- a choking throat condition is established : the flow accelerates in the convergent part of the nozzle until achieving sonic condition in correspondence of the throat section, hence the mass flow rate achieves the maximum values and then is maintained constant during the whole evolution in the divergent part of the nozzle. Moreover, the flow continues to accelerate in the divergent part of the nozzle, ensuring supersonic condition in correspondence of the nozzle exit.
- absence of velocity gradients in the direction normal to the motion during the jet propagation in the convergent-divergent;

Through these hypotheses is possible to calculate the Mach exit number, considering the conservation of the mass flow rate between the throat section and exit section and using a 1 D formulation.

The first step in the computation is representing the mass flow rate as a function of the Mach number.

$$\dot{m} = \frac{p^0 A_{ref}}{\sqrt{RT^0}} f(M)$$

Where

$$f(M) = \sqrt{\frac{\gamma M^2}{\left(1 + \frac{(\gamma - 1)M^2}{2}\right)^{\frac{\gamma+1}{\gamma-1}}}}$$

γ is the gas constant, and A_{ref} is the reference area corresponding to the section where the mass flow rate is computed.

Accordingly to the conservation of the mass flow rate between the sonic throat and the exit section, the following equation is derived:

$$\frac{p^0 A_{throat}}{\sqrt{RT^0}} f(M = 1) = \frac{p^0 A_{exit}}{\sqrt{RT^0}} f(Me)$$

Where the first term represents the mass flow rate computed in the throat sonic section, and the right term represents the mass flow rate computed at the exit section, where the exit Mach number is achieved through the nozzle expansion.

Taking into account the isentropic hypothesis, the total pressure and total temperature remain unchanged between the two sections. Moreover, in the sonic throat section, the Mach number is known, and the Mach function assumes the following value:

$$f(M = 1) = \sqrt{\frac{\gamma}{\left(1 + \frac{(\gamma - 1)}{2}\right)^{\frac{\gamma+1}{\gamma-1}}}} = 0.6847$$

Thus, by simplifying the conservation equation, it is possible to derive a nonlinear equation.

$$f(Me) = \frac{1}{\varepsilon} f(M = 1)$$

The right terms of the equation are known, and the non-linearity resides in the definition of the Mach function.

This nonlinear equation presents two different solutions, one in subsonic region and the other one in supersonic region, corresponding to the two physical possible situations of an expanding jet into a convergent-divergent nozzle.

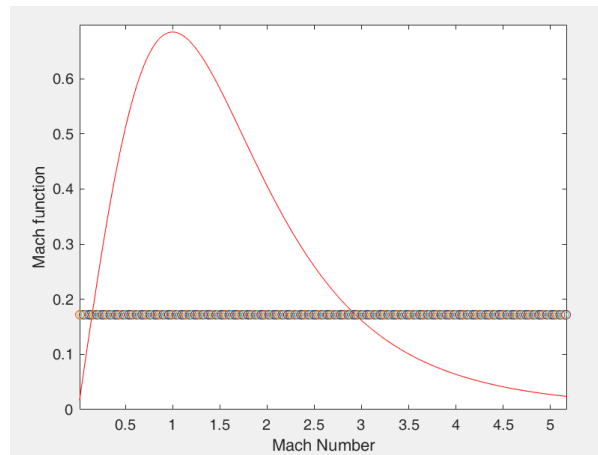


Figure 66-Mach function and graphical representation of the solution of the nonlinear equation

A more accurate solution is furnished by a numerical method able to solve non-linear equations. Given the simplicity of the equation, the Newton Bisection Method has been applied: this method is aimed at identifying the roots of the equation obtained by placing the Mach function minus the constant term equal to zero. For the definition of the boundary conditions of the method, a tolerance of $10e-6$ has been adopted, coupled with the extremes of the calculation range of the root set to $M=1$, and $M=5$, also thanks to the previous graphic solution. The convergence has been obtained after only 21 iterations, and the Mach computed is aligned with the graphic solution.

```

constant=1/4.*((1.4.*(2./(2.4)).^(2.4./0.4)).^(0.5));
f=inline(' sqrt( (1.4.*x.^2)./((1+0.2.*x.^2).^(2.4./0.4)) )-0.1712 ');
x=linspace(0,20,1000);
Mach=f(x);
plot(x,Mach);
toll= 10e-07;

a=1;
b=5;
cont =0;
if f(a)*f(b)<0
    err=abs(b-a);
    while err>toll
        z=(a+b)/2;
        if f(a)*f(z)<0
            b=z;
        else
            a=z;
        end
        cont=cont+1;
        err=abs(a-b);
    end
end
end

```

Figure 67-MATLAB computation of the Newton Bisection Method

In conclusion, the Mach exit value has been calculated equal to 2.94

Once identified the Mach exit number, is possible to compute the so-called supersonic exit pressure with the relation valid for isentropic flow.

The stagnation inlet conditions are so summarized in the following table:

Total Pressure	Total temperature	Supersonic exit pressure
4137636.06 Pa	347.14 K	123250 Pa

4.6. Results -No nozzle case

4.6.1. Comparison of the field parameters

The starting point for the analysis of the results is considering that the no-nozzle simulation has been implemented from a validated code which has demonstrated the achievement of a stable solution, is numerically stable and doesn't present any critical issues: so, the starting conditions of the new simulations are dictated by the results obtained from the previous simulation. Modifying the boundary condition while running a simulation, normally leads to a transient period under which variables are changing over time in consequence of the variation. Indeed, even if the computed condition at the nozzle exit shall reproduce the same conditions related to the nozzle presence, some slight variations occur, related to the set of considered assumptions earlier depicted and to the adaptation to the newly imposed boundary condition. Following the transient period, convergence toward a stationary state is expected for the flowfield regions not affected by unsteadiness, while convergence toward the same average values is expected for the unsteady flowfield parts.

Is important to discern between the comparison of steady regions and unsteady ones. Indeed, while for a steady situation the parameter values are independent of the physical time of the simulation, for the unsteady regions the parameters variate over time. To correctly compare the no-nozzle situation with the nozzle case, the simulations shall run at the same physical time. However though this condition is implemented, the presence of a transient event prevents the perfect superimposition of the temporal trends of the quantities, thus preventing the comparison only from a graphical point of view. Along with the graphic correlation, it is necessary therefore a temporal average of the quantities, calculated on the same number of iterations and starting from the same physical time of the solution.

Moreover, the analysis of flowfield parameters is computed upon 40000 iterations for the unsteady supposed regions. The choice of this value is related to the fundamental frequency of the unsteady phenomena, around 2 kHz. Indeed, is possible to compute the physical time related to the unsteadiness, inverting the unsteady frequency, and elaborate a minimum number of iterations aimed to capture the unsteadiness. For the selected case, the computed physical time is $5 \cdot 10^{-4}$ seconds, which means that during this time an entire cycle of field unsteady parameter is completed. Remembering the time step adopted for the simulation, 10^{-6} , the number of iterations is estimated dividing the physical time and the time step. Hence, considering the inner iterations adopted for solving the differential equation, the minimum number of iteration able to capture the unsteadiness is 5000. Therefore, 40000 iterations, approximately 8 variations cycle, represent a good compromise among the time needed for catching the unsteady evolution of the flowfield and the computational cost, which grows proportionally to the number of iterations.

Concerning the steady regions of the flowfield, the computation and comparison of the parameters have been realized upon 20000 iterations. Indeed, this number, corresponding to $2 \cdot 10^{-3}$ seconds, has been considered large enough to capture the transient event and to allow the convergence to a steady state. Once the convergence towards a stationary state solution has been achieved, continuing to iterate would only have been a waste of calculation time.

For each probe point the trends of the quantities over time and the time averages are reported, both for the nozzle and no-nozzle case.

Point 2, supersonic region inside the jet plume

No-nozzle case

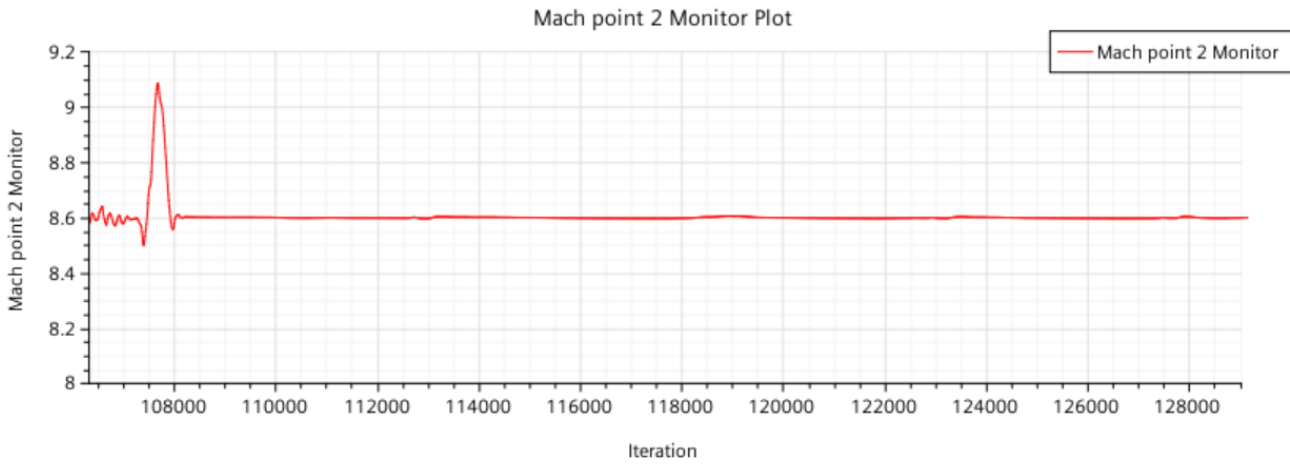


Figure 68-No nozzle simulation, point 2 Mach number over 20000 iterations

Nozzle-case

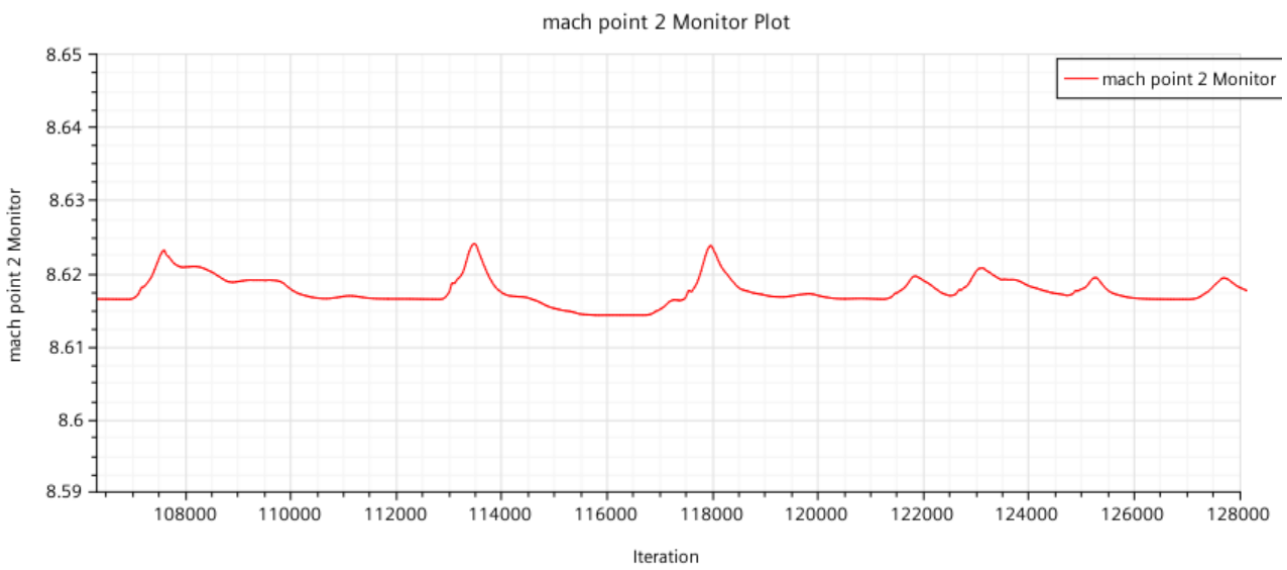


Figure 69-Nozzle simulation, point 2 Mach number over 20000 iterations

Table 19-Point 2 Mach number averages for both iterations

No nozzle	Nozzle
8.60	8.61
percentage difference between the two simulations	0.1%

No nozzle case

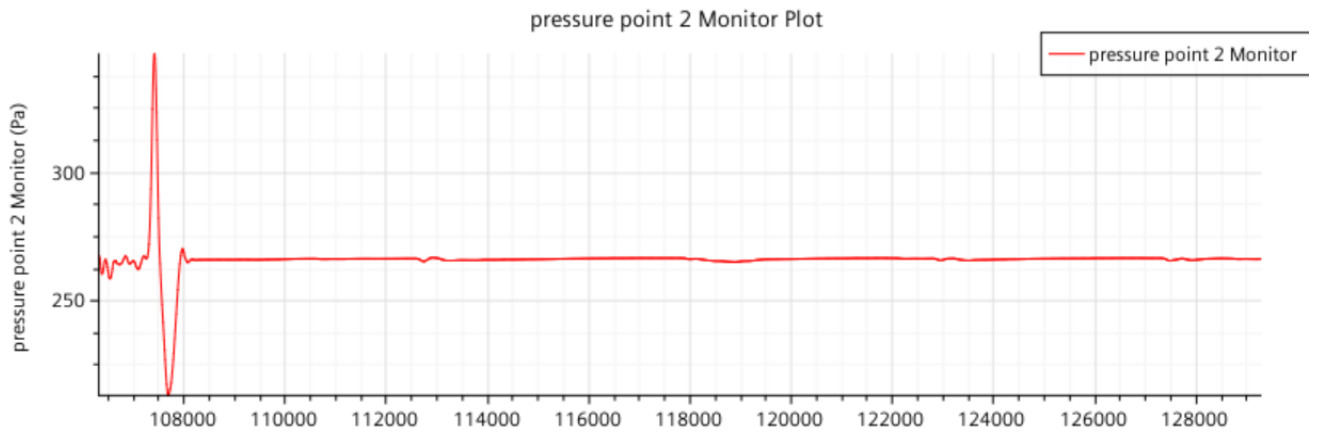


Figure 70-No nozzle simulation, point 2 pressure over 20000 iterations

Nozzle case

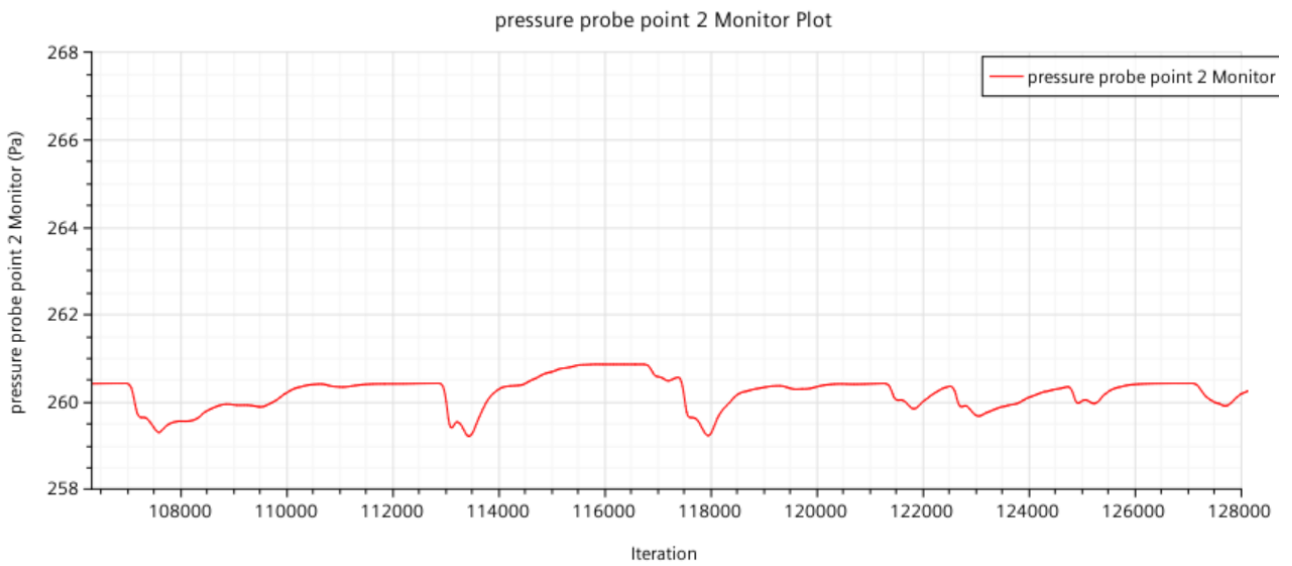


Figure 71-Nozzle simulation, point 2 pressure over 20000 iterations

Table 20-Point 2 pressure averages for both simulations

No-nozzle	Nozzle
265.81 Pa	260.12 Pa
Percentage difference between the two simulations	2%

No nozzle case

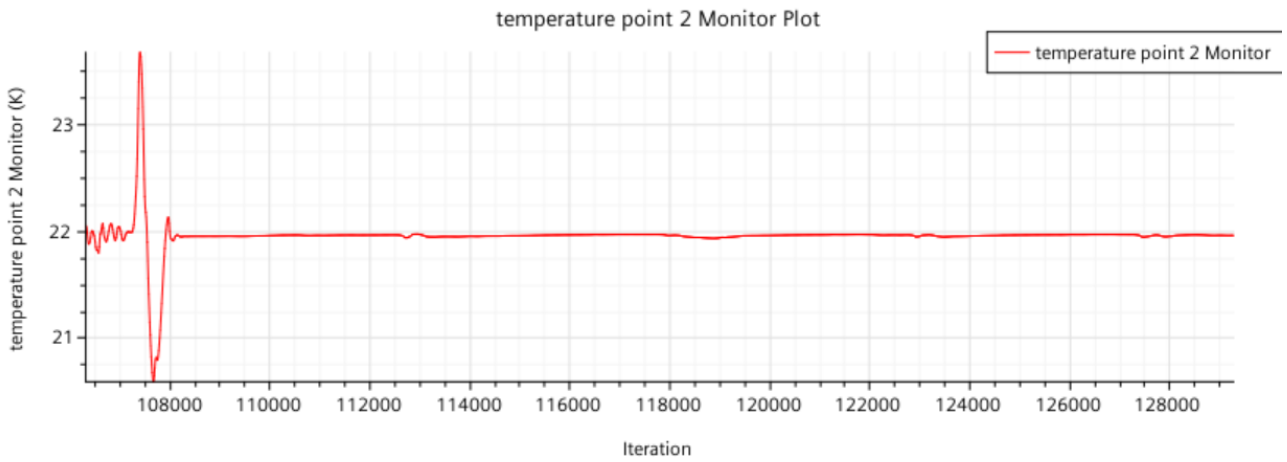


Figure 72-No nozzle case, point 2 temperature over 20000 iterations

Nozzle case

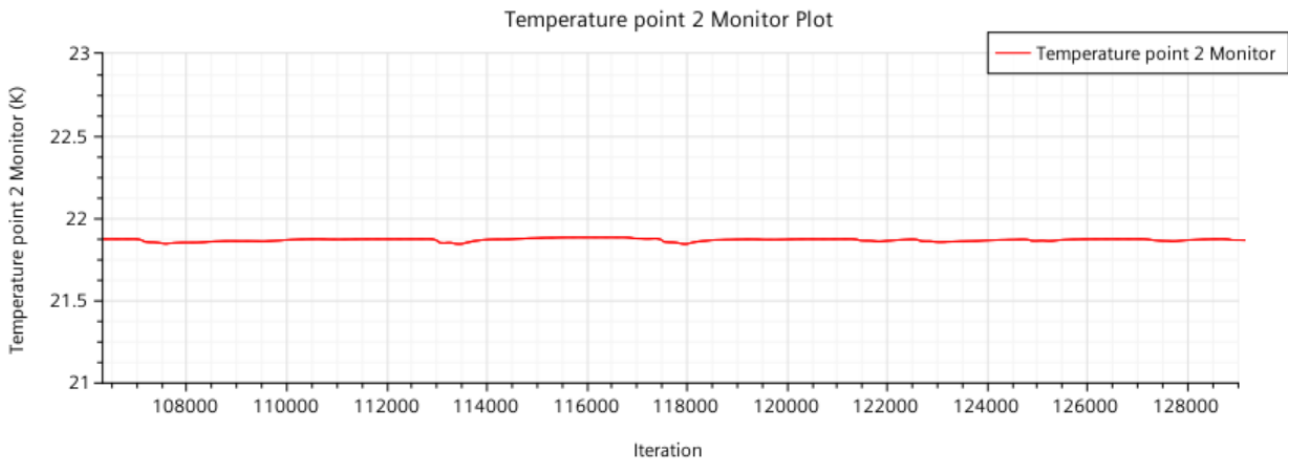


Figure 73-Nozzle case, point 2 temperature over 20000 iterations

Table 21-point 2 temperature averages for both simulations

No-nozzle	Nozzle
21.95 Kelvin	21.86 Kelvin
Percentage difference between the two simulations	0.4%

The analysis of the flowfield parameters in the point 2 confirms the steady state assumptions regarding this supersonic region : the inability of any disturbances to ascend the supersonic region results in a quasi-steady flowfield where the field parameters are independent of time and oscillate very slightly around their average values . Is also remarkable the presence of the transient event for the no nozzle case , represented as a strong variations of the field parameters among time. Is possible to quantify the physical time associated with this event : indeed considering the starting iteration set to 106000, the field values converge to the steady state value approximately after 2000 iterations. Taking into account that every 10 iterations constitute a time step of $10e-6$ s, a physical time of $2 \times 10e-4$ s is calculated.

Subsequently to the transition event, is visible that all parameters converge towards the same values calculated with the simulation presenting the nozzle, as graphically demonstrated and confirmed from the calculation of difference percentage of the time-average of such values.

From this analysis it is clear that the nozzle replacement with the expansion conditions applied on the exit section, doesn't affect the flowfield downstream the nozzle, and so the characteristics of the exhausting jet.

Point 4 , subsonic region on the body

No nozzle case

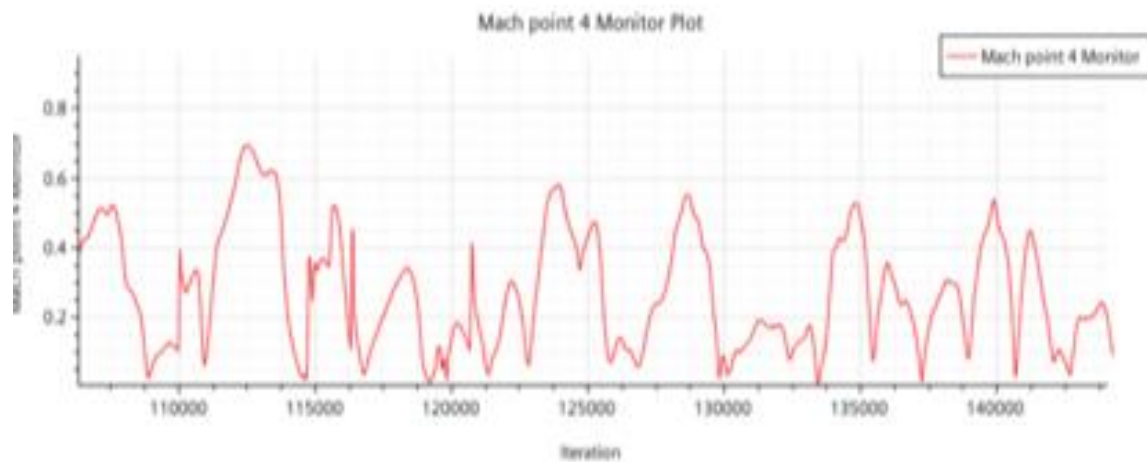


Figure 74-No nozzle case, point 4 Mach number over 40000 iterations

Nozzle case

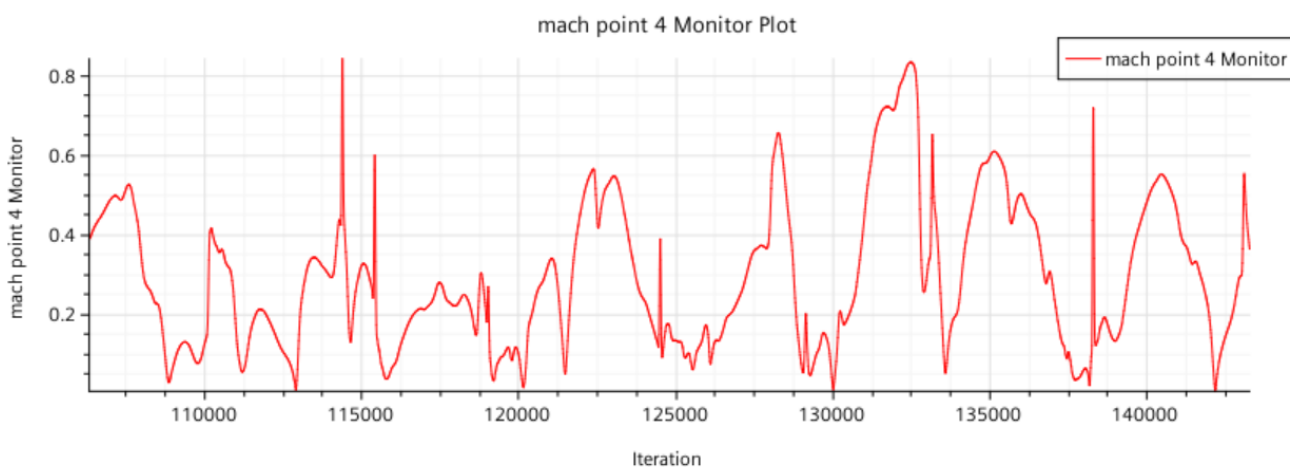


Figure 75-Nozzle case, point 4 Mach number over 40000 iterations

Table 22-Point 4 Mach number averages for both iterations

No nozzle	Nozzle
0.2703	0.2905
percentage difference between the two simulations	6.2%

No nozzle case

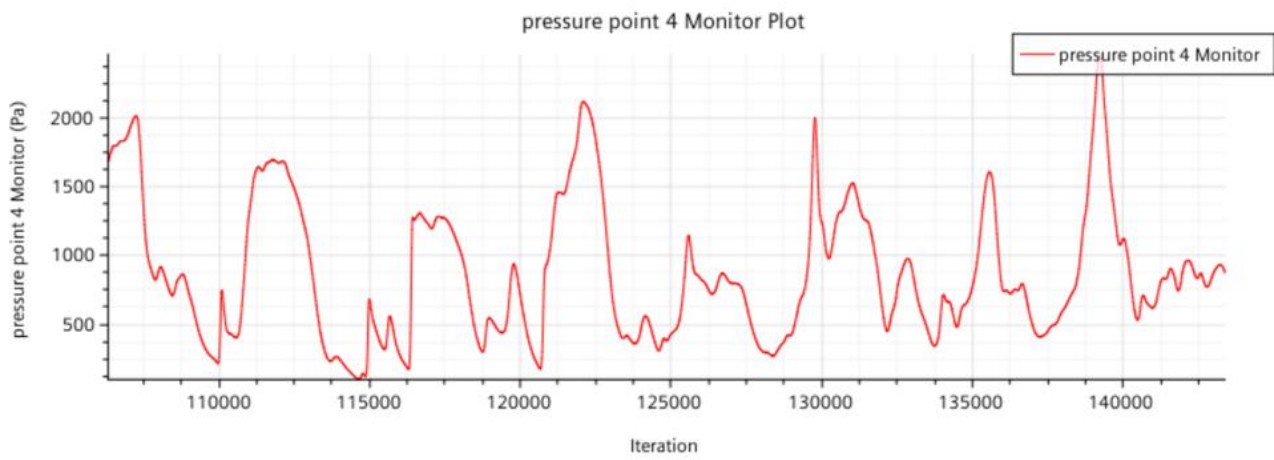


Figure 76-No nozzle simulation, point 4 pressure over 40000 iterations

Nozzle case

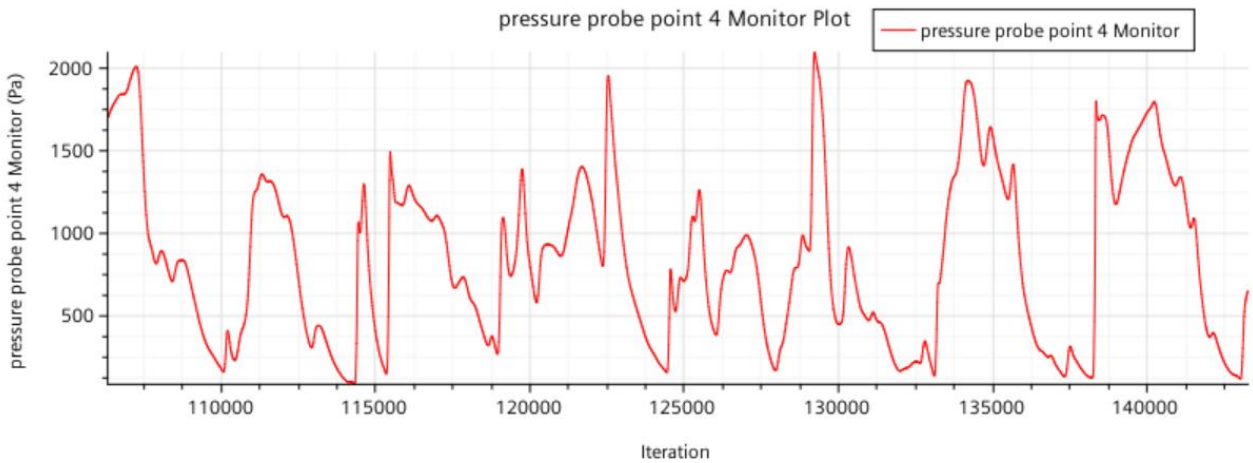


Figure 77-Nozzle simulation, point 4 pressure over 40000 iterations

Table 23-Point 4 pressure averages for both simulations

No-nozzle	Nozzle
866.77 Pa	838.22 Pa
percentage difference between the two simulations	3.4%

No nozzle case

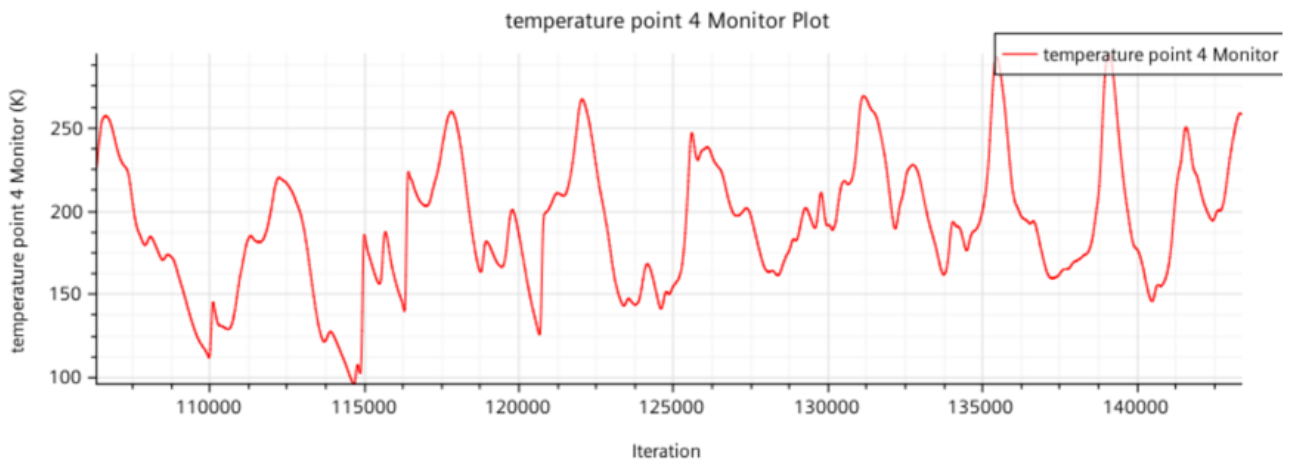


Figure 78-No Nozzle case, point 4 temperature over 40000 iterations

Nozzle case

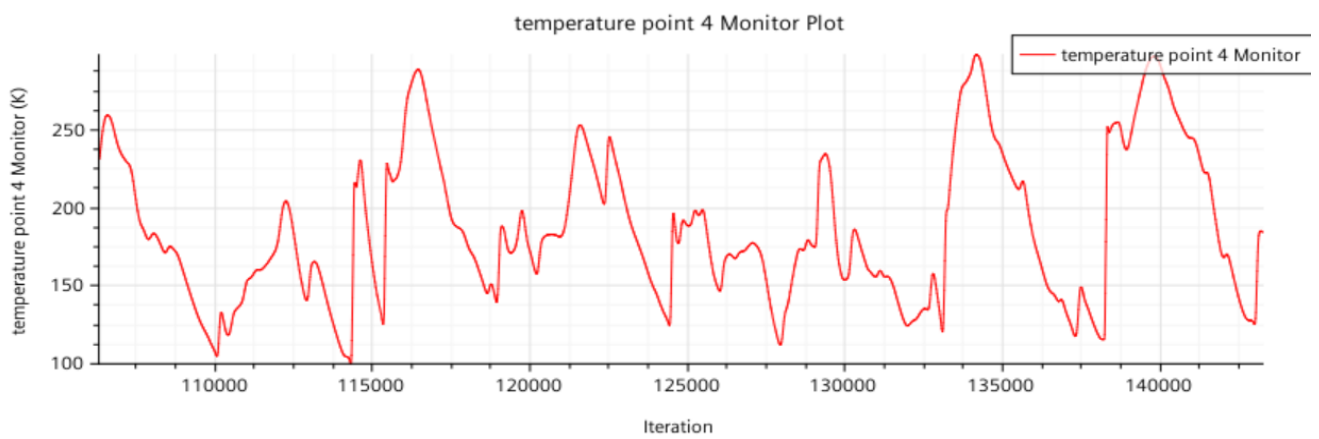


Figure 79-Nozzle case, point 4 temperature over 40000 iterations

Table 24-point 4 temperature averages for both simulations

No-nozzle	Nozzle
191.20 Kelvin	185.67 Kelvin

Percentage difference between the two simulations	2.9%
---	------

Also in this situation the transient event related to the variation of boundary conditions runs out soon; however, the presence of the transient event causes a shift in the physical time among this simulation and the validated one: even if the starting time is the same, the presence of the transient event prevents that the no-nozzle case refers to the same physical time of the nozzle case. Therefore even if the parameters trends is similar between the two simulations, differences in peaks amplitude or in peaks locations are notable, especially as time passes. Indeed, in the first part of the iterations, the trends are more consistent than the last part, also index of the propagation of the time shift within the numerical solution.

However, the parameters variations occur within the same range either for pressure , temperature, and Mach and the average computed values are characterized by a slight percentage difference.

With a brief frequency analysis, the no-nozzle case preserves the main frequency of the nozzle case, which variates between 1.7-2.2 kHz, in accordance with the fundamental frequency computed in the test reference case. This also indicates that the strong parameters variations, especially in terms of pressure and temperature(up to 50 kelvin or up to 1000 Pascal), are related to the vortex shedding in the flowfield, originated by the triple point oscillations and then reflected off the body.

Point 3, subsonic region behind the bow shock

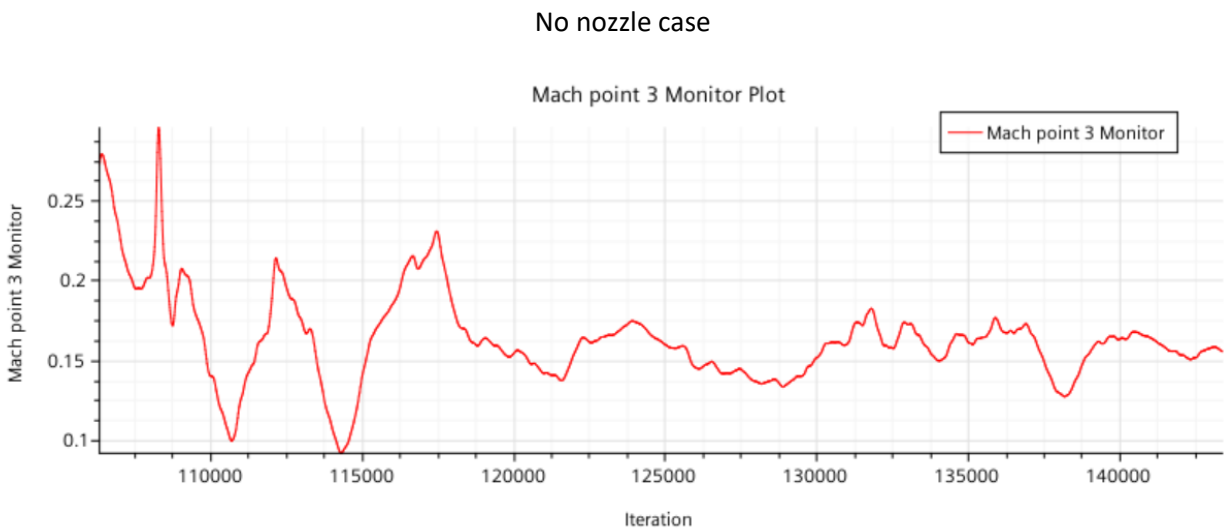


Figure 80-No nozzle case, point 3 Mach number over 40000 iterations

Nozzle Case

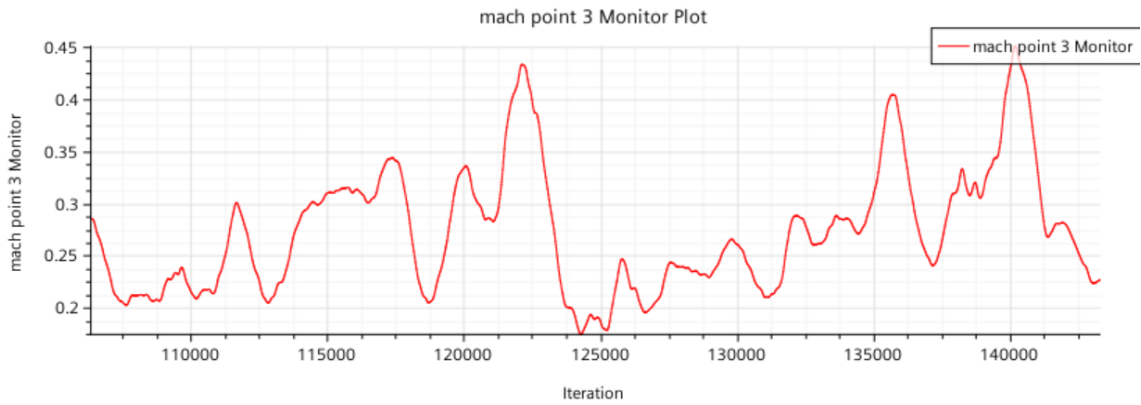


Figure 81-Nozzle case, point 3 Mach number over 40000 iterations

Table 25-Point 3 Mach number averages for both iterations

No nozzle	Nozzle
0.178	0.273
Error percentage between the two simulations	34.7%

No Nozzle case

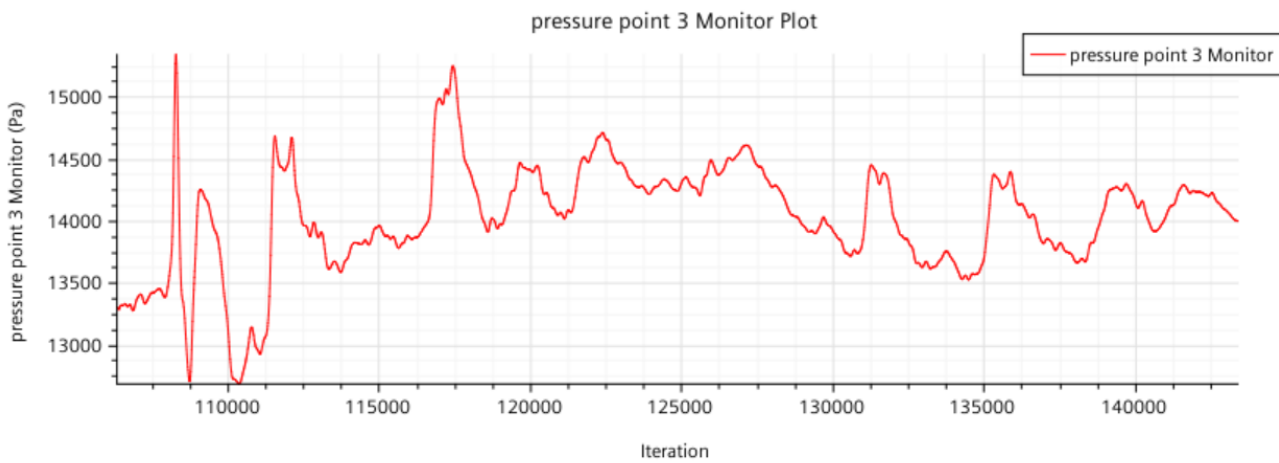


Figure 82-No nozzle case , point 3 pressure over 40000 iterations

Nozzle case

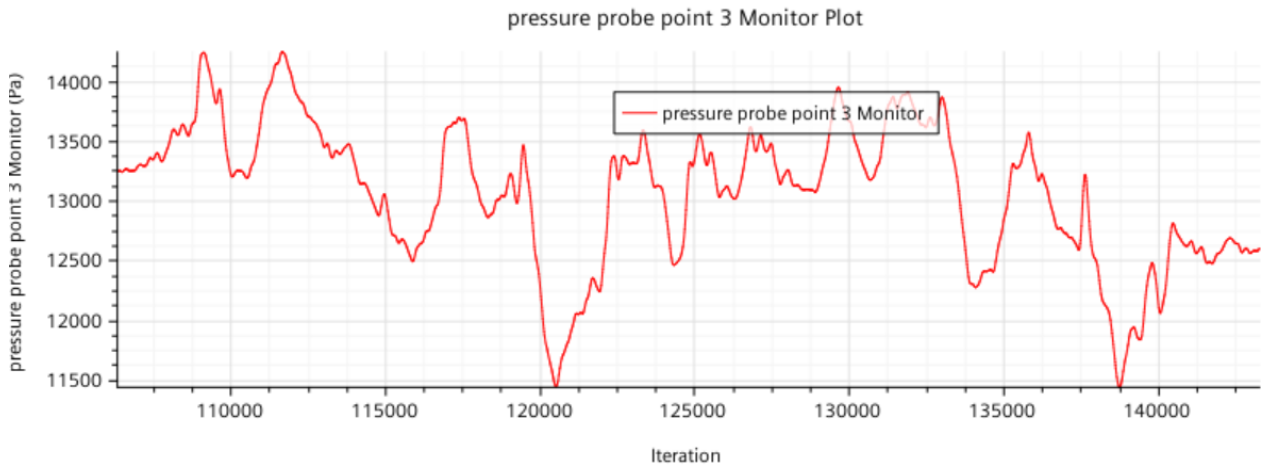


Figure 83-Nozzle case, point 3 pressure over 40000 iterations

Table 26-point 3 pressure averages for both simulations

No-nozzle	Nozzle
1402.10 Pa	1306.4 Pa
Error percentage between the two simulations	7.11%

No nozzle case

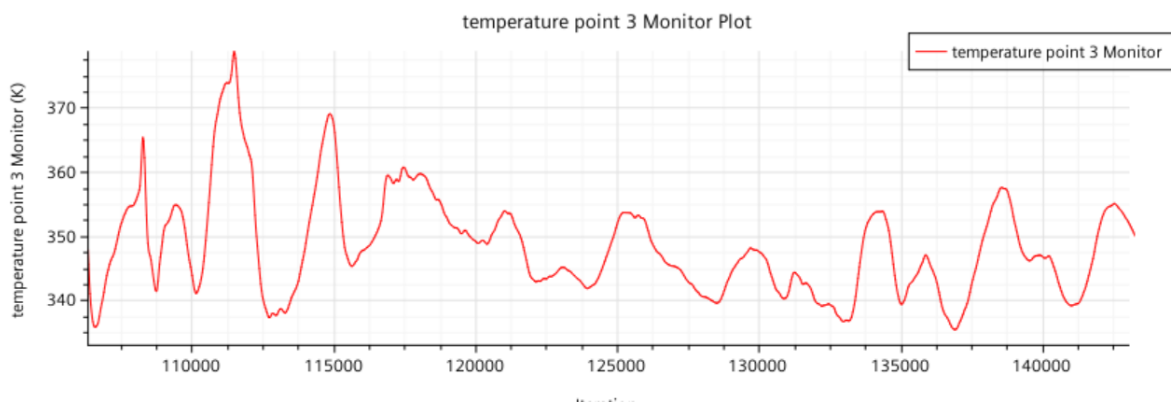


Figure 84-No nozzle case, point 3 temperature over 40000 iterations

Nozzle case

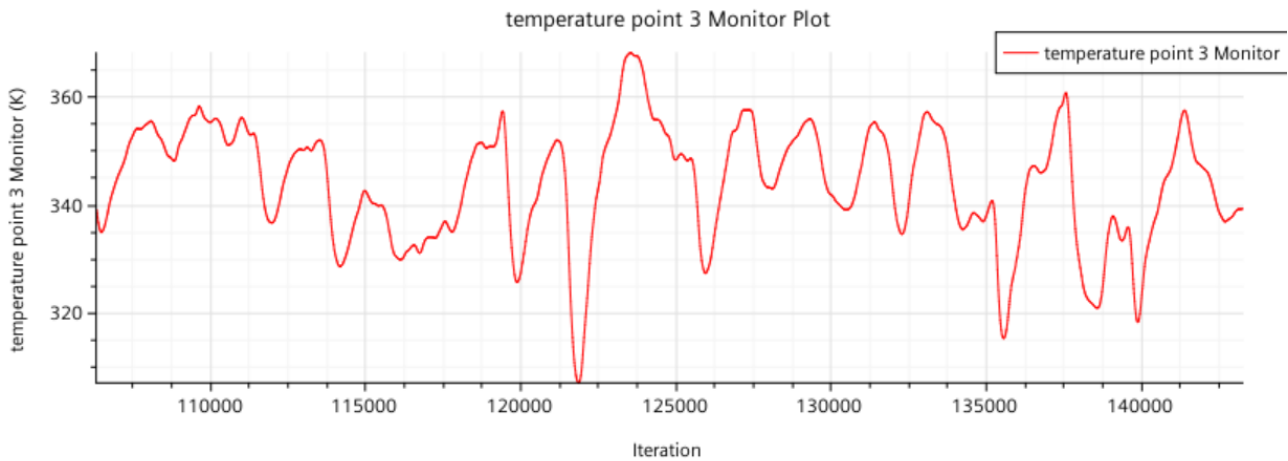


Figure 85-Nozzle case, point 3 temperature over 40000 iterations

Table 27- point 3 temperature averages for both simulations

No-nozzle	Nozzle
348.37 Kelvin	343.8 Kelvin
Error percentage between the two simulations	1.3%

Point 3 is involved in the stagnation region between the Mach disk and bow shock. This region is characterized by the contact surface produced by the interaction of the incoming freestream and exhausting jet. This region is also distinguished by the small oscillation of the bow shock and Mach disk, which coupled with the pressure wave generated by the triple point, increase the complexity of this flowfield portion: is impossible to characterize the unsteadiness presented in the stagnation region by a fundamental frequency, and so the unsteadiness there is defined irregular.

Thus, the comparison between the parameters of the no-nozzle and nozzle case becomes really complicated: the time shift effect related to the transient event is more amplified than the previous case. Though the agreement between the average values of temperature and pressure, with a low percentage difference, the Mach average value presents the highest difference reported. The discrepancy between the Mach number behaviour for the no-nozzle and the nozzle case may be related to the position of point 3 with respect to the stagnation point. The small reduction of the bow shock distance may have led to the displacement of the probe point 3 from the subsonic region behind the Mach disk, to the subsonic region behind the bow shock, thus causing a slight velocity variation. However, this result must be correctly contextualized: the difference, which is high in percentage, actually reflects a very low Mach number, which does not indicate a change in the phenomenology of the interested area among the two simulations.

In conclusion following the comparison of the numerical and graphical trends of the field parameters, the elimination of the jet expansion inside the nozzle doesn't affect the flowfield characteristics in the selected three points, which are representative of the three important regions of the SRP flowfield.

4.6.2. Mach isocontours -pressure and temperature isocontours – qualitative comparison

As for the validation of the first simulation, a qualitative analysis is implemented aimed to compare the pressure, temperature, and Mach number trends among the two simulations.

Even in this case, the analysis is computed by using images that refer to a precise solution time, i.e. 0.023 s. Indeed, it is impossible to investigate the unsteadiness through these images, and the frequency analysis is later computed.

Mach isocontours, temperature isocontours and pressure isocontours plots demonstrate the capability of the no-nozzle case to reproduce the main SRP flow features described by theoretical prediction and observed in the previous simulation: thus, the substitution of the jet expansion through the convergent-divergent with the jet exiting condition at the nozzle exit section doesn't affect the existence of the characteristic structures.

Indeed it is possible to locate through the frames :

- The bow shock;
- The Barrel shock and jet boundary;
- The Stagnation region ;
- Jet plume structure ;
- The Mach disk;
- The recirculation region ;
- The free shear layer near the jet boundary;
- The Triple point.

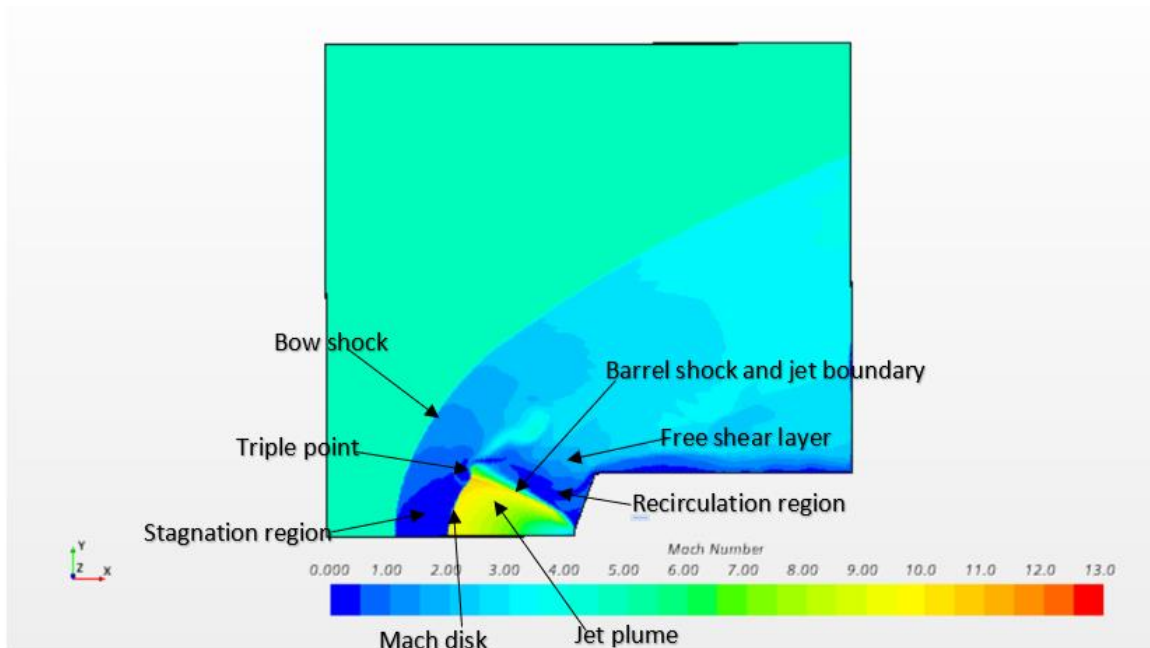


Figure 86-Mach isocontours scene with SRP flowfield main features, no-nozzle case

From the comparison of the isocontours plots between the two simulations emerges that the pressure, temperature, and Mach number variations occur within the same ranges and the quantities are characterized by the same values in the same points of the flowfield.

The Mach number assumes the higher values at the top of the jet (≈ 13), in the jet plume. Then is characterized by subsonic values in the stagnation region within the bow shock and Mach disk, and then by either supersonic and subsonic values at the shear layer above the jet boundary. A peculiarity in this Mach number scene with respect to the nozzle case, is the different pattern of the triple point: as far as the scene is elaborated for a different solution time, the triple point pattern is affected by its time dependency, and thus slightly differs from the previous case. Moreover, throughout the flowfield there are no strong differences within the colormap of the nozzle case, which represents the values from minimum to maximum, indicating that the Mach number variations occur within the same range in the same flowfield zone, making the two frames very similar but not superimposable, as far as are elaborated for different solution times.

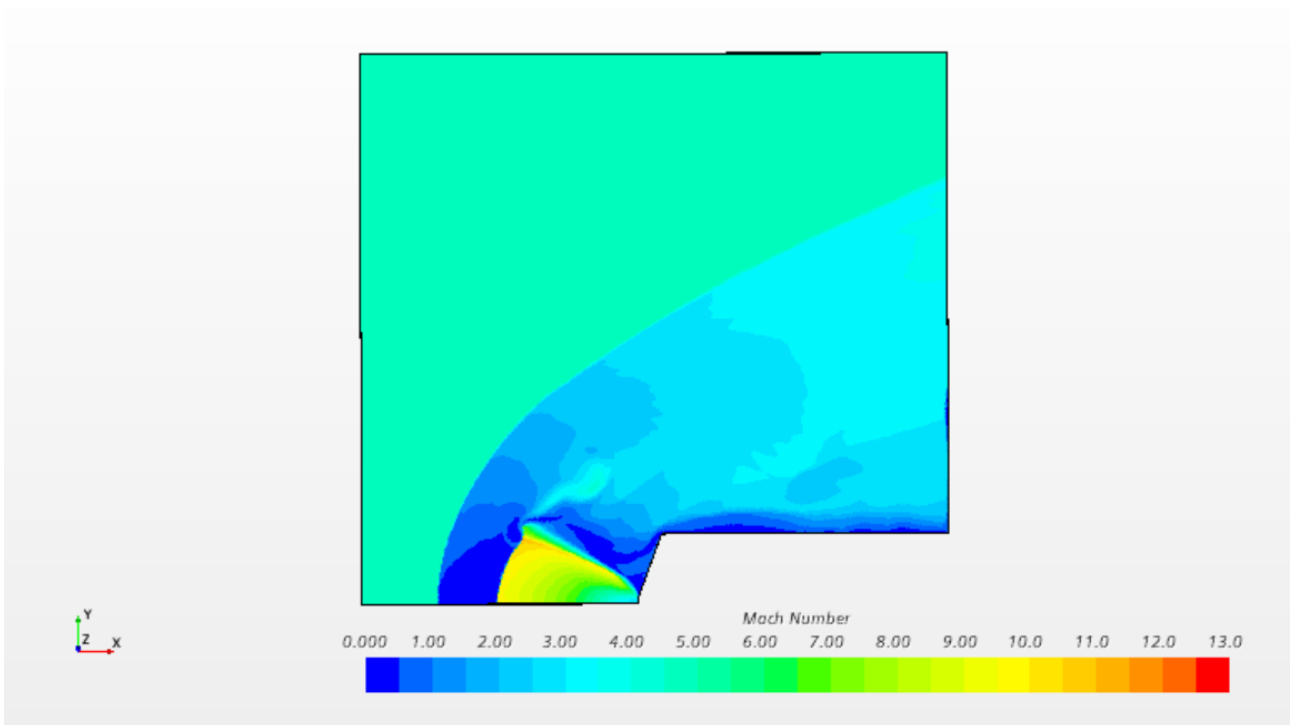


Figure 87-Mach isocontours scene for the no-nozzle simulation

The temperature profile has the minimum values at the expansion zone of the jet where the temperature reaches peaks of the order of ten degrees, therefore aligned with the minimum temperature values achieved in the same region by the nozzle case. Following the compression due to both the Mach disk and the bow shock, the temperature reaches its maximum values in the stagnation region. Even in this region the colormap shows agreement among the two simulations, either in term of colours utilised and quantitative values (≈ 350 K). However, a constant temperature profile envelope the forebody and the aftbody, with a temperature of ≈ 200 K.

A slight difference between the two temperature plots (no-nozzle and nozzle case) resides in the representation of the triple point, which appears less marked and less concaved in the no-nozzle case.

However, this is related to the strong oscillation behavior characterizing such point, and does not affect the good correspondence between the temperature ranges in the two simulations.

The existence of a temperature discontinuity (yellow straight line) above the jet boundary underlines the presence of the shear layer in that region : this contact surface is originated by the interaction of the freestream flow behind the bow shock and jet which is moving toward the aftbody. This region is characterized by the same pressure values and common direction of velocity, but by different velocity, temperature, and density magnitudes, depending on the previous evolution of the considered flow, either the exhausting jet and the freestream.

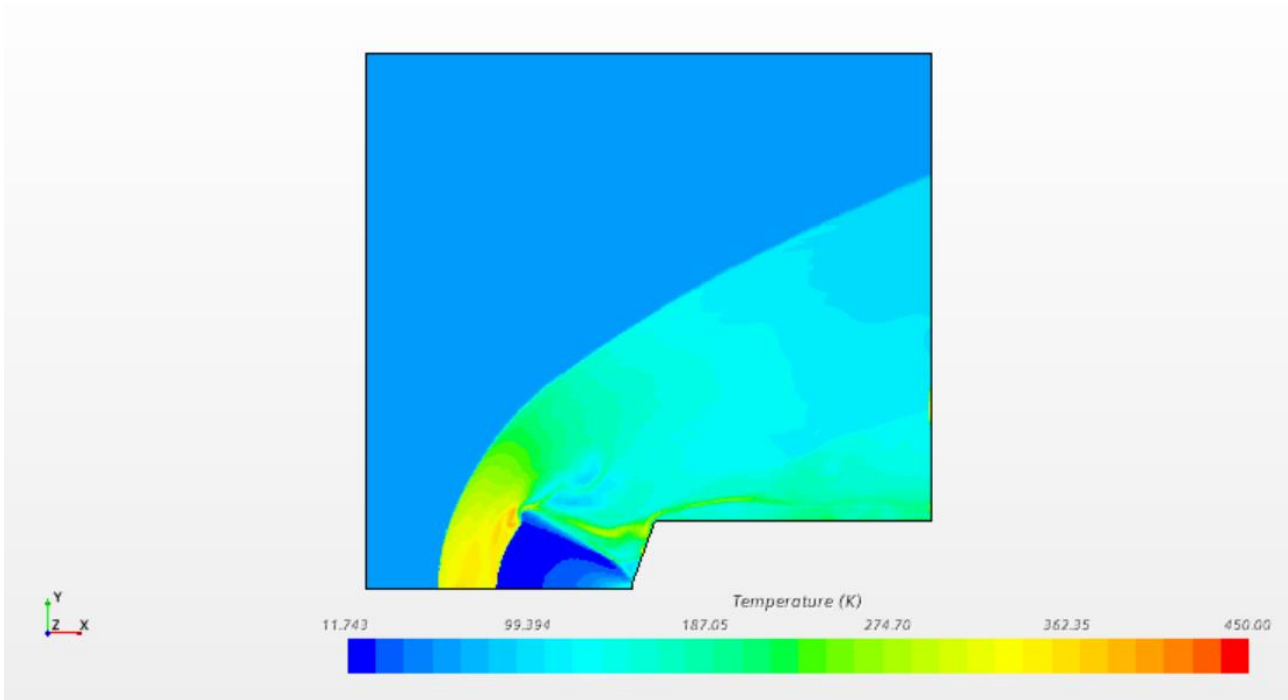


Figure 88-temperature isocontours scene for the no-nozzle simulation

The colormap of the pressure isocontours scene has been set to reproduce the pressure variations range of the nozzle case. The pressure scene has been the only scene which strongly differs in terms of range variations between the two simulations; adopting a colormap based on the maximum and minimum value for the pressure in the no-nozzle case, would have led a shift in the representation of the pressure field.

This shift is due to the displacement of the maximum pressure value towards lower values for the no nozzle case.

The maximum static pressure value is of course reduced passing from the nozzle case to the no-nozzle case. While the highest value for the nozzle case was the static pressure value in the reservoir, which coincided with the stagnation jet pressure in that quiescent condition, the maximum static pressure value in the no-nozzle case is the jet exit pressure, obtained from the isentropic relation and lower than the total jet pressure, due to the jet expansion condition. The difference in the maximum values between the two simulations is approximately one order of magnitude. Indeed, in this scene the pressure value corresponding to the stagnation condition of the nozzle case, has not been achieved at any point.

Beyond the maximum values, the pressure distribution in the flowfield presents the same trends as the nozzle simulation. There's a strong reduction in pressure during the jet expansion, indeed the minimum

pressure values are achieved at the end of the jet plume, before the Mach disk. (the magnitude order is ≈ 100 Pa). In the stagnation region between the Mach disk and bow shock, the pressure profile recovers high pressure values but still lower than the jet exit pressure, which represents the absolute maximum pressure for this case. Is also remarkable the constant pressure profile enveloping the body, as in the nozzle simulation, distinguished by values of the order of 800-1000 Pa. The contact surface previously depicted with the temperature isocontours scene can't be noticed in the pressure scene.

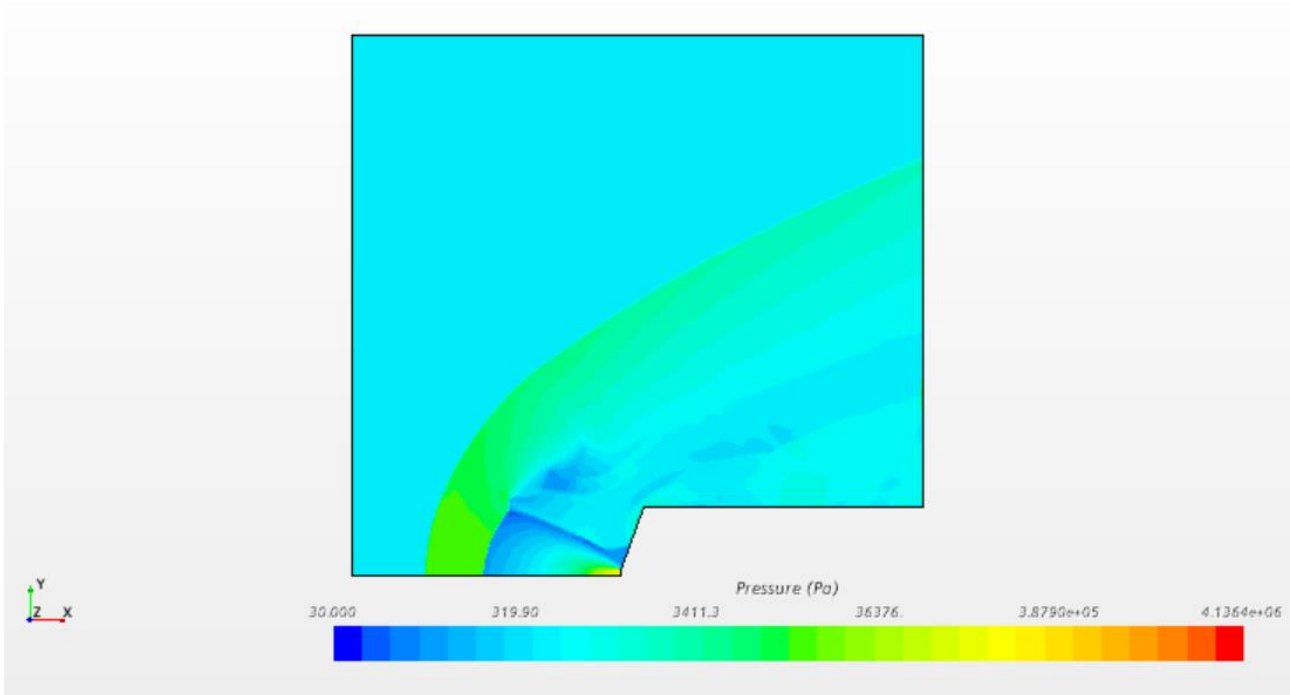


Figure 89-Pressure isocontours scene for the no nozzle simulation

Pseudo- Schlieren scene

In the pseudo-Schlieren scene elaborated for the no-nozzle case at the solution time set to 0.023s, all the main SRP features which cause density gradients have been represented. Furthermore, is remarkable the presence of the bow shock, Mach disk, jet barrel shock, subsonic shear layer, and supersonic/subsonic shear layer above the jet plume. Indeed the pseudo-Schlieren scene confirms the assumptions elaborated in the temperature isocontours scene regarding the shear layer above the jet plume: the succession of dark lines above the jet indicates the shear layer presence, where density gradients related to the interaction of two different flowfields occur.

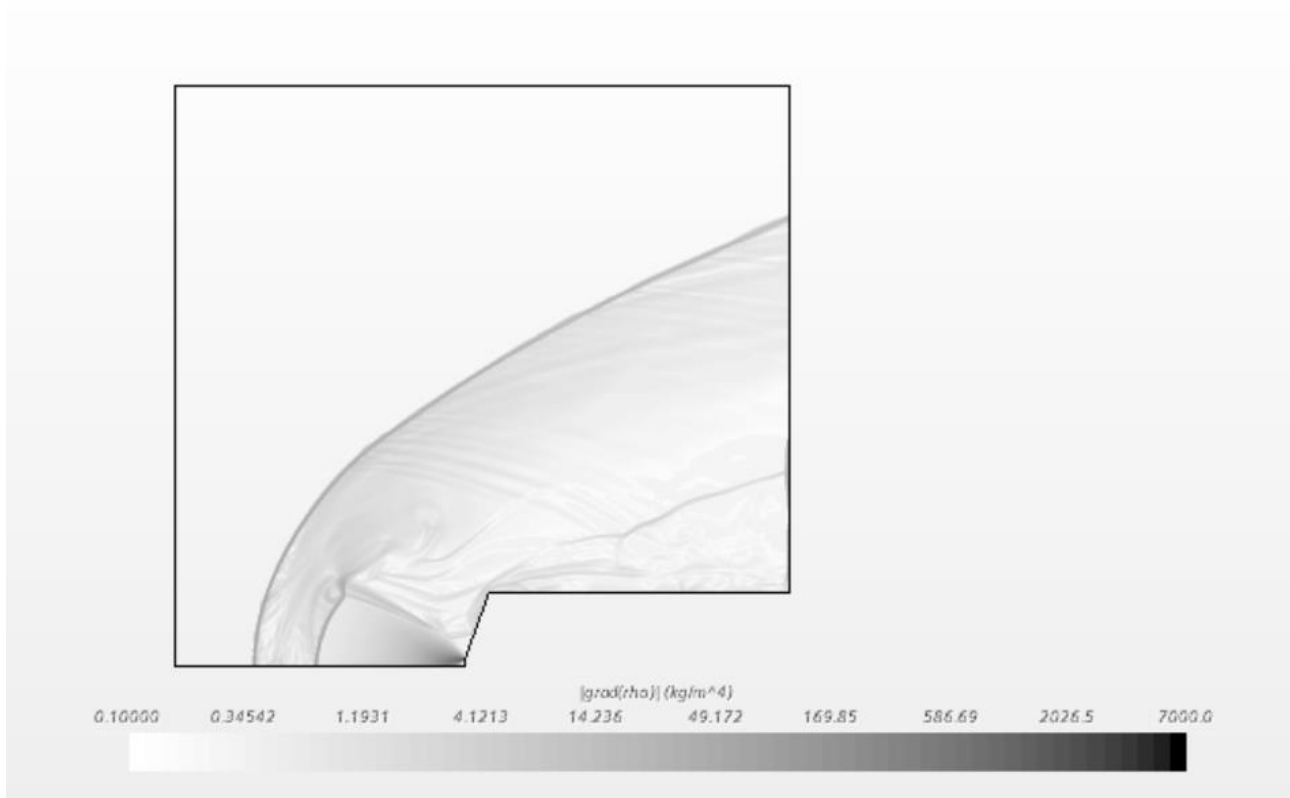


Figure 90-Pseudo Schlieren image, no-nozzle case

The only remarkable difference that emerged from the comparison of the pseudo-Schlieren image between the two simulations, relies on the triple point structure which is less marked in the no-nozzle case with respect to the nozzle case. This difference in the triple point pattern is related to the unsteady behavior of this contact region, whose structure strongly depends on the instant considered. Indeed as depicted before, the triple point oscillations and contractions are the source of the flowfield unsteadiness.

From the qualitative comparison between the Mach, temperature, pressure and pseudo Schlieren scenes between the two simulations is evident that the nozzle elimination doesn't affect the SRP flowfield structure. Through the scenes analysis is notable that the same quantities values are encountered in the same field regions, thus indicating no relevant variation induced by the substitution of the jet expansion inside the nozzle with the jet exit condition applied directly at the nozzle exit.

4.6.3. No nozzle case -flow features dimension

Even in the no nozzle simulation, the calculation of these quantities has been computed through the “measure distance” tool of STAR CCM+; the measurements are elaborated on the-pseudo Schlieren scene, which underlines all the desired flowfield features.

Table 28- comparison of flow features dimension

	Bow shock standoff distance	Bow shock radius	Jet plume length	Maximum jet plume radius
Flow features dimensions in cm for the no nozzle case	18.19	24.45	12.80	7.32
Flow feature dimensions in cm for the nozzle case	18.8	25.03	12.89	7.420
Percentage difference between the two cases	3.3%	2.3%	<1%	1.3%

The reduction of the bow shock standoff distance and jet plume length may have led to the displacement of point 3 from the subsonic region behind the Mach disk, to the subsonic region behind the bow shock, thus inducing the velocity difference underlined in the Mach average comparison.

However, the flow features dimensions are aligned with the calculation of the nozzle case, presenting the maximum percentage difference, related to the maximum jet plume radius, less than 4%. The no-nozzle simulation underestimates the quantities dimension by values that can be overlooked.

4.6.4 Pressure coefficient comparison

Besides the quantitative comparison executed in the three representative points, is important to compare the pressure coefficient with the nozzle situation and reference data, in order to understand if the nozzle elimination affects the computation of this value. Therefore, the pressure coefficient trends for either the forebody and aftbody are here reported. The calculation of this value has been computed with the same methodology adopted in the nozzle case.

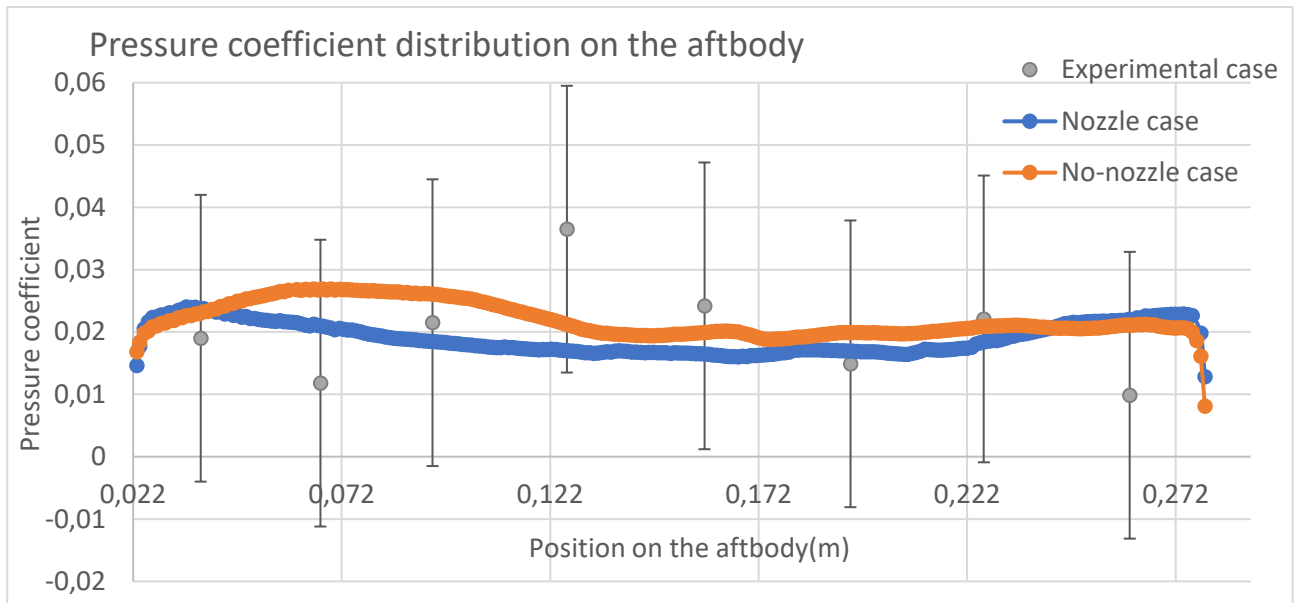


Figure 91-Aftbody averaged surface pressure coefficient distribution

Even in this simulation, the x-axis shows the position on the aftbody with respect to the X coordinate of the local systems, indeed the beginning of the aftbody is set to 0.022 m.

The curve starts with a local minimum, around 0.17, which is observable in the left part of the chart. This value is aligned either with the calculated value for the nozzle simulation and reference data. Subsequently the coefficient increases in the stretch corresponding to the positions between 0.04m and 0.08 m, where a local maximum of 0.027 is achieved. In this section the pressure coefficient for the no-nozzle case slightly overcomes the pressure coefficient computed with the nozzle simulation, indicating higher pressure values sampled at the beginning of the aftbody. However these values are still contained within an acceptable range with respect to the reference test data. Starting from 0.122 m, the coefficient remains constant throughout the body length with little fluctuations around the value of 0.02. This trend is in accordance with both the results of the nozzle simulation and the reference data. In correspondence to the end of the aftbody a strong pressure coefficient reduction is notable, aligned with the nozzle case to the value of -0.01.

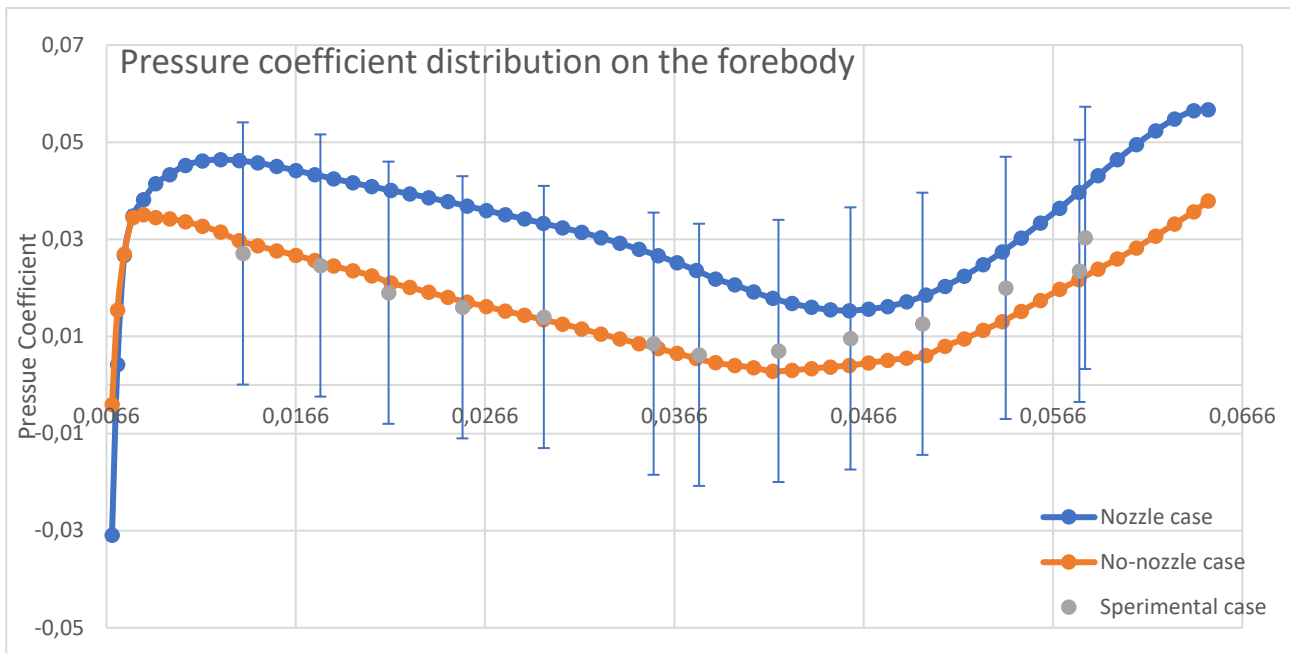


Figure 92-Forebody averaged surface pressure coefficient distribution

Even in the no-nozzle simulation, the pressure coefficient profile for the forebody does not show a constant trend.

The x-axis shows the position on the aftbody with respect to the Y coordinate of the local systems, indeed the begging of the forebody is set to 0.0066 m.

At the forebody beginning, the pressure is characterized by values around -0.01. The profile presents the values of the pressure coefficient predicted in the previous simulation and in the reference data: the coefficient increases, indeed the line is characterized by a positive slope until it reaches a local maximum of 0.038. Then the curve decreases progressively until a minimum value of 0.003, distinguished by an upwards concavity. This local minimum is aligned with reference data and previous simulation, which located the minimum value between the 60-70% of the forebody length, and computed its value varying between 0 and 0.18.

In addition the last part of the chart shows a progressive augmentation of the pressure coefficient, consistently with the reference data, until it reaches the second local maximum, 0.04, at the end of the forebody.

The quantitative analysis of the average pressure coefficient distribution on the forebody and aftbody confirmed that the nozzle elimination doesn't affect the global flowfield characteristics, demonstrating that the pressure coefficient variations occur within the same range at the same point, and thus obtaining results which are aligned either with the validated nozzle simulation and reference data.

The pressure coefficient values on the forebody and aftbody are contained within the range predicted by the test reference case, thus showing that the nozzle elimination does not affect the ability to correctly reproduce the experimental case.

This outcome, together with the quantitative and qualitative analysis previously carried out, shows how the elimination of the nozzle doesn't affect the ability to correctly simulate the flowfield, and therefore the computational savings related to this simplified situation can be obtained without modifying the quality of the solution

4.7 Frequency analysis

The frequency analysis is aimed to describe the unsteady phenomena related to the triple point oscillation: this oscillation creates pressure waves that propagate towards the bow shock and the body. These waves also reflect off the body and the barrel shock strengthening the oscillatory phenomena.

The analysis is computed for either the validated nozzle case simulation and for the no-nozzle case. Either the CFD validated codes , DPLR , FUN3D , OVERSET, and the tunnel test data , predicted peak frequency ranging from 1.7-2.2 kHz, with sharp patterns and multiple harmonics peaks at higher frequencies.

The analysis is realized upon 100000 iterations: despite the 40000 iterations used for the verification of the no-nozzle case, this number has been retained more significant to describe the oscillatory phenomenon, including a greater number of variations cycles.

For either the nozzle simulation and the no-nozzle case, point 4 has been considered for the analysis , as far as subject to the pressure variations induced by the pressure waves generated by the triple point and reflected off the body. Moreover , point 4 results were adopted for the comparison with the 165 test tunnel case, as far as the frequency analysis in the Langley test was computed either using pressure high-frequency transducers located on the body and studying the variation of pressure coefficient on the forebody.

The analysis was obtained through the Data set function STAR CCM+ tools, which allows the creation of a “ Point time Fourier Transforms”. This tool enables the Fourier transformation for one time point in the input signal: through the Fourier Transformation, the time signals are transformed to the frequency domain in order to identify the dominant modes in the signal. In the frequency domain peaks correspond to oscillatory component in time domain.

The amplitude function represented in the frequency domain is the Power Spectral Density. This function is a frequency domain description of the signal power, indeed is used to characterize broadband random signals because represents how power is distributed over frequencies. PSD shows the strength of the variations of the input signal as a function of frequency : in other words at which frequency the variations are strong or weak. Is always adopted to show the frequency and amplitude of oscillatory signals in a time series data.

In conclusion, the frequency peaks indicating high PSD levels, represent the fundamental modes identifying the unsteady phenomenon related to the triple point oscillation.

The following figure represents the Point 4 pressure signal over time transformed in the frequency domain with PSD level on the y-axis.

For the nozzle simulation the results are perfectly aligned with the reference data , underlying a dynamic peak frequency around 2 kHz, and slightly highlighting the presence of harmonics for 4 kHz.

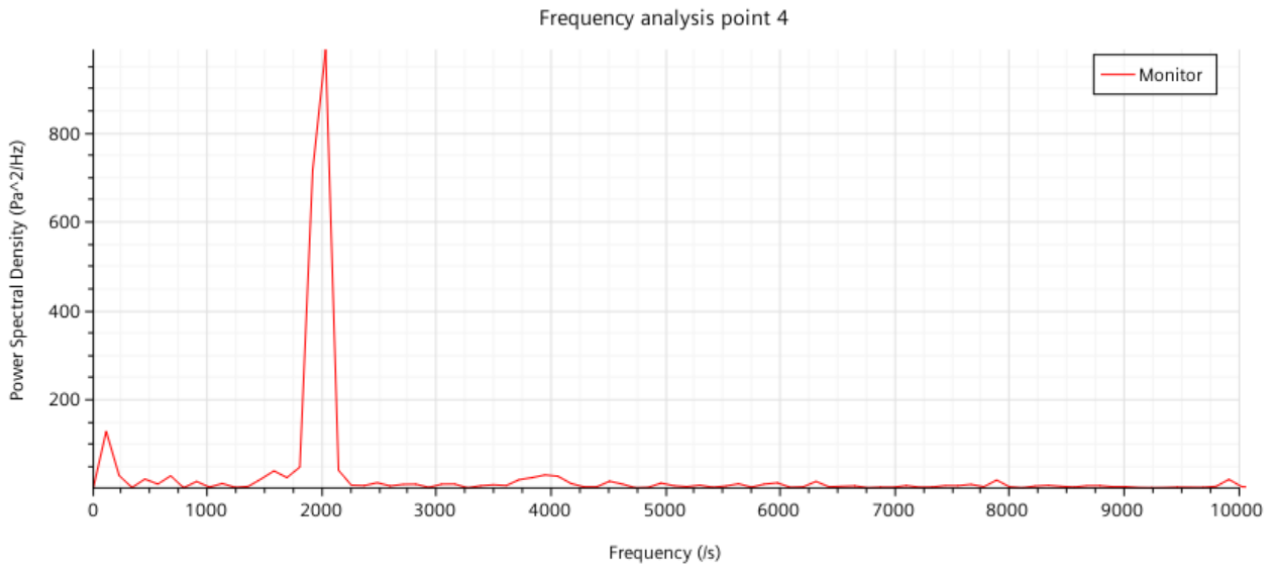


Figure 93-point 4 dynamic frequency analysis, nozzle simulation

The results for the no-nozzle case are aligned with the results of the nozzle simulation and with the test experimental case, showing a dynamic peak frequency to range from 2 to 2.2 kHz. Hence the nozzle elimination doesn't affect the ability to capture and simulate the unsteadiness characterizing the flowfield. It is also remarkable the presence of harmonics at 3.6-4 kHz and 5.2 kHz; these harmonics are shifted to lower frequencies compared to the reference case and appear more marked than the nozzle simulation.

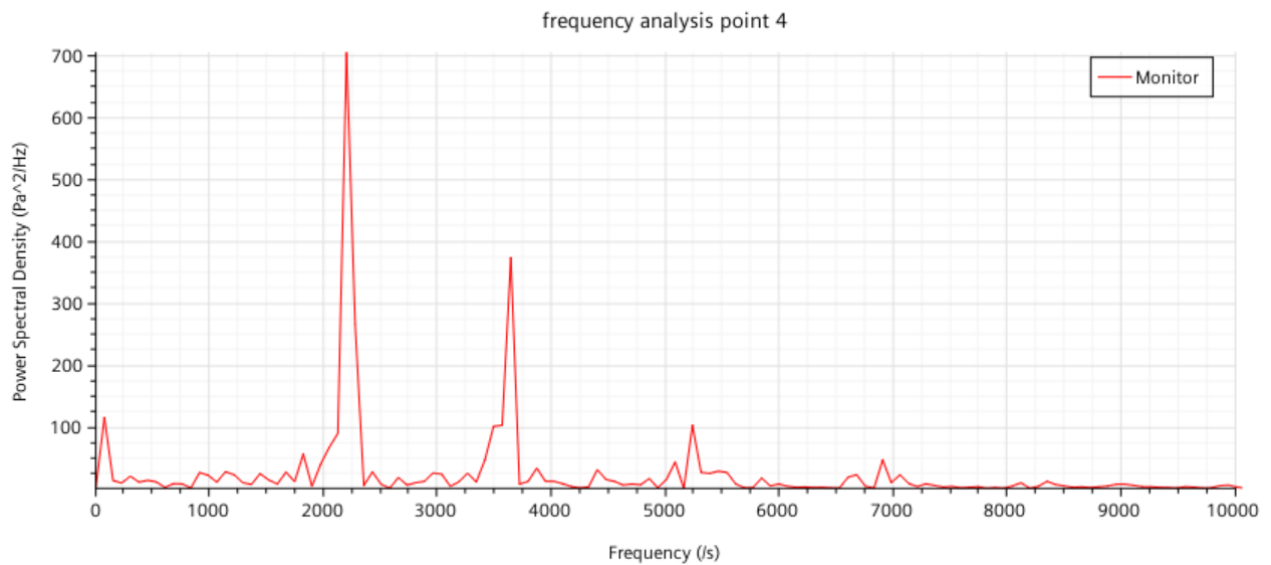


Figure 94-point 4 dynamic frequency analysis-no nozzle simulation

The set of these results demonstrates the ability of both the nozzle simulation and the no-nozzle case, to capture the unsteadiness of the flowfield; as far as this capability has been also related to the grid refinement and physics models adopted for the simulation set up, both these characteristics have been considered adequate and well-structured to describe the phenomenology analysed.

4.7.1. Frequency analysis with grid refinement

Considering that in CFD simulations the grid definition determines the simulation capabilities to best capture the unsteady events, a frequency analysis for the no-nozzle case has been computed implementing a grid thickening. Even in this simulation point 4 has been considered for the analysis. The mesh refinement implies a modification of the region inside the cone shape and leads to a large augmentation of the total number of cells, vertices and faces in the calculation domain. The total number of these features is reported in table 16. However, due to the very high number of computational cells, the computational cost has increased enormously compared to the previous case. For this reason, the frequency analysis was carried out on a number of iterations equal to 70000, which was defined as a good compromise between the need to capture the unstable phenomenon, including a greater number of variations cycles, and avoid too high computational times.

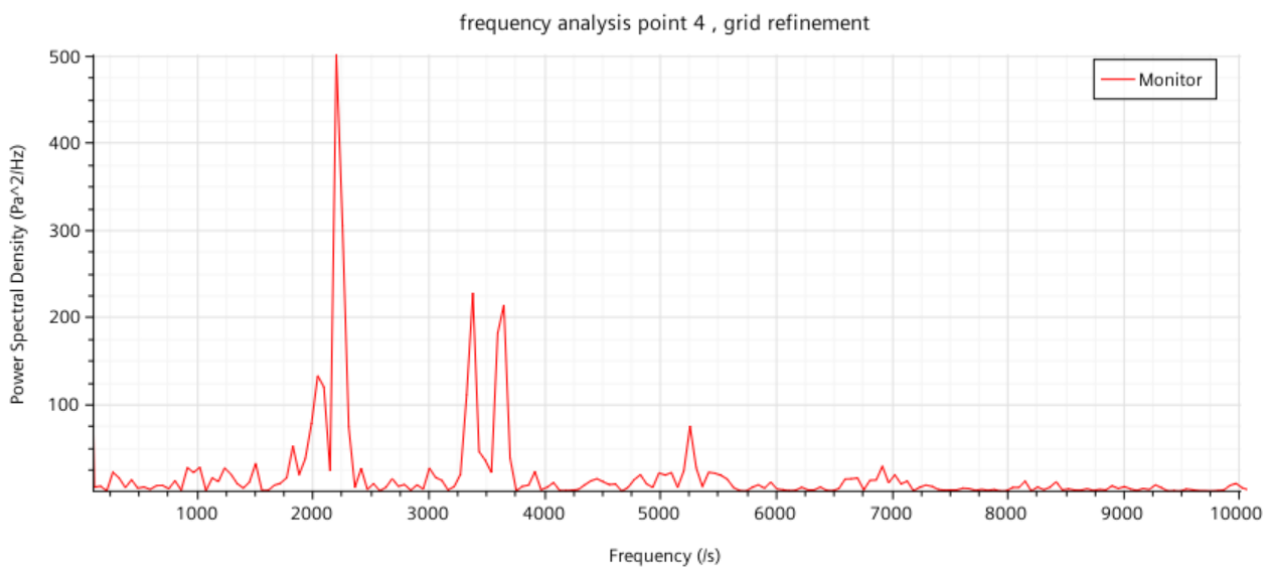


Figure 95-point 4 dynamic frequency analysis-no nozzle simulation, grid refinement

The results for the no-nozzle case with the grid refinement are aligned with the previous computations. A dynamic peak frequency ranging from 2 to 2.2 kHz was detected and considered as the predominant frequency, aligned with either the reference data and previous simulations; Moreover, harmonics characterized by double sharp peaks ranging to 3.4-3.7 kHz were found. These harmonics are shifted to lower frequencies compared to the previous case, but still have values traceable to experimental data, as those contained in reference [33].

In conclusion, considering the good quality of the results obtained with the initial grid with respect to the reference data, what emerges through the grid refinement is that the thickening does not lead to obvious improvements in the frequency analysis. For this reason, within the framework of the dynamic analysis, the mesh refinement is considered not necessary, as far as the computational cost induced by the larger number of cells does not balance the improvement of the results with respect to the initial grid.

Conclusion

At first, the supersonic retropropulsion has been introduced in the framework of the technologies used for the Mars Entry, Descent and Landing phase. The current technological limitations for the descent phase of the Mars EDL have been obtained through the analysis of the past landed unmanned missions. Indeed, the classical EDL approach, derived from Viking heritage, results not suitable to the characteristics required by Human Mars Class missions: the augmentation in the expected landed payload prevents the application of the EDL systems adopted for robotic and large-robotic missions.

The State of Art concerning the possible architectures which will enable a human mission on Mars, has been illustrated through the description of the results achieved by the NASA teams, EDL SA and MAWG. The work conducted by these teams establishes the current reference architecture for this type of mission. Moreover, in this context, the supersonic retropropulsion has been selected as the most likely means to slow down the spacecraft during the descent phase; the preliminary outcome of NASA studies concerning the parametrization and conceptual design of a propulsion system able to implement SRP in relevant Mars conditions is also presented.

Subsequently, the TRL level of the technology is discussed, examining the technical challenges to face in order to raise the technological readiness level. In this context, the aerodynamic field represents an important area of research and one of the major challenges of this area is the development and validation of CFD models, needed to build aerodynamic databases.

For this reason, the bulk of the dissertation is focused on performing a CFD simulation able to reproduce the aerodynamic main features of the SRP. To better understand the complexity of the flowfield and the expected results, all the factors that contribute to the definition of the flowfield have been briefly described.

The reference data required to validate the simulation have been taken from one run elaborated during one of the wind tunnel tests aimed to validate CFD codes for SRP, i.e. LARC 4x4 UPWT, conducted by NASA ETD TDP; the test reference case is the run 165. Due to the complexity of the interaction between an exhausting jet and an opposing freestream, the configuration tested represents the simplest jet case available, with periodic and axisymmetric flowfield structure.

The model chosen for the simulation is a slender 70° sphere cone body with a 5 inch diameter, presenting a central nozzle and a cylindrical forebody 10 inches long. Following the set-up of the CFD simulation through STAR CCM+, the analysis of the results is detailed. In order to validate the simulation, quantitative and qualitative comparisons with reference data, either of the wind tunnel test and already validated NASA codes, have been carried out.

The qualitative comparison is based on images representing the pressure, temperature, and Mach isocontours field for an arbitrary solution time, while the quantitative comparison is based on the determination of main flow features dimension and on the estimation of the averaged surface pressure coefficient distribution on the forebody and aftbody.

The qualitative analysis shows that the code is indeed able to represent all the main features distinguishing SRP flowfield, maintaining the quantities variations range within those predicted by the experimental reference test case and the other CFD validated codes; the quantitative analysis of the average pressure coefficient distribution on the forebody and aftbody, has confirmed the simulation capability to properly reproduce the reference test case conditions and results, defining a similar pressure coefficient

distribution over the aftbody and forebody with the maximum discrepancy found at the end of the aftbody, but this difference is nevertheless kept within acceptable values. Moreover, the flow features main dimensions measured for the simulation case are aligned with the experimental measurements: the percentage difference between the two cases is less than 5% for all values.

Given the excellent results obtained both from a qualitative and quantitative point of view, it can be considered that the simulation implemented has met the necessary requirements for validation and can therefore constitute a solid baseline for further analysis and simulation.

Thus, exploiting the initial conditions set by the CFD validated code, a second simulation investigating the effect of the nozzle elimination and substitution by the jet exit condition at the nozzle exit has been carried out. Following the computation of the stagnation inlet condition and the realization of the simplified model, three different points have been collocated as probes inside three relevant regions of the flowfield.

As for the validation of the first simulation, a qualitative analysis is implemented, aimed to compare the pressure, temperature, and Mach number trends within the flowfield between the two simulations. Moreover, a quantitative analysis is developed through the comparison of the average pressure coefficient distribution on the forebody and aftbody, the flowfield main features dimension, and the trends of the quantities over time and their time averages for each probe point.

Through the scenes analysis is notable that the same quantities values are encountered in the same field regions, thus indicating no relevant variations induced by the substitution of the jet expansion inside the nozzle with the jet exit condition applied directly at the nozzle exit. The quantitative analysis of the average pressure coefficient distribution on the forebody and aftbody confirmed that the nozzle elimination doesn't affect the global flowfield characteristics, demonstrating that pressure coefficient variations occur within the same range at the same point, and thus obtaining results which are aligned either with the validated nozzle simulation and reference data. In addition, following the comparison of numerical and graphical trends of the field parameters in the selected three probe points, the elimination of the jet expansion inside the nozzle doesn't affect the flowfield quantities, either in the supersonic and subsonic region, except for a Mach value in the probe point 3, located in the stagnation region between the bow shock and Mach disk. However this discrepancy may be related to the reduction of bow shock standoff distance and jet plume length, which may have led to the displacement of this point from the subsonic region behind the Mach disk, where was located within the nozzle simulation, to the subsonic region behind the bow shock, inducing the velocity difference underlined in the Mach average comparison. In conclusion, the computational savings related to the no-nozzle situation could be implemented without modifying the quality of the solution, paving the road for the application of this principle in more complex simulations.

Finally a frequency analysis has been computed either for the nozzle and no-nozzle simulations, aimed to describe the unsteady phenomena related to the triple point oscillation; the analysis is realized upon 100000 iterations as far as this number has been retained large enough to describe the oscillatory phenomenon, including a greater number of variations cycles. The set of these results demonstrates the ability of both the nozzle simulation and the no-nozzle case to capture the unsteadiness of the flowfield, underlying a dynamic peak frequency around 2 kHz, and highlighting the presence of harmonics between 3.7-4 kHz. In conclusion a grid refinement was computed on the no-nozzle simulations to study how the mesh definition affects the capability to capture the unsteady phenomena. The results of the frequency analysis for this case are aligned with the previous simulations, not showing significant improvements with respect to the previous case. Thus, in the framework of the frequency analysis for these simulations, the mesh refinement has been considered not necessary, as far as the computational cost induced by the larger number of cells does not balance the low improvement of the results compared to the previous calculations.

The CFD simulations results obtained within the dissertation could constitute a viable basis on which to carry out further analysis aimed at studying the fluid dynamics and aero-thermodynamics that characterize the supersonic retropropulsion flowfield. Either way, further work is required to simulate the interaction between the oncoming freestream and the exhausting jet under relevant conditions, i.e. with non-scaled models, through the use of hot gases in the nozzle, through the adaptation of gases that constitute the Martian atmosphere for the oncoming freestream, varying the AoA of the oncoming freestream etc . Is also important to understand how the physicals models and solvers adopted affect the quality of the results, for example to see under equal conditions how a turbulent approach affects the capability to capture the unsteadiness.

Bibliography

- [1] W. C. C. R. , E. Adler, "Draft Entry , Descent, and Landing Roadmap Technology area 09," NASA, 2010.
- [2] N. Science, "Mars Exploration Program," [Online].
- [3] R. M. Robert D. Braun, "Mars Exploration Entry, Descent and Landing Challenges," in *2006 IEEE Aerospace Conference.*, 2006.
- [4] NASA, "VIKING," 1975.
- [5] D. J. M. B. D. G. K. S. M. J. S. Gerarld A. Soffen, "NASA Space Science Data Coordinated Archive," [Online]. Available: <https://nssdc.gsfc.nasa.gov/nmc/spacecraft/display.action?id=1975-075C>.
- [6] N. F. Jet Propulsion Laboratory, "Viking Mission to Mars," 1988. [Online]. Available: https://mars.nasa.gov/internal_resources/828/.
- [7] R. e. a. Prakash, "Mars Science Laboratory entry, descent, and landing system overview," in *IEEE Aerospace Conference*, 2008.
- [8] R. M. a. M. A. Manning, *Landing on Mars*, 2005.
- [9] G. K. Ball, *Planetary landers and entry probes*, 2007.
- [10] J. L. D. D. R. K. M. M. M. J. A. S. J. A. W.-B. a. T. A. Z. e. a. Alicia M. Dwyver Cianciolo, "Entry, Descent and Landing Systems Analysis Study : phase 1 Report," NASA, 2010.
- [11] G. W. a. Wells, *Entry descent and landing challenges of human Mars exploration*, 2006.
- [12] B. G. , S. J. H. D. W. B. Drake, "Human exploration of Mars, design reference architecture 5.0," in *IEEE Aerospace Conference* , 2010.
- [13] T. e. a. Zang, "Overview of the NASA entry descent and landing systems analysis study," in *AIAA SPACE 2010 Conference & Exposition* , 2010.
- [14] B. G. a. D. W. K. Drake, "Human exploration of Mars design reference architecture 5.0 addendum #2," 2014.
- [15] P. A. Gnoffo, "Planetary-entry gas dynamics.," *Annual Review of Fluid Mechanics* , vol. 31, no. 1, pp. 459-494, 1999.
- [16] G. a. M. A. ". t.-d. c. m. f. b. b. f. A. J. 4. (. 2.-2. MORETTI, "A time-dependent computational method for blunt body flows," *AIAA Journal*, vol. 4, no. 12, pp. 2136-2141, 1966.
- [17] A. , W. Anderson, "On hypersonic blunt body flowfield obtained with a time dependent technique," *United States Naval Ordnance Laboratory*, vol. 68, 1968.
- [18] A. Korzun, "Aeodynamic and performance characterization of supersonic retropropulsion for application to planetary entry and descent," Georgia Institute of Technology, 2012.

- [19] F. A. Albini, "Approximate computation of underexpanded jet structure," *AIAA Journal*, vol. 3, no. 8, pp. 1535-1537, 1965.
- [20] M. e. a. Metha, "Thruster plume surface interactions : applications for spacecraft landing on planetary bodies," *AIAA journal*, vol. 51, no. 12, pp. 2800-2818, 2013.
- [21] J. e. a. Wilkes, "Fluorescence imaging of underexpanded jets and comparison with CFD," in *44th AIAA Aerospace Sciences Meeting and Exhibit*, 2006.
- [22] A. C. C. ,. a. R. B. Korzun, "Comparison of inviscid and viscous aerodynamic predictions of supersonic retropropulsion flowfields," in *10th AIAA/ASME Joint Thermophysics and Heat Transfer Conference*, 2010.
- [23] C. a. W. P. Peters, "An approximate analysis of the shock structure in underexpanded plumes," *ARNOLD ENGINEERING DEVELOPMENT CENTER ARNOLD AFB TN*, Vols. AEDC-TR, 1976.
- [24] F. P.J, "The flow of a jet from a body opposing a supersonic free stream," *Journal of Fluid Mechanics*, vol. 26, no. 2, pp. 337-368, 1966.
- [25] D. K. I. M. B. A. H. A. Ota, "The Dynamics of Shock Dispersion and Interactions in Supersonic Freestreams with Counterflowing Jets," NASA Marshall Space Flight Center.
- [26] A. M. J. R. a. R. B. Korzun, "A survey of supersonic retropropulsion technology for mars entry, descent, and landing.," in *2008 IEEE Aerospace Conference*, 2008.
- [27] K. T. e. a. Edquisit, "" Development of supersonic retropropulsion for future mars, entry , descent and landing systems."," *Journal of Spacecraft and Rockets*, vol. 51, no. 3, pp. 650-663, 2014.
- [28] P. a. R. A. Jarvinen, *The Aerodynamic Characteristics of Large Angled Cones with Retrorockets*, 1970.
- [29] D. e. a. Schauerhamer, "" Supersonic Retropropulsion Computational Fluid Dynamics Validation with Langley 4x4 Foot Test Data," *Journal of Spacecraft and Rockets*, vol. 51, no. 3, pp. 693-714, 2014.
- [30] S. A. a. M. N. R. Berry, "Supersonic Retropropulsion Test 1853 in NASA LaRC Unitary Plan Wind Tunnel Test Section 2," 2014.
- [31] W. e. a. Kleb, "Toward Supersonic Retropropulsion CFD validation," in *42nd AIAA Thermophysics Conference*, 2011.
- [32] e. a. Schauerhamer, "" Continuing Validation of Computational Fluid Dynamics for Supersonic Retropropulsion," in *50th AIAA Aerospace Sciences Meeting including the New Horizons forum and Aerospace Exposition*, 2012.
- [33] J. S. B. Codoni, "Analysis of Dynamic Data from Supersonic Retropropulsion Experiments in NASA Langley's Unitary Plan Wind Tunnel," in *42nd AIAA Fluid Dynamics Conference and Exhibit*, 2012.
- [34] Siemcenter, STAR CCM+ Manual.